

การตกตะสมและลักษณะเฉพาะของฟิล์มคาร์บอนคล้ายเพชร โดปด้วยกำมะถัน
โดยวิธีการตกตะสมด้วยเลเซอร์ชนิดพัลส์

นางสาวกัญจน์ชญา หงส์เลิศงสกุล

วิทยานิพนธ์นี้เป็นส่วนหนึ่งของการศึกษาตามหลักสูตรปริญญาวิทยาศาสตรดุษฎีบัณฑิต
สาขาวิชาฟิสิกส์ ภาควิชาฟิสิกส์
คณะวิทยาศาสตร์ จุฬาลงกรณ์มหาวิทยาลัย
ปีการศึกษา 2552
ลิขสิทธิ์ของจุฬาลงกรณ์มหาวิทยาลัย

DEPOSITION AND CHARACTERISATION OF SULPHUR DOPED
DIAMOND-LIKE CARBON FILMS USING PULSED LASER
DEPOSITION METHOD

Miss Kanchaya Honglertkongsakul

A Dissertation Submitted in Partial Fulfillment of the Requirements
for the Degree of Doctor of Philosophy Program in Physics

Department of Physics

Faculty of Science

Chulalongkorn University

Academic Year 2009

Copyright of Chulalongkorn University

กัญจน์ชญา หงส์เลิศคงสกุล : การตกสะสมและลักษณะเฉพาะของฟิล์มคาร์บอนคล้ายเพชรโคปด้วยกำมะถัน โดยวิธีการตกสะสมด้วยเลเซอร์ชนิดพัลส์ (DEPOSITION AND CHARACTERISATION OF SULPHUR DOPED DIAMOND-LIKE CARBON FILMS USING PULSED LASER DEPOSITION METHOD) อ. ที่ปริกษาวิทยานิพนธ์หลัก : ผศ. ดร. บุญโชติ เผ่าสวัสดิ์ยรรยง, อ. ที่ปริกษาวิทยานิพนธ์ร่วม : Paul W. May, Ph.D., 131 หน้า.

การเสียดละลายของเป่าผสมกำมะถันกับแกรไฟต์ ทำโดยการตกสะสมของเลเซอร์ที่ถูกกระตุ้นด้วยแก๊สอาร์กอนฟลูออไรด์ ที่มีความยาวคลื่น 193 นาโนเมตรและมีกำลัง 10 และ 20 จูลต่อตารางเซนติเมตรในสุญญากาศ ทำให้เกิดฟิล์มคาร์บอนคล้ายเพชรโคปด้วยกำมะถัน เป่าผสมกำมะถันกับแกรไฟต์ทำจากการผสมผงกำมะถันกับแกรไฟต์ ที่จำนวนร้อยละของโมลาร์ของกำมะถันแตกต่างกัน เช่น 0%, 1%, 5%, 10% และ 25% ฟิล์มคาร์บอนคล้ายเพชรโคปด้วยกำมะถันถูกปลูกลงบนแผ่นรองรับซิลิกอนและควอตซ์ ที่อุณหภูมิของแผ่นรองรับแตกต่างกัน เช่น อุณหภูมิห้อง 150 องศาเซลเซียส และ 250 องศาเซลเซียส ผลของอุณหภูมิของแผ่นรองรับกำลังของเลเซอร์ และจำนวนร้อยละของโมลาร์ของกำมะถัน ที่มีต่อสมบัติทางไฟฟ้า ทางแสง ทางกล และทางโครงสร้างของฟิล์มได้ถูกศึกษา ฟิล์มคาร์บอนคล้ายเพชรโคปด้วยกำมะถันในงานนี้มีค่าสภาพต้านทานอยู่ในช่วง 10^3 ถึง 10^6 โอห์มเซนติเมตร สอดคล้องกับค่าแถบพลังงานในช่วง 0.25 ถึง 2.00 อิเล็กตรอนโวลต์ ค่าความเข้มข้นของพาหะอยู่ในช่วง 10^{14} - 10^{18} ต่อลูกบาศก์เซนติเมตร ผลของการโคปฟิล์มคาร์บอนคล้ายเพชรด้วยกำมะถัน ทำให้ฟิล์มเป็นสารกึ่งตัวนำชนิดเอ็น ค่าสอลล์โมบิลิตี้อยู่ในช่วง 10^{-5} -1 ตารางเซนติเมตรต่อโวลต์วินาที ความหนาของฟิล์มอยู่ในระดับร้อยนาโนเมตร ค่าความแข็งของฟิล์มอยู่ในช่วง 10-30 จิกะพาสคัล ลักษณะพื้นผิวหน้าของฟิล์มพบอนุภาคระดับไมครอนกระจายบนพื้นผิว ผลการวิเคราะห์ส่วนประกอบของธาตุยืนยัน การมีอยู่ของกำมะถันในฟิล์ม

ภาควิชา .. ฟิสิกส์ ลายมือชื่อนิสิต

สาขาวิชา .. ฟิสิกส์ ลายมือชื่อ อ. ที่ปริกษาวิทยานิพนธ์หลัก

ปีการศึกษา .. 2552 ลายมือชื่อ อ. ที่ปริกษาวิทยานิพนธ์ร่วม

4873810923 : MAJOR PHYSICS

KEYWORDS: DIAMOND-LIKE CARBON FILMS / SULPHUR DOPED
DIAMOND-LIKE CARBON FILMS / PULSED LASER DEPOSITION
METHODS

KANCHAYA HONGLERTKONGSAKUL: DEPOSITION AND
CHARACTERISATION OF SULPHUR DOPED DIAMOND-LIKE
CARBON FILMS USING PULSED LASER DEPOSITION METHOD.
THESIS ADVISOR: ASSISTANT PROFESSOR BOONCHOAT
PAOSAWATYANYONG, Ph.D., THESIS CO-ADVISOR: PAUL W.
MAY, Ph.D., 131 pp.

Ablation of a sulphur-graphite target was carried out by ArF excimer laser deposition at a laser wavelength of 193 nm and fluence of 10 and 20 J/cm² in vacuum to produce sulphur-doped diamond-like carbon (S-DLC) films. The sulphur-graphite target was made from sulphur and graphite powder mixed at different sulfur molar percentages, e.g. 0%, 1%, 5%, 10% and 25%. S-DLC films were deposited on silicon and quartz substrates at different substrate temperatures, e.g. room temperature, 150°C and 250°C. The effects of substrate temperature, laser fluence and sulphur molar percentage on the electrical, optical, mechanical and structural properties of the resulting films were studied. The S-DLC films in this work showed resistivity values in the range of 10³-10⁶ Ω·cm, corresponding to a band gap in the range of 0.25-2.00 eV. The carrier concentration was found to be in the range of 10¹⁴-10¹⁸ cm⁻³. The effect of doping the DLC films with sulphur was found to convert the films into an n-type semiconductor. The Hall mobility was in the range of 10⁻⁵-1 cm²·V⁻¹·s⁻¹. The thickness of the films was in the hundred nanometers range, while the hardness of the films was in the range of 10-30 GPa. The surface morphology showed the presence of micron-sized particulates on the surface. Elemental composition analysis confirmed the presence of sulphur in the films.

Department : Physics..... Student's Signature

Field of Study : Physics..... Advisor's Signature

Academic Year : 2009..... Co-Advisor's Signature

ACKNOWLEDGEMENTS

There are a large number of people to whom I need to grateful, both academically and socially, during my Ph.D. First of all, I would like to express my deepest gratitude to my supervisor Assistant Professor Boonchoat Paosawatyanong, and my co-supervisor Dr. Paul W. May. They helped and supported me through my dissertation. Without any of them it would be impossible for this dissertation to be accomplished.

Dissertation committee, Assistant Professor Dr. Sojiphong Chatraphorn, Assistant Professor Dr. Rattachat Mongkolnavin, Dr. Varagorn Hengpunya and Assistant Professor Dr. Tanakorn Osothchan, who spent their time inspecting this dissertation and gave very kind comments to help with the dissertation production.

Department of Physics, Faculty of Science, Chulalongkorn University for giving me the opportunity to study for a Ph. D. Assistant Professor Dr. Somchai Kiatgamolchai for helping with the Hall effect measurements. NanoShield Co., Ltd for letting me use their Nanoindentation measurement apparatus.

School of Chemistry, University of Bristol for giving me to opportunity to use many instruments. Dr. Sean Pearce at the Interface Analysis Centre, Bristol for providing SIMS measurements, and Dr. James Smith, Dr. Gareth Fuge and Dr. Jie Ma from the Bristol University diamond group (Budgies) for all their helpful suggestions during my work. And all of my friends at Hodgkin House, Bristol for supporting me during the time I stayed there.

For financial support I would like to thank the Office of the Higher Education Commission and the 90th Anniversary of Chulalongkorn University Fund (Ratchadaphiseksomphot Endowment Fund).

Finally, I would like to express my deepest gratitude to my family, and all of my friends for their entire care, love, patience and encouragement.

CONTENTS

	Page
THAI ABSTRACT	iv
ENGLISH ABSTRACT	v
ACKNOWLEDGEMENTS	vi
CONTENTS	vii
LIST OF TABLES	xii
LIST OF FIGURES	xiii
CHAPTER I INTRODUCTION	1
1.1. Motivation of This Dissertation	1
1.2. Aim of This Dissertation	3
1.3. Dissertation Outline	3
CHAPTER II DIAMOND-LIKE CARBON	5
2.1. Allotropes of Carbon	5
2.1.1. Graphite	6
2.1.2. Diamond	7
2.1.3. Properties of Diamond and Graphite	9
2.2. Amorphous Carbon and Diamond-Like Carbon	11
2.2.1. The Synthesis of DLC	14
2.2.2. DLC Deposition Mechanism	14
2.2.3. Properties of DLC	16
2.2.3.1. Electrical Properties	17
2.2.3.2. Optical Properties	18
2.2.3.3. Mechanical Properties	19
2.2.4. Applications of DLC Films	20
2.3. Doping of Diamond and Diamond-Like Carbon	20
2.3.1. P-Type Doping	22
2.3.2. N-Type Doping	22
2.3.3. a-C Alloys	23
2.3.3.1. CN _x Films	23
2.3.3.2. CP _x Films	24

	Page
2.3.3.3. CS _x Films.....	25
2.4. Summary.....	25
CHAPTER III PULSED LASER DEPOSITION	26
3.1. Choice of Laser.....	27
3.1.1. Excimer Laser Basics.....	28
3.2. Pulsed Laser Ablation and Deposition	32
3.2.1. Characteristics of the PLD process	32
3.2.1.1. Stoichiometric Transfer.....	32
3.2.1.2. The Energetics of the Ablation Plasma.....	33
3.2.1.3. Multi-Layered Films	33
3.2.1.4. Uniform Thickness Over a Controlled Area.....	33
3.2.2. The Stages of PLA	34
3.2.2.1. Surface Heating.....	35
3.2.2.2. Surface Melting and Thermionic Emission	36
3.2.2.3. Enhancing the Production of a Plasma.....	37
3.2.2.4. Absorption of the Laser Radiation by the Plasma.....	37
3.2.3. Effect of Process Parameters.....	37
3.2.3.1. Laser Wavelength	38
3.2.3.2. Laser Fluence	39
3.2.3.3. Background Gas	40
3.2.3.4. Target-to-Substrate Distance.....	40
3.2.3.5. Substrate Temperature	40
3.2.4. Particulates	41
3.2.4.1. Elimination of Particulates.....	42
3.2.4.1.1. Laser Effects.....	42
3.2.4.1.2. Plume Effects	42
3.2.4.1.3. Geometry.....	43
3.3. Diamond-Like Carbon Films Produced by PLD	44
CHAPTER IV EXPERIMENTAL SETUP	46
4.1. Pulsed Laser Deposition	46
4.2. Excimer Laser	48

	Page
4.3. Vacuum Ablation Chamber	50
4.4. Target Material	50
4.5. Substrate and Substrate Heating	52
4.6. Carbon Dioxide Laser (CO ₂ Laser)	52
CHAPTER V CHARACTERISATION TECHNIQUES	53
5.1. Laser Raman Spectroscopy (LRS).....	53
5.1.1. Introduction	53
5.1.2. Theory	53
5.1.3. Spectrum Fitting.....	57
5.1.4. Graphitization and the I_D/I_G Ratio.....	57
5.1.5. Factors Affecting the Spectrum	58
5.1.6. Characterisation of DLC Films by LRS.....	59
5.1.7. LRS Setup	60
5.2. Spectroscopic Ellipsometry (SE).....	61
5.2.1. Introduction	61
5.2.2. Theory	61
5.2.3. Fitting Model.....	62
5.2.4. SE Setup	64
5.3. Ultraviolet-Visible Spectroscopy (UV-VIS)	64
5.3.1. Introduction	64
5.3.2. Theory	64
5.3.3. Estimation the Optical Band Gap.....	66
5.3.4. UV-VIS Setup	67
5.4. Linear Four-Point Probe Measurement	68
5.4.1. Introduction	68
5.4.2. Theory	68
5.4.3. Linear Four-Point Probe Setup.....	69
5.5. Hall Effect Measurement	70
5.5.1. Introduction	70
5.5.2. Theory	70
5.5.3. Hall Effect Setup	72

	Page
5.6. Scanning Electron Microscopy (SEM) and Energy	
Dispersive X-ray Spectroscopy (EDX).....	72
5.6.1. Introduction.....	72
5.6.2. Theory.....	72
5.6.3. SEM Setup.....	74
5.7. Secondary Ion Mass Spectroscopy (SIMS).....	75
5.7.1. Introduction.....	75
5.7.2. Theory.....	75
5.7.3. SIMS Setup.....	76
5.8. Nanoindentation.....	78
5.8.1. Introduction.....	78
5.8.2. Theory.....	78
5.8.3. Nanoindentation Setup.....	79
CHAPTER VI RESULTS AND DISCUSSIONS.....	80
6.1. Electrical Properties.....	80
6.1.1. Film Resistivity.....	80
6.1.2. Carrier Concentration and Hall Mobility.....	84
6.2. Optical Properties.....	88
6.2.1. Refractive Index and Extinction Coefficient.....	88
6.2.2. Optical Band Gap.....	89
6.3. Physical Properties.....	92
6.3.1. Surface Morphology.....	92
6.3.2. Film Thickness.....	95
6.3.3. Film Hardness.....	97
6.4. Structural Properties.....	99
6.4.1. G Peak Position and I_D/I_G Ratio.....	99
6.4.2. Elemental Composition by EDX.....	108
6.4.3. Elemental Composition by SIMS.....	109
CHAPTER VII CONCLUSIONS AND SUGGESTIONS.....	111
7.1. Conclusions.....	111
7.2. Suggestions.....	113

	Page
REFERENCES.....	114
APPENDICES	126
APPENDIX A.....	127
APPENDIX B.....	130
BIOGRAPHY	131

List of Tables

	Page
Table 2.1 Some applications of diamond.....	9
Table 2.2 Some properties of graphite and diamond. RT = room temperature	10
Table 2.3 Properties of some phases of carbon.....	17
Table 2.4 Some applications of DLC films with the required properties	20
Table 3.1 Wavelengths of common excimer laser systems	29
Table 3.2 Mean kinetic energy of ionised carbon species produced by different wavelengths during PLA of graphite	38
Table 3.3 Summary of the reported results for DLC films deposited by PLD. E_g is the energy band gap, and the percentage values correspond to the amount of sp^3 carbon in the film.....	45
Table 4.1 Experimental parameters. RT = room temperature.....	46
Table 5.1 LRS setup conditions for measurement of the DLC films.....	60
Table 6.1 Hardness of S-DLC film deposited at 10 J/cm^2 of laser fluence at various sulphur molar percentage and at room temperature and 150°C	97
Table 6.2 Hardness of DLC film deposited at room temperature at 0% sulphur molar percentage at 10 J/cm^2 and 20 J/cm^2 laser fluence	97

List of Figures

	Page
Figure 2.1 Crystalline structure of graphite with three graphene planes.	6
Figure 2.2 Configuration of sp^2 hybrid orbitals in graphite.....	7
Figure 2.3 Crystalline structure of diamond	8
Figure 2.4 Configuration of sp^3 hybrid orbitals in diamond	8
Figure 2.5 Structure of a hydrogen-containing diamond-like carbon film. The black spheres represent C atoms with 3 bonds (sp^2), the gray spheres represent C atoms with 4 bonds (sp^3), and the small white spheres represent hydrogen	12
Figure 2.6 Ternary phase diagram of amorphous carbon films	13
Figure 2.7 Impact of an ion on a substrate, showing (a) direct penetration, and (b) penetration by displacement.....	15
Figure 2.8 Density-of-electron-states for a DLC film.....	17
Figure 3.1 Potential energy diagram of an ArF excimer laser system.....	29
Figure 3.2 Schematic diagram of an ArF excimer laser cavity.....	31
Figure 3.3 Film thickness and deposited area depend on the distance away from target	34
Figure 3.4 Four main stages of PLA	35
Figure 3.5 Number of particulates corrected for the film thickness as a function of laser fluence	39
Figure 3.6 Schematic diagram of a velocity filter for elimination of slow-moving particulates from a fast plume.....	43
Figure 3.7 Off-axis PLD geometry to produce reduced-particulate films	44
Figure 4.1 Schematic of PLD system.....	47
Figure 4.2 Photograph of PLD system.....	47
Figure 4.3 Schematic diagram of the laser set-up.....	49
Figure 4.4 SEM image of the laser drilled hole on the target surface.....	49
Figure 4.5 Photograph of the 10-ton press and the compressed target material in the form of a 5 cm diameter, 1 cm thick disc	51
Figure 4.6 Schematic diagrams of (a) substrate and (b) heated substrate.....	52
Figure 5.1 Schematic diagram of the LRS microscope.....	55

	Page
Figure 5.2 Photograph of the Renishaw 2000 LRS microscope.....	55
Figure 5.3 Carbon motion in the (a) G mode and (b) D mode.....	56
Figure 5.4 Deconvolution of the Raman spectrum with two Gaussians in DLC film.....	57
Figure 5.5 Variation of I_D/I_G ratio with L_a	58
Figure 5.6 Schematic diagram showing the position and heights of D and G peak of DLC films in a Raman spectrum	59
Figure 5.7 Geometry of SE measurements	62
Figure 5.8 Photograph of J.A. Woollam M-2000U SE.....	62
Figure 5.9 Model fitting of (a) silicon dioxide layer (b) film layer, using results of (a) for the SiO ₂ layer.	63
Figure 5.10 Schematic diagram of the UV-VIS spectroscopic set-up	65
Figure 5.11 Photograph of the UV-VIS spectroscopic holder	66
Figure 5.12 Example of transmittance spectrum as a function of wavelength	66
Figure 5.13 Example of a Tauc plot from a DLC film deposited at room temperature and 10 J/cm ²	67
Figure 5.14 Schematic diagram of a Linear Four-Point Probe	69
Figure 5.15 Photograph of a Linear Four-Point Probe.....	69
Figure 5.16 Schematic diagram of the Hall Effect.....	70
Figure 5.17 Photograph of Hall Effect apparatus.....	71
Figure 5.18 Schematic diagram of a simple SEM	74
Figure 5.19 Photograph of an SEM	75
Figure 5.20 Basic principle of SIMS	77
Figure 5.21 Photograph of SIMS apparatus.....	77
Figure 5.22 Schematic diagram of a load-displacement curve in Nanoindentation. ...	79
Figure 5.23 Photograph of Nanoindentation apparatus.....	79
Figure 6.1 Example of a current-voltage characteristic from S-DLC film deposited at 0% sulphur molar percentage at 150° C with 10 J/cm ² of laser fluence	81

Figure 6.2 Resistivity values of DLC and S-DLC films versus % atomic ratio of S/C at different substrate temperatures and at 10 J/cm ² and 20 J/cm ² of laser fluence	82
Figure 6.3 Carrier concentration of DLC and S-DLC films versus % atomic ratio of S/C at difference substrate temperatures at 10 J/cm ² and 20 J/cm ² laser fluence	85
Figure 6.4 Hall mobility of DLC and S-DLC films versus % atomic ratio of S/C at difference substrate temperatures at 10 J/cm ² and 20 J/cm ² laser fluence	87
Figure 6.5 Example of <i>n</i> and <i>k</i> values of DLC films	88
Figure 6.6 Energy band gap of DLC and S-DLC films measured by UV-VIS	89
Figure 6.7 Energy band gap of DLC and S-DLC films measured by SE	90
Figure 6.8 Morphology of S-DLC films on the silicon substrate determined by SEM at 1% sulphur molar percentage with 10 J/cm ² laser fluence and various substrate temperatures; (a) room temperature, (b) 150 °C, and (c) 250 °C	92
Figure 6.9 Morphology of S-DLC films on the silicon substrate determined by SEM at room temperature with 0% sulphur molar percentage and 2 laser fluences; (a) 10 J/cm ² , and (b) 20 J/cm ²	93
Figure 6.10 Morphology of S-DLC films on the silicon substrate determined by SEM at 250 °C substrate temperature and 10 J/cm ² laser fluence and various sulphur molar percentages; (a) 1%, (b) 5%, (c) 10%, and (d) 25%	94
Figure 6.11 Film thickness versus sulphur molar percentages at different substrate temperatures and laser fluence.....	95
Figure 6.12 Cross-sectional SEM analysis of an S-DLC film on a silicon substrate...	96
Figure 6.13 Raman spectra of a DLC film, a diamond film and the graphite target with excitation wavelength 514 nm.	100
Figure 6.14 Raman spectra of DLC and S-DLC films at different sulphur molar percentages deposited at room temperature and 10 J/cm ² of laser fluence.....	100

Figure 6.15 Raman spectra of S-DLC films at different substrate temperatures with 10 J/cm ² laser fluence at (a) 0% sulphur molar percentage, and (b) 25% sulphur molar percentage	102
Figure 6.16 Raman spectra of S-DLC films at different laser fluence at room temperature with (a) 0% sulphur molar percentage, and (b) 25% sulphur molar percentage.....	103
Figure 6.17 Example of Raman spectrum fitting of an S-DLC film.....	104
Figure 6.18 Plot of G-peak position versus sulphur molar percentages at different substrate temperatures at 10 J/cm ² and 20 J/cm ² laser fluence.....	105
Figure 6.19 Plot of I_D/I_G ratio versus sulphur molar percentages at different substrate temperatures at 10 J/cm ² and 20 J/cm ² laser fluence.....	107
Figure 6.20 % Atomic ratio of S/C of S-DLC films versus sulphur molar percentage at different substrate temperatures and laser fluence.....	108
Figure 6.21 SIMS depth profile of an S-DLC film	108
Figure A. Raman spectra for DLC and S-DLC films at different percentages of sulphur deposited at (a) room temperature and 10 J/cm ² laser power (b) room temperature and 20 J/cm ² laser power (c) 150°C and 10 J/cm ² laser power (d) 150°C and 20 J/cm ² laser power (e) 250°C and 10 J/cm ² laser power (f) 250°C and 20 J/cm ² laser power.....	129
Figure B Example of an EDX spectrum from a S-DLC film.....	130

CHAPTER I

INTRODUCTION

1.1. Motivation of This Dissertation

Diamond-like carbon (DLC) films have become interesting for commercial applications due to their useful properties that can be modified to be similar to those of diamond, and which can be adjusted to suit each application [1-4]. Moreover, because DLC films can be produced easier than diamond films, this means that DLC film production has many advantages over diamond films. The unique properties of DLC films include: high mechanical hardness, high thermal conductivity, chemical inertness and high transparency in the visible and infrared (IR) spectral region. All of these properties can be adjusted by changing the deposition conditions and deposition techniques. These films, therefore, have been used in several mechanical, electrical and optical applications. Some examples of the use of DLC films are: cutting and abrasive wear tools, coatings for sunglasses and IR windows, computer hard-disk coatings, flat-panel displays, anti-reflective coatings on optics, and coatings for medical implants [3-8].

Recently, increasing attention has been focused on DLC films that contain carbon and another element; such as nitrogen, phosphorus and sulphur, for use in electronic and mechanical applications. For example, nitrogen and carbon (CN_x) compounds have been produced as thin amorphous films by several methods [9-14]. The most reported CN_x compounds are non-crystalline, although crystalline carbon nitride (C_3N_4) is also the subject of a lot of research effort [15]. This C_3N_4 compound is predicted to be harder than diamond, and therefore it may be suitable to use in mechanical applications.

The main objective of research into phosphorous-doped DLC films was to produce crystalline films of the thermodynamically stable compound, for example: phosphorus carbide or carbon phosphide (C_3P_4). However, making crystalline films has proved unsuccessful to date, and only amorphous films have been reported. There are few reported phosphorous-doped DLC films, which showed that the effect of phosphorous helps to increase the conductivity on DLC films [16-18].

Similarly, it may be possible to make a solid material C_xS_y films by the addition of a sulphur-containing gas during deposition. In previous work [19], carbon disulfide (CS_2) was used as a convenient source of C and S. The CS_2 was converted to become a black solid by heating. This black solid in form of powder was studied the electrical properties. It had an energy band gap of 1.7 eV and conductivity of $10^{-8} \Omega^{-1}\cdot\text{cm}^{-1}$ at room temperature. In later work, a hot filament reactor was used to decompose CS_2 [20]. It was found tricarbon sulfide (C_3S) composition produced films with electrical conductivity above $10^2 \Omega^{-1}\cdot\text{cm}^{-1}$. In later work, an inductively-coupled radio frequency plasma-polymerisation method was used to decompose CS_2 to be a cathode material for rechargeable batteries [21]. In next work, hydrogenated amorphous carbon-sulphur alloys were produced in a capacitively-coupled radio frequency reactor by decomposing 3.5% CH_4/H_2S in 96.5% Ar at 0.5 Torr [22, 23].

Recently, there have been reports of thin films of C-S-H for use in semiconductor applications. Amorphous hydrogenated carbon-sulphur thin films (a-C:H:S) were produced by capacitively-coupled radio frequency reactor from CH_4/H_2S [24]. The distribution of C and S was found to be homogeneous throughout the films. The energy band gap and refractive index values of films were in the range of 1.5-2.5 eV and 1.8-2.1, respectively. However, despite their potential semiconductor applications, there has been little work on sulphur doped diamond-like carbon (S-DLC) films. Therefore, to study the properties of S-DLC films has been a primary interest of this dissertation.

There have been many techniques used to deposit DLC films, for example; chemical vapour deposition (CVD) [6, 7, 25-27], molecular beam epitaxy (MBE) [28], sputtering [9, 29] and pulsed laser deposition (PLD) [1-5, 8, 11, 30-39]. In this dissertation, the technique of PLD is the main interest due to its high quality film production. PLD is applicable to almost any material, in particular to compounds that are difficult or impossible to produce in thin-film form by other techniques. And to our knowledge, there is no prior literature published regarding this PLD method used to deposit S-DLC film.

In this dissertation, therefore, we are interested in studying the properties of S-DLC films deposited by PLD techniques. The effect of sulphur-doped DLC films, in an attempt to fabricate an n-type semiconductor material, is the main topic in this dissertation. Electrical, optical, mechanical and structural properties were studied and reported.

1.2. Aim of This Dissertation

The aim of this present work is to use the technique of PLD to make amorphous carbon–sulphur (a-C:S) thin films with a range of S:C ratios, and to study their electrical, optical, mechanical and structural properties.

1.3. Dissertation Outline

The present thesis is organized as follows: In the remaining part of Chapter 1 is an introduction which describes the motivation of this dissertation and describes why I am interested in studying the properties of DLC and S-DLC films. The aim and outline of this dissertation are presented.

Chapter 2 introduces the allotropes of carbon, diamond and graphite, as well as DLC films - the main topic of this dissertation. The fundamental properties and applications of DLC films are reviewed, including a literature review of DLC doping and amorphous carbon alloys films.

Chapter 3 describes the PLD technique that was used to synthesize DLC and S-DLC films. The choice of lasers for film growth (particularly, the ArF excimer laser) is discussed. Pulsed laser ablation and deposition are described as well as the characteristics of the PLD process and the problem of particulates.

Chapter 4 describes the experimental set-up and the conditions for the deposition of DLC films and S-DLC films.

Chapter 5 contains the basic techniques used to characterise thin films. These include Laser Raman Spectroscopy, Spectroscopic Ellipsometry, Ultraviolet-Visible Spectroscopy, Linear Four-Point Probe measurement, Hall Effect measurement, Scanning Electron Microscopy, Energy Dispersive X-ray spectroscopy, Secondary Ion Mass Spectrometry and Nanoindentation.

Chapter 6 describes the experimental results. These results are discussed and are compared with other findings in the literature.

Chapter 7 contains a summary and conclusions of the present dissertation. Suggestions for future work are presented.

CHAPTER II

DIAMOND-LIKE CARBON

DLC films have been intensively studied and widely used in commercial applications due to their useful properties, which lie between those of diamond and graphite [1, 4]. However, much research still needs to be done to further improve their properties. This chapter introduces DLC films through their properties and commercial applications. DLC films are a form of amorphous carbon, which contains regions that are diamond-like and regions that are more graphite-like in structure. Therefore, to understand DLC, it is important to first understand the properties of these two allotropes. Modifying the properties of DLC films allows them to be used in a variety of industrial applications. Doping is the main method to modify the electrical properties of the films for electrical applications. Doping can be both n-type and p-type increasing the electrical conductivity from highly insulating to semiconducting. In particular, sulphur-doped DLC showing n-type semiconductivity is the main topic of this study.

2.1. Allotropes of Carbon

Apart from the fullerenes and nanotubes, carbon has generally two crystalline allotropes, graphite and diamond, with the carbon atoms bonded by sp^2 and sp^3 hybridization, respectively. The difference in the type of hybridization and the structure of carbon results in the different properties of these two allotropes [7, 40-45].

2.1.1. Graphite

Graphite is the most abundant and stable allotrope of carbon found naturally, and is a hexagonal close-packed (h.c.p) crystal with the carbon in sp^2 hybridization. The carbon atoms form three σ bonds due to overlap of three sp^2 superimposed orbitals, and a π bond from the interaction of p orbitals. This creates a stable trigonal back-bone crystal structure where each C is covalently bonded with three neighboring carbon atoms in the same plane. Each C shares an electron with another C atom in an adjacent plane, forming a weak van der Waals' bond [40]. This allows the two graphene planes to slip over each other. The in-plane C-C distance is 0.142 nm whereas the inter-plane C-C distance is 0.341 nm [46]. The crystalline structure of graphite with three graphene planes is shown in Figure 2.1. The configuration of sp^2 hybrid orbitals in graphite is shown in Figure 2.2.

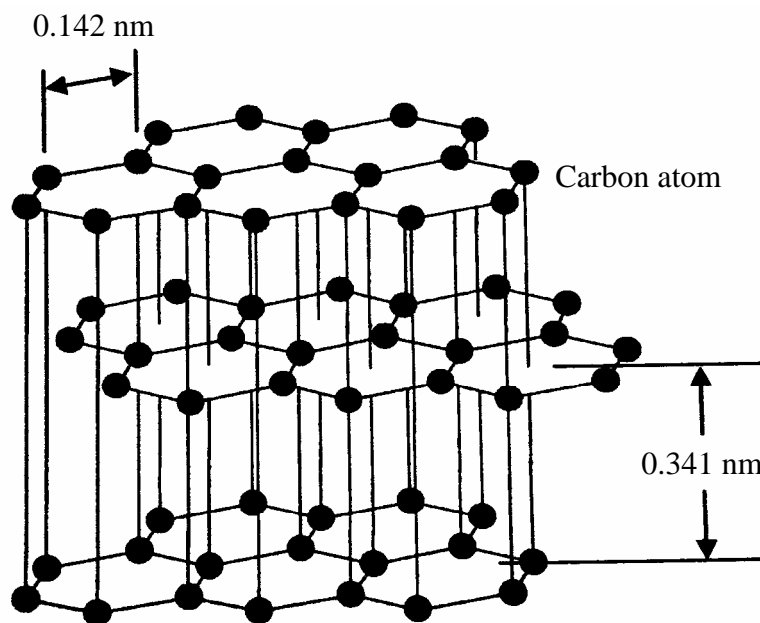


Figure 2.1 Crystalline structure of graphite with three graphene planes [40, 46].

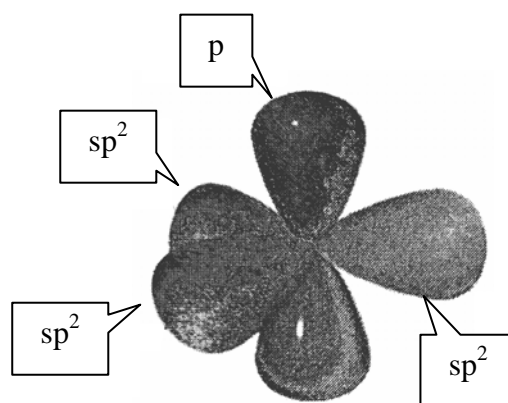


Figure 2.2 Configuration of sp^2 hybrid orbitals in graphite [46].

Due to the structure of graphite, the inter-plane C-C interactions are weak and contain mobile electrons. These give graphite its unique properties, such as being a good electrical conductor, good thermal conductor, low thermal expansion coefficient, soft, chemically active, non-oxidizable and optically opaque. Thus, it is suitable to use as a lubricant [40, 41].

2.1.2. Diamond

Diamond is the strongest material in nature, and has C arranged in a face-centered cubic (f.c.c.) structure with sp^3 hybridization [40]. The C exhibits a metastable tetragonal-bonded crystal structure with four strong covalent σ bonds [40]. The C-C distance is quite short, ~ 0.154 nm. Therefore diamond has a strong chemical bond leading to a strong, rigid molecular structure at the macroscopic level [46]. The crystalline structure of diamond and the configuration of its sp^3 hybrid orbitals are shown in Figures 2.3 and 2.4, respectively.

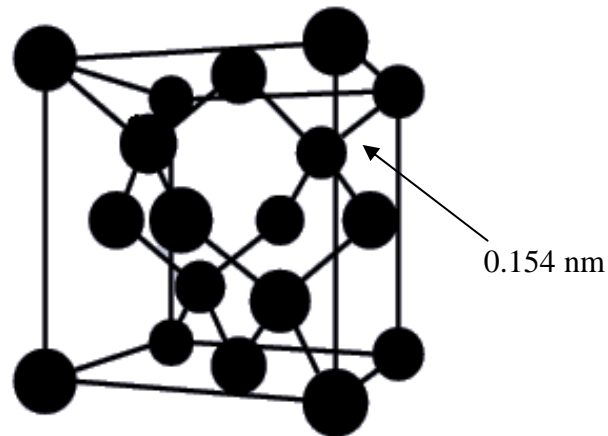


Figure 2.3 Crystalline structure of diamond [40, 46].

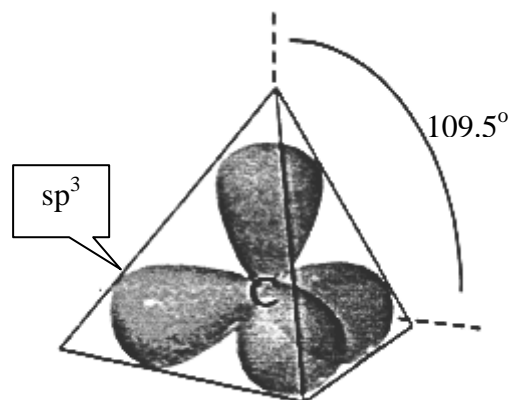


Figure 2.4 Configuration of sp^3 hybrid orbitals in diamond [46].

The strong directional sp^3 bonding gives diamond its unique properties, such as highest elastic modulus, extreme hardness, highest thermal conductivity of any solid at room temperature, high resistivity at room temperature, very low thermal expansion coefficient, low coefficient of friction, high chemical stability and resistance, large optical band gap, and transparency in the infrared (IR) and near-infrared range [1, 40, 41, 47]. As a result, diamond, either in the form of powder, grit or films, can be used in many industrial applications, including in mechanical, electrical and optical applications. Some applications of diamond are shown in the Table 2.1.

Properties	Applications
High hardness	Abrasive coatings and cutting tools
Transparency to IR	Infrared laser windows
Large band gap	Semiconductor devices
High thermal conductivity	Semiconductor device heat sinks

Table 2.1 Some applications of diamond [1, 40, 41, 47-50].

2.1.3. Properties of Diamond and Graphite

The different structure and hybridization of diamond and graphite cause the difference in their properties. The in-plane C-C bond in graphite is shorter than C-C bond in diamond. Therefore, the short in-plane C-C bonds give graphite a higher thermal and electrical conductivity than diamond when measured along the graphene planes [40]. However, the thermal and electrical conductivity perpendicular to the planes are very low by comparison because of the weak van der Waals' bonding. This shows that graphite is a semimetal. Apart from thermal and electrical conductivity, graphite and diamond have many other differing properties. A comparison of properties of graphite and diamond are shown in Table 2.2.

Properties	Graphite		Diamond
	In plane	Transverse	
Lattice constant (at RT) (Å)	2.462	6.708	3.567
Bond length (at RT) (Å)	1.421	3.410	1.545
Bond strength (kJ·mol ⁻¹)	~524	~7	~349
Thermal conductivity (W·m ⁻¹ ·K ⁻¹)	<4180	2	~2000
Electrical resistivity (Ω·cm)	10 ⁻⁴	1	>10 ¹⁴
Debye temperature (K)	2500	950	1860
Electron mobility (cm ² ·V ⁻¹ ·s ⁻¹)	20 × 10 ³	100	2200
Hole mobility (cm ² ·V ⁻¹ ·s ⁻¹)	15 × 10 ³	90	1600
Dielectric constant	-	2.6	5.7
Refractive index	1.8	2.15	2.42
Transparency	Opaque		UV-VIS-IR
Melting point (K)	4200		4500
Band gap (eV)	~0.04		5.45
Density (g·cm ⁻³)	2.267		3.515
Fraction of hybrid orbital	100% sp ²		100% sp ³
Hardness (GPa)	soft		79-102
Electric breakdown field (V·m ⁻¹)	-		10 ⁹

Table 2.2 Some properties of graphite and diamond [40, 41, 47]. RT = room temperature.

2.2. Amorphous Carbon and Diamond-Like Carbon

In addition to the crystalline phases of carbon, graphite and diamond, carbon can also form amorphous phases. These phases have a range of $sp^2:sp^3$ C contents, and therefore a range of properties. The ones with low sp^3 C content are generally termed *amorphous carbon* (a-C), and these are usually soft and electrically conducting. A definition of a-C is [51]: “A carbon material without long-range crystalline order. Short range order exists, but with deviations of the interatomic distance and/or interbonding angles with respect to the graphite lattices as well as to the diamond lattice.”

Diamond-like carbon

The phases of a-C with high sp^3 content have properties very close to those of diamond [52], and so are often called *diamond-like carbon* (DLC) [40]. DLC films are relatively easy and economical to deposit and can be deposited over a large area. A definition of DLC is [51]: “Diamond-like carbon films are hard, amorphous films with a significant fraction of sp^3 -hybridized carbon atoms and which can contain a significant amount of hydrogen. Depending on the deposition conditions, these films can be fully amorphous or contain diamond crystallites. These materials are not called ‘diamond’ unless a full three-dimensional crystalline lattice of diamond is proven.”

The two definitions above (a-C and DLC) were given by The International Union of Pure and Applied Chemistry (IUPAC), who specify that a-C films and DLC films are synonymous expressions. DLC films are a range of metastable amorphous materials containing a mixture of sp^2 and sp^3 hybridized carbon. The differences in both structures and chemical bonds between sp^2 and sp^3 hybridized carbon produce the variation of the properties of DLC films. The ratio of $sp^3:sp^2$, therefore, indicates the specific property of each DLC film [5-8, 47, 52, 53]. The carbon hybridization ratio ($sp^3:sp^2$) in these films can be between 0% to 85%. Films with high sp^3 C content have properties such as high mechanical hardness, high electrical resistivity, low friction coefficient, IR transparent and chemical inertness

[31, 32, 40, 41, 43]. These properties give DLC a variety of uses, from protective coatings on optical windows, medical implants or hard drives, to MEMS devices [31]. The structure of a DLC film is shown in Figure 2.5

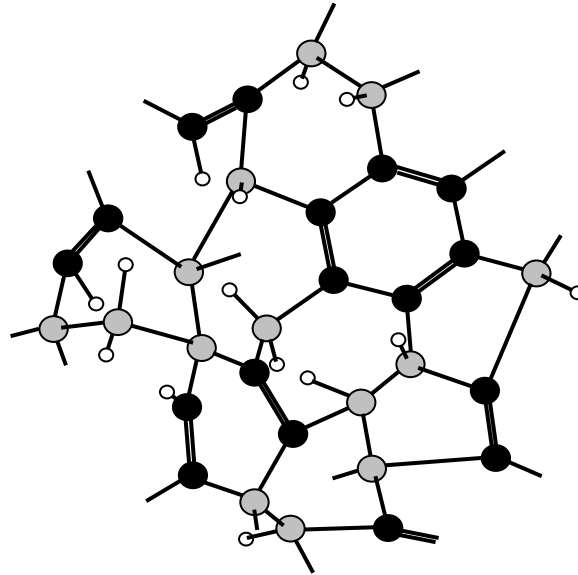


Figure 2.5 Structure of a hydrogen-containing diamond-like carbon film. The black spheres represent C atoms with 3 bonds (sp^2), the gray spheres represent C atoms with 4 bonds (sp^3), and the small white spheres represent hydrogen [47].

DLC films can be separated into two types by hydrogen content [47]. Some DLC films use H_2 gas during formation, as hydrogen will help to reduce the dangling bonds in the amorphous structure. Thus, some of the sp^3 bonding in hydrogenated amorphous carbon is formed from carbon-to-hydrogen atoms. The hydrogen-containing DLC films are called *hydrogenated amorphous carbon* (a-C:H), *hydrogenated diamond-like carbon* (HDLC) or *diamond like hydrocarbon* (DLHC). These films have typically less than 50% of C sp^3 fraction [50]. They have lower refractive index values and density values. Moreover, they have an infrared absorption band [1, 50].

DLC produced under H-free conditions does not contain any hydrogen. Therefore, these films do not have an infrared absorption band and the film is a mixture of C-C sp , sp^2 and sp^3 bonds. The high density, Young's modulus and hardness of DLC are all a consequence of the amount of C-C sp^3 bonding. Hydrogen-free DLC films are sometimes called *tetrahedral amorphous carbon* (ta-C) [34, 50, 54], *amorphous carbon* (a-C) [55-57], *amorphous diamond* (a-D) [2] or *hard carbon* [58], and can contain up to 85% of C sp^3 fraction [50].

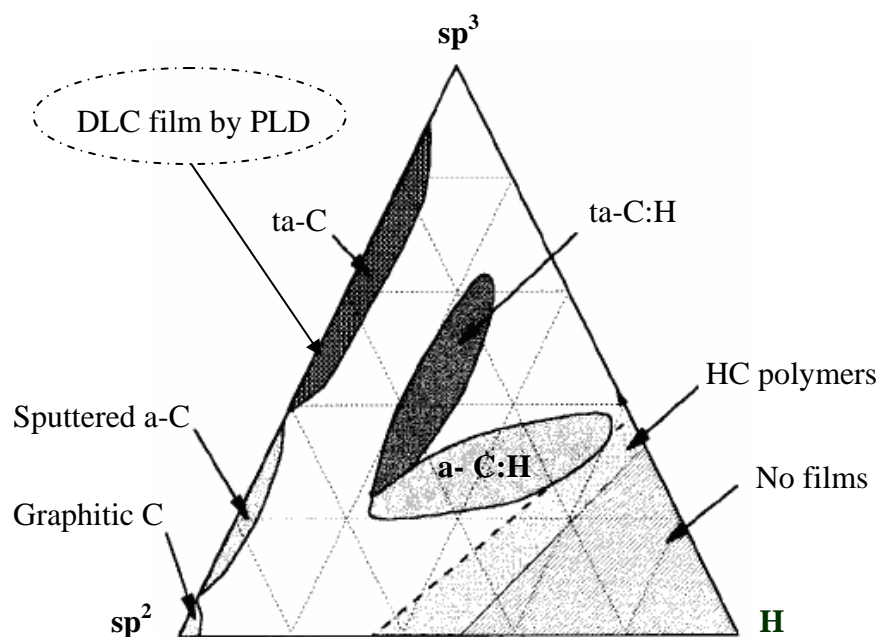


Figure 2.6 Ternary phase diagram of amorphous carbon films [52].

DLC is best explained using a ternary phase diagram, as shown in Figure 2.6. Pure crystalline graphite is at the extreme left-hand corner, while diamond is at the top corner. H content increases moving towards the right-hand side. The composition and resulting properties of the carbon film are a direct result of the C:H content plus the $sp^2:sp^3$ C ratio. Thus, the properties of a carbon film can be tailored to a specific application by adjusting these values during deposition.

2.2.1. The Synthesis of DLC

DLC was first produced by ion beam deposition by Aisenberg and Chabot, and was a mixture of microcrystalline diamond and hydrogenated amorphous carbon [41, 47]. Since then, a number of other techniques have been developed to deposit a-C and DLC films. These methods are divided into two types: (a) Plasma-enhanced chemical vapor deposition (PECVD) dissociates hydrocarbon gas mixtures by a plasma discharge, and accelerates the C fragments onto a substrate. (b) Sputtering or pulsed laser deposition (PLD) use a solid carbon source with no H₂ present to physically eject C atoms from the target which then deposit onto a substrate. All deposition methods are non-equilibrium processes that are concerned with the interaction of highly energetic ions with the surface of the films [2, 38]. DLC can also be deposited on a variety of substrates such as silicon, stainless steel, ceramics, organic polymers and plastics, and glass [3, 59].

2.2.2. DLC Deposition Mechanism

The growth mechanism of DLC can be explained by a shallow subsurface implantation (subplantation) model [60], in which (hydro)carbon ions (C⁺, C₂⁺, CH⁺, *etc.*) impact on and implant into the growing surface.

(1) The energetic C ion penetrates the target surface

The ion energy and the nature of the target determine how deep the ions penetrate. If the ion energy is below a threshold penetration energy (E_p), the ions stay on the surface (but the ion are neutralized by electrons from the bulk) leading to island formation. If the ion energy is above E_p , ion penetration can occur in two ways. First, the ion can pass directly through the surface layer and become implanted as shown in Figure 2.7(a). Second, the ion can displace an atom in the first layer, knocking it deeper into the bulk, while itself remaining on the surface (Fig. 2.7(b)).

(2) The energy loss of ions

The excess ion energy will be lost in three mechanisms; atomic displacement, phonon excitation and electron excitation. The latter two can be combined as “thermal spikes”.

(3) The addition of the ion into the film

If the substrate is below a critical temperature (T_c), the addition of the ion into the film produces an increase of density, since implantation occurs with little increase in film volume. Above T_c , the implanted ions/atoms have enough thermal energy to restructure (anneal) to a more stable, lower density form. These effects usually produce more sp^2 bonding and highly graphitic films.

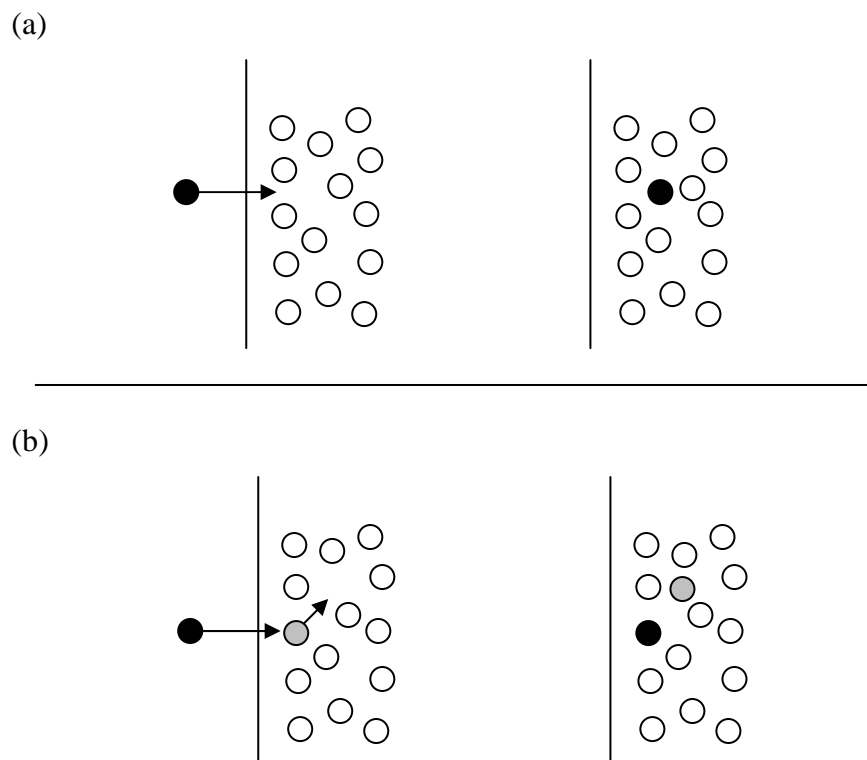


Figure 2.7 Impact of an ion on a substrate, showing (a) direct penetration, and (b) penetration by displacement.

DLC films with the highest sp^3 proportions can generally be deposited by ions with an impact energy of 100 eV per carbon ion [61]. However, if the impact energy is lower or higher than this energy, the DLC films will become more graphitic. Thus, there are three deposition regimes:

(a) If the impact energy is too low, the ion cannot penetrate the surface. It simply sticks on the surface and forms an amorphous carbon layer.

(b) If the impact energy is ~ 100 eV, the probability of the ion penetrating the surface also increases, with the effect of increasing the local density. Because sp^3 hybridized C is more stable at high density, these ion impacts produces more sp^3 carbon.

(c) But as the ion energy is increased above ~ 100 eV, only a fraction of the energy is used to allow the ion to penetrate the surface. The excess energy is lost as heat within the DLC films, and this large, rapid thermal spike allows the structure to anneal into a more stable sp^2 form. Thus, these higher energy impacts lead to the film becoming more graphitic.

2.2.3. Properties of DLC

Each type of DLC will have different properties, as these depend on the structure and hybridization of carbon. The properties of DLC and other phases of carbon are shown in Table 2.3.

Material	sp^3	H	Density	Bandgap	Hardness
	/ (atomic %)		/ ($g\cdot cm^{-3}$)	/ eV	/ GPa
Diamond	100	0	3.515	5.5	100
Graphite	0	0	2.267	-0.04	-
Glassy C	0	0	1.3-1.55	0.01	2-3
Evaporated C	1	0	1.9-2.0	0.4-0.7	2-5
Sputtered C	5	0	2.2	0.5	-
ta-C	80-88	0	3.1	2.5	80
a-C:H (hard)	30-60	10-40	1.6-2.2	0.8-1.7	10-20
a-C:H (soft)	50-80	40-65	1.2-1.6	1.6-4	<5
ta-C:H	70	30	2.4	2-2.5	50
polyethylene	100	67	0.92	6	0.01

Table 2.3 Properties of some phases of carbon [40, 41, 60].

2.2.3.1. Electrical Properties

The electronic structure of DLC films can be described in terms of their density-of-electron-states, which is a function of energy $N(E)$. The Fermi level (E_F) separating the filled and empty states is placed at $E = 0$, as shown in the schematic electronic band structure in Figure 2.8.

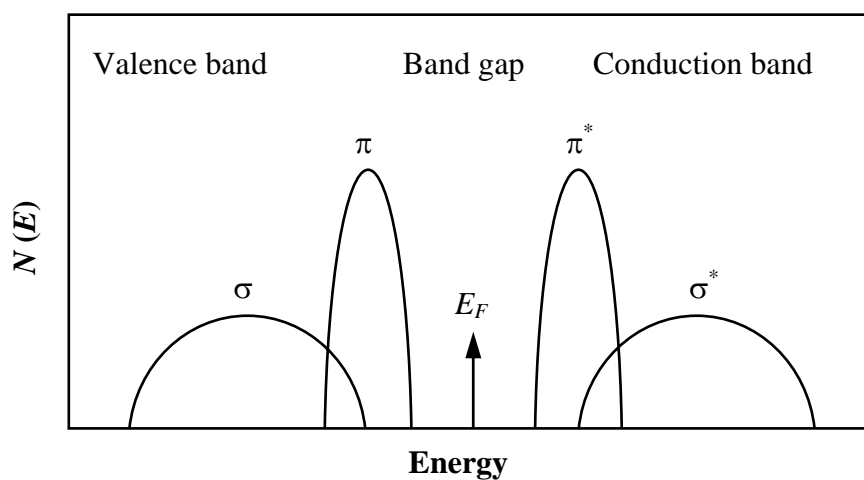


Figure 2.8 Density-of-electron-states for a DLC film [41].

The C-C and C-H σ -bonds form filled σ states in the valence band and unoccupied σ^* states in the conduction band. The σ -states are separated by a wide σ - σ^* band gap of at least 5 eV. π and π^* states are formed close to the Fermi level by the π -bonds of sp^2 and sp carbons. The π - π^* band gap is much narrower than the σ - σ^* band gap. The arrangement of sp^2 sites in the film is a crucial factor in the properties because these sites lie closest to E_F . Any alteration of the nature of the π bonding by graphitization, development of clustering and/or re-orientation, will thus have an effect on the density-of-electron-states, and therefore on the electronic properties and effective band gap of DLC films [41].

The electrical properties of DLC films vary between those of a semimetal (graphite) to a wide band gap insulator (diamond). Although DLC has a band gap in the range of 1-4 eV, it does not behave like a typical semiconductor [50]. The gap structure of DLC is only ‘mobility gap’ in that carriers residing in gap-states are localized, which produce behavior similar to that of a semiconductor. Electronic transport in DLC films is quite complex as a result of their disordered structure. The mobility and electrical resistivity of DLC and ta-C films at room temperature are generally characterised in the range of 10^{-11} - 10^{-12} $\text{cm}^2\cdot\text{V}^{-1}$ and 10^2 - 10^{16} $\Omega\cdot\text{cm}$, respectively, and depend upon the deposition conditions [50].

2.2.3.2. Optical Properties

Optical properties of DLC films will normally depend on the deposition techniques, deposition conditions and hydrogen content [1, 24, 28, 36, 39, 41, 43, 50, 56, 62]. DLC films are typically transparent in the infrared, are weakly absorbing in the visible region, and are increasingly absorbing with decreasing wavelength in the ultraviolet (UV). Hydrogen content in DLC films causes the loss of infrared transparency at 2900 cm^{-1} [1, 50], due to absorption by C-H vibrational modes.

Optical band gap (E_g) values of DLC films measured by the Tauc method [63] (see Section 5.3), are normally in the range from 0.38 to 2.72 eV and depend upon the deposition conditions [50]. E_g increases with increasing hydrogen content as the mid-band-gap π -states are reduced when the H forms sp^3 bonds to C. As the refractive index, n , and extinction coefficient, k , are affected by the hydrogen content, these will also decrease with increased concentration of bound hydrogen. A higher n will usually indicate DLC with high hardness and better wear resistance [50]. Normally the dielectric constant of a diamond film is 5.6, while DLC film have a dielectric constant in the range of 2.7-3.8, depending upon the deposition conditions [50].

2.2.3.3. Mechanical Properties

The outstanding mechanical properties of DLC films, such as high elastic modulus and hardness, low friction coefficient, low wear rate and low roughness, can be controlled by the sp^3 carbon content.

The hardness of DLC films is generally in the range of 10 to 20 GPa, depending upon the deposition conditions. DLC films with a higher sp^3 content are generally more diamond-like in character, so are harder, have a lower friction coefficient and a lower wear rate. However, these films often suffer from stress problems. Although DLC films have superb properties, their production has an important drawback due to a limitation of the thickness to which they can be deposited. In general, softer films with low sp^3 C content can be deposited thicker than the harder films with high sp^3 content, which often delaminate above thicknesses of a few micrometre mainly due to stress-related problems [34].

2.2.4. Applications of DLC Films

Due to the superb properties of DLC films, they are used in many applications, including electrical, optical and mechanical applications, as shown in Table 2.4.

Properties	Applications
High hardness, wear resistance	Cutting and abrasive wear tools
Low wear rate, high hardness, optical and IR transparency	Coatings for sunglasses and IR windows
High hardness, low wear, smoothness	Computer hard disk coatings
High hardness, scratch resistance	Watch cases, lens
Low electron affinity	Flat panel displays
High refractive index	Anti-reflective coatings on optics
Chemical inertness, biocompatibility, hardness, smooth	Coatings for medical implants, e.g. artificial hip joints

Table 2.4 Some applications of DLC films with the required properties [1, 50].

2.3. Doping of Diamond and Diamond-Like Carbon

The ability to tune the band gap of DLC films between 0 and 4 eV makes it a promising material for electronic devices [40, 50]. However, pure DLC normally contains a low carrier concentration. Therefore, researchers have attempted to enhance their electrical properties by doping DLC with foreign atoms to increase the carrier concentration. This can be achieved by either increasing the number of free electrons or creating free holes to improve the conductivity [64-68].

Doping is usually achieved by substituting atoms from the host lattice with impurity atoms from neighboring groups in the Periodic Table. The dopant atoms create isolated defect states in the gap between the valence and conduction band. Carriers can ‘hop’ between these mid-band-gap states, forming a conduction pathway. The more states that are present, the better the conduction. Eventually the states can overlap to form a continuous band, allowing efficient conduction.

Concerning crystalline diamond films (not DLC), most previous work has concentrated on doping both p-type and n-type. There are many reports which show that p-type doping of diamond films using boron is easily achieved, and the electrical conductivity can be controlled by the boron content from highly insulating to near-metallic [69]. However, n-type doping of diamond is more difficult due to the physical size of the potential dopant atoms (P, N and S) compared to the small, rigid diamond lattice. Although n-type doping has been achieved using N and P, the electronic properties of the resulting film are still not ideal for device applications, since the defect energy levels are too deep. So the search is still on to find a shallow n-type dopant for diamond [40, 68, 70].

In theory, DLC should be easier to dope than diamond because it has a narrower band gap, so dopants can only form shallow levels. However, there are few reports about doping of DLC films due to numerous experimental difficulties encountered. First, DLC films have a low doping efficiency for most of the common dopant atoms [40, 50]. This is because the loosely defined bonding of the random carbon network allows the dopant atoms to exhibit their chemically preferred valence, with their outer shells fully saturated (*i.e.* there are no ‘spare’ electrons or holes) [71]. Also, incorporation of other elements helps to increase the proportion and clustering of sp^2 bonds due to reducing both the lattice strain and the density [18]. In other words, adding dopant atoms often results in localised graphitisation of the DLC film. Another problem is that the density of defects in a-C/DLC films is too high for most electronic device applications (*e.g.* 10^{20} cm^{-3} in ta-C compared to 10^{16} cm^{-3} in hydrogenated amorphous silicon (a-Si:H)) [52, 60]. As a result, there are very few reports of successful p-n junction devices made from DLC [72, 73].

2.3.1. P-Type Doping

Normally, p-type doping is achieved by replacing some atoms in the film with another which has one less valence electron [40]. An electron from the valence band is excited into this empty state, creating a mobile 'hole' in the valence band. Mobile carriers like this hole (or acceptor) allow electrons to flow through the material [68, 74]. Analogous to the conventional dopants used in Si, elements from group III, boron and iodine, have been studied as potential acceptors in carbon films [65, 75, 76]

It was found that boron incorporation into diamond created an empty level 0.37 eV above the valence band [72, 75]. The activation energy for transport and resistivity decreased with increasing boron incorporation. Similarly for ta-C films, Kleinsorge *et al.* [75] showed that boron doping increased their conductivity by five orders of magnitude (10^{-6} to $0.1 \Omega^{-1}\cdot\text{cm}^{-1}$), without changing the band gap.

Iodine doping of DLC films also produced a decrease in the band gap (3.5 to 1.9 eV). In this case, the decrease in the band gap coincided with an increase in the electrical conductivity (8.26×10^{-4} - $2.76\times 10^{-2} \Omega^{-1}\cdot\text{m}^{-1}$), due to the reduction of sp^3 -bonded carbon [77].

2.3.2. N-Type Doping

Usually, n-type doping is achieved by replacing some atoms in the film with ones which have one extra valence electron [40]. Again, analogously to the conventional dopant used in Si, elements from group V (nitrogen and phosphorous) and group VI (sulphur) have been studied as potential 'electron donors' in diamond [65, 68, 70, 78]. There are reports that N and P are single donors on substitution sites while S should behave as a double donor [68].

It was found that N cannot be used as a donor atom in diamond films since the activation energy of N is 1.7 eV lower than the conduction band of diamond. A shallow level, therefore, cannot occur. Nitrogen also causes the distortion of the diamond film structure [79, 80].

It was found that the activation energy for P in diamond films is 0.6 eV below the conduction band. Hence the P doping produces a lower activation energy than N doping. Another difficulty is that the P incorporation is obtained preferentially on (111) oriented surfaces of diamond. Also, because of the high ionization energy of P, the carrier concentration in the conduction band is very low and the resistivity is very high. The carrier mobility is also low, $< 250 \text{ cm}^2 \cdot \text{V}^{-1} \cdot \text{s}^{-1}$ [32, 78, 81].

S has also been used as a potential n-type dopant in diamond films, and the original reports [25, 68, 81, 82] raised great excitement when apparently n-type films were produced with low activation energies. However, later measurements showed that these results arose from inadvertent contamination from boron [68, 81]. The case for S as an n-type dopant in diamond has still to be proven.

2.3.3. a-C Alloys

Although little work has been done to dope a-C films with elements such as B, S, P and N, there has been a lot of work trying to make amorphous and crystalline alloys of C using these elements. Some of the more important findings are detailed below.

2.3.3.1. CN_x Films

In 1989, Liu and Cohen predicted the existence of a super-hard carbon nitride solid. This motivated extensive world-wide experimental and theoretical research to synthesize such a compound. From minimum energy calculations, CN_x compounds were generally accepted to be metastable under standard conditions [83]. Therefore, the formation of these super-hard phases needs to be sought in non-equilibrium processes. CN_x was claimed to have been produced as thin amorphous films by several methods, such as radio frequency plasma deposition [9, 10] pulsed laser deposition [11], ion-beam-assisted deposition [12], ion implantation [13] and magnetron sputtering [14]. The name ‘CN compounds’ have been widely used to represent the ideal composition of C₃N₄ but most reported CN compounds are non-crystalline [15]. More recently, in work of Yang and Wang, carbon nitride

nanocrystals with a cubic structure were prepared by using a pulsed laser induced liquid-solid interfacial reaction [84]. Another step forward was made by Yin *et al.* [85], who synthesized highly crystalline β -carbon nitride nanorods using a combination of mechanically ground graphite nanoparticles and high temperature chemical reactions. Yang *et al.* [86], developed the technique further, and deposited ultrafine crystalline carbon nitride powder, nanopowders and nanorods by the novel method of pulsed laser ablation of a graphite target in liquid ammonia solution at room temperature and pressure.

2.3.3.2. CP_x Films

There have been relatively few reports of P doping of DLC films [16-18, 87-90]. In work of Verramy *et al.*, the filtered cathodic arc method was used to produce P-doped DLC films. They found that DLC films incorporated up to 1% P, and the resistivity of the films was reduced by 6-7 orders of magnitude with no apparent change to the amorphous nature of the carbon films [17]. Capacitively-coupled radio frequency (r.f.) plasma deposition has been used to produce P-doped DLC films as well [16, 18]. PH_3 gas was used as a dopant gas in producing films with ~ 11% P content. The authors found that the conductivity of this film increase nearly five orders of magnitude at room temperature. In work of Galzon *et al.*, they found that incorporation ~3% P in films destabilized the tetrahedral network in favor of an sp^2 bonded network [87]. Radio frequency plasma deposition has been used to produce highly P-doped DLC films. In the work of Kuo *et al.*, CH_4 and PH_3 mixtures were used as the process gases, with PH_3 concentration up to 21% by volume. The authors found that these films had P:C ratios up to 0.9. [90]. Pearce *et al.* used a gas mixture consisting of CH_4 with addition of 0-90% PH_3 . They found that these films had P:C ratios as high as 3:1 [91].

2.3.3.3. CS_x Films

A solid material C_xS_y can be produced by the addition of a sulphur-containing gas during deposition. In previous work, CS₂ was used as a convenient source of C and S. In 1868, Loew found that carbon disulfide produced a dark precipitate on exposure to sunlight [92]. In 1910, Dewar and Jones produced polymeric (CS)_x by adding thiophosgene (CSCl₂) to tetracarbonylnickel (Ni(CO)₄) [93]. In 1941, Bridgman heated liquid CS₂ until it became a black solid with heating at 200°C at atmospheric pressure. This black solid decomposed to carbon and sulphur [94] and in 1986; Tsukamoto and Takahashi studied the electrical properties of this black solid in the form of powder. They found that it had a band gap of 1.7 eV and conductivity of 10⁻⁸ Ω⁻¹·cm⁻¹ at room temperature. The conductivity of this powder was increased to 10⁻³ Ω⁻¹·cm⁻¹ by doping with nitrogen or iodine [19]. In 1992, a hot filament reactor was used to decompose CS₂ by Spiro *et al.* [20]. They found C₃S composition in the films with electrical conductivity above 10² Ω⁻¹·cm⁻¹.

In 1996, Sathir and Schoch produced CS₂ as a cathode material for rechargeable batteries by a inductively-coupled radio frequency plasma-polymerised method [21]. Dallal *et al.*, produced hydrogenated amorphous carbon sulphur alloys in a capacitively-coupled radio frequency reactor by decomposing 3.5% CH₄/H₂S in 96.5% Ar at 0.5 Torr [22, 23]. However, there has been very little systematic work to study the properties of thin films of C-S-H for using in semiconductor applications. In 2004, Filik *et al.*, produced amorphous hydrogenated carbon-sulphur thin films (a-C:H:S) by capacitively-coupled radio frequency reactor from CH₄/H₂S [24]. They found the distribution of C and S was homogeneous throughout the films. The E_g and refractive index values of films were in the range of 1.5-2.5 eV and 1.8-2.1, respectively.

2.4. Summary

This dissertation studies the properties of S-DLC films because these films are expected to be n-type semiconductors and therefore may be of use in a range of semiconductor devices.

CHAPTER III

PULSED LASER DEPOSITION

Thin films are highly useful in the production of semiconductor and resistant coatings. However, the production of thin films containing non-volatile components has proved difficult to achieve [95]. Examples of these films include ZnO [96-98], GaN [99-101], high temperature superconductors [95], and DLC [2, 4, 5, 8, 30-33, 37, 53, 102]. As a result, in recent years, there has been a great deal of research into methods to make these types of thin films. The techniques employed have been varied, and include: chemical vapour deposition (CVD) [6, 7, 26, 27], molecular beam epitaxy (MBE) [28], sputtering [9, 29] and pulsed laser deposition (PLD) [1, 4, 8, 11, 30-36]. In this dissertation, the technique of PLD is the main interest.

Although limited to small areas, PLD offers a number of advantages over other deposition techniques. A highly focused laser beam produces extremely high energy densities (10^9 W/cm²), which allows material of almost any composition to be vaporised and deposited. This 'brute force' approach allows the deposition of a wide range of materials, and provides a large number of controllable experimental parameters, which results in a very flexible research tool.

This chapter will describe the details of the PLD technique used in this dissertation for the deposition of DLC and S-DLC films. The first section provides information on the choice of lasers used for PLD, and the basic set-up, characterisation and configuration of the laser are discussed. The second section provides information on PLD, the basic equipment, mechanisms of pulsed laser ablation and the effect of process parameters. The last section discusses the growth of DLC films by PLD.

3.1. Choice of Laser [103]

The common laser wavelengths used to grow thin films in PLD techniques lie in the range 200 to 400 nm, in the UV region of the spectrum. This is because there are few available laser sources capable of easily delivering the required high energy density ($>1 \text{ J/cm}^2$), necessary to ablate enough solid material to cover $10 \times 10 \text{ mm}^2$ areas on a substrate. Moreover, most solid materials are opaque in the UV, thus the laser power is absorbed efficiently at these wavelengths. This leads to the laser power being absorbed closer to the target surface, and hence reduces the problem of particulate formation (see Section 3.2.4).

Most laser sources for thin film deposition, to date, have been either excimers or Nd:YAG lasers. Nd:YAG lasers are a solid-state system, with fundamental wavelength 1064 nm. The neodymium ions (Nd^{3+}) are impurities within an yttrium-aluminium garnet (YAG) crystal, and serve as the active element. They are pumped optically into an upper electronic state by flash lamps. High output energies are achieved by using two YAG rods in an oscillator configuration. This configuration can produce an output up to 2 J/pulse with limited pulse repetition rate at 30 Hz. In order to produce light in the UV the fundamental frequency can be doubled or tripled by passing the beam through a suitable crystal, to give an output at 532 nm and 355 nm or 266 nm, respectively, with a concurrent drop in laser power.

An excimer laser is a gas laser system which emits radiation in the UV with high output delivering in excess of 1 J/pulse. They can achieve pulse repetition rates up to several hundred Hz with energies 500 mJ/pulse. Excimer lasers provide the most efficient source of UV laser radiation because they radiate directly in the UV without the frequency doubling or tripling required for Nd:YAG lasers.

3.1.1. Excimer Laser Basics

Excimer is a contraction of “excited dimer”, and characterises a class of molecules that accomplish the condition for generation of a population inversion. The term excimer applies correctly only to homonuclear dimers. The correct term for heteronuclear molecules is *exciplex*, which is an acronym of “excited diatomic complex”. However, the term ‘excimer’ is commonly used also for the class of exciplex molecules.

An excimer laser uses an electrical discharge to form an exciplex from a mixture of two gases. The lasing action takes place from a bound upper electronic state to a repulsive ground electronic state. The crucial feature of the gas in the lasing action is the dimer, which is only bound in the excited state. Any excited dimer, therefore, will quickly dissociate as it relaxes to the ground state following the emission of a photon. This principle is illustrated in Figure 3.1. When the dimer is formed, it will decay via both spontaneous emission and collisional deactivation. In order for lasing action to occur, the formation rate of the ionic and excited precursors must be faster than these decay process, leading to a build up of population in the upper state - a *population inversion*. Once a population inversion is achieved, emission of a photon stimulates the relaxation of the entire population at once, producing a coherent beam of light at the same frequency. Moderate output energies of several hundred mJ per laser-pulse plus an excimer lifetime of nanoseconds, dictate an excimer population density requirement of the order 10^{15} cm^{-3} . Most excimer lasers are based on inert gas halides such as ArF, or homonuclear excimers, such as F₂. A list of common excimer lasers with their associated lasing wavelength in available laser systems is shown in Table 3.1.

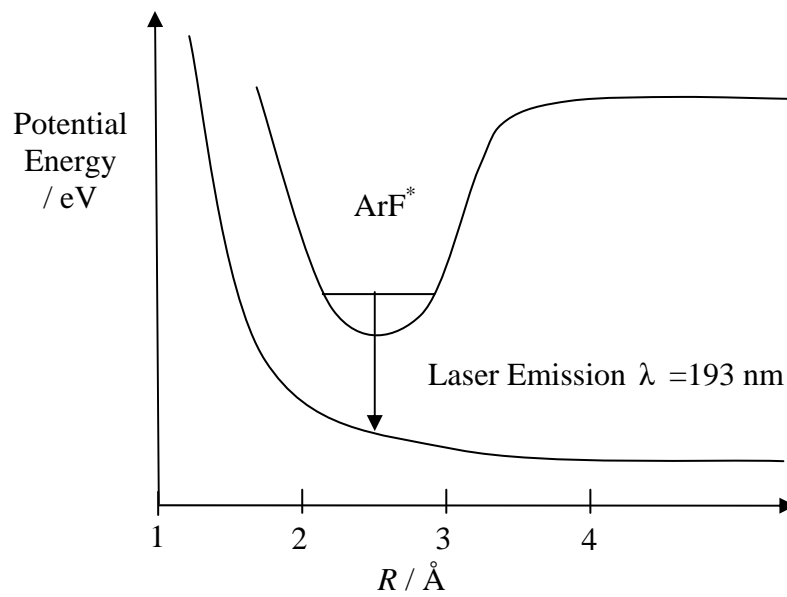


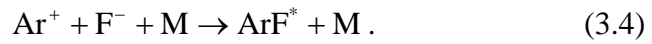
Figure 3.1 Potential energy diagram of an ArF excimer laser system [104].

Excimer	Wavelength / nm
F ₂	157
ArF	193
KrCl	222
KrF	248
XeCl	308
XeF	351

Table 3.1 Wavelengths of common excimer laser systems.

The kinetics and chemical reactions leading to the formation of the excimer molecules are complex and consist of many steps, since the reactions generally require a third body for energy transfer. For ArF lasers, the typical operating pressure is 3 atm, and the gas mixture is composed of 0.16% F₂, 6.3% Ar with the balance being Ne. The ArF excimer laser reactions are shown in Equations 3.1 to 3.5 [103].

Equations 3.1 and 3.2 show the electron-impact excitation and Penning ionisation between Ar and electrons, respectively, while Equation 3.3 is the dissociative recombination between F_2 and electrons. Equation 3.4 is the recombination of Ar^+ and F^- stabilised by a third body, M, and Equation 3.5 is the reaction of Ar^* with F_2 .



The * denotes an electronically excited species, and M denotes the buffer gas, usually He or Ne, as a third body. When the ArF^* exciplex relaxes to the repulsive potential-energy surface, as shown in Figure 3.1, it will emit a photon at 193 nm and decompose to $Ar + F$. This regenerates the original gas mixture, as shown in Equations 3.6 and 3.7.



In theory, the laser gas mixture should last forever, because the starting gas is regenerated after every excimer reaction. However, even though the starting gas is regenerated, the performance of the laser degrades with time. This is a result of two factors: some gas leaking from the laser tube, and the degradation of the highly reactive F_2 gas through reaction with the seals and the walls of the laser cavity chamber. This decrease in performance is seen by the increasing voltage necessary for operation a few days after gas refilling.

The required pulse duration of excimer lasers is about 10-50 ns for pumping using electrical discharge via fast high-voltage switches (Thyratrons). Normally, the excimer laser cavity has only a single pass to emit the photons, resulting in a highly divergent beam. This creates difficulty in focusing the laser to spot sizes less than $\sim 0.4 \text{ mm}^2$ -which limits the power density available for PLD using these lasers (compared to other types of laser such as Nd:YAG, which can focus down to $10 \text{ }\mu\text{m}^2$ or better).

The ArF excimer laser commonly generates a UV laser pulse at 193 nm with bandwidth of about 1 nm and a duration of 20 ns. The pulse-shape is rectangular in cross-section with dimensions $15 \times 30 \text{ mm}$ determined by the output window of the laser. A schematic diagram of an ArF excimer laser cavity is shown in Figure 3.2.

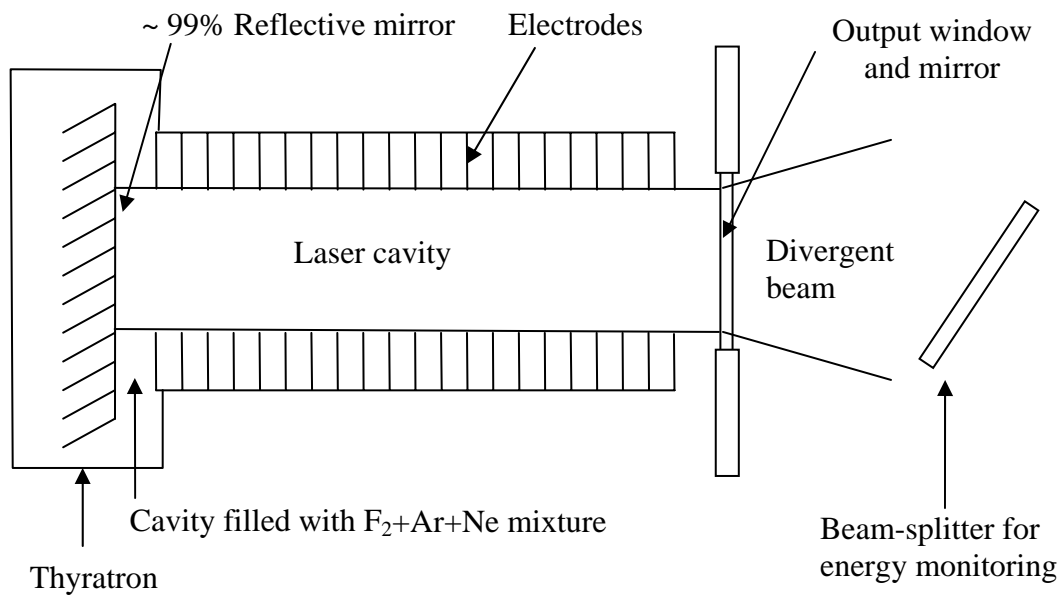


Figure 3.2 Schematic diagram of an ArF excimer laser cavity.

3.2. Pulsed Laser Ablation and Deposition

The PLD technique is an extremely simple technique to produce high quality thin films in a physical vapour deposition system. It involves ablation of a solid target material with a high power laser beam, tightly focused in a high vacuum or low pressure of ambient gas. The extreme photon-energy density at the focus on the target surface causes the ejection of neutral and ionized material via thermal and photochemical ejection mechanisms. The ejected material from the surface of a target is called an “ablation plume”. This ablation plume produces a transient highly luminous plasma in the form of ions, electrons, atoms, radicals or clusters. The process leading to this plume is called *pulsed laser ablation* (PLA). The components of the plume expand rapidly away from the surface of the target material at energies of ~ 100 eV and travel across the vacuum chamber until they impinge on a substrate, upon which deposition takes place. Thus, PLA which results in deposition of material is now termed *pulsed laser deposition* (PLD). At each laser pulse, more material is deposited and the film becomes denser and thicker. The thickness of the films can be from a few atomic layers to many μm [105].

3.2.1. Characteristics of the PLD Process [106]

3.2.1.1. Stoichiometric Transfer

Films that are formed by PLD techniques often have the same composition as the target because the high initial rate of heating of the target, the high efficient atomic excitation and electronic ionization, and the non-thermal target erosion by the plasma all combine to cause uniform ejection of the surface material. However, often stoichiometry is not preserved when one component of the target has a significantly different volatility compared to the others, *i.e.* it will evaporate faster or slower than the rest of the target. This is readily overcome, however, by adjusting the stoichiometry of the target to be richer or poorer in the required component (see Section 6.4.3 SIMS results).

3.2.1.2. The Energetics of the Ablation Plasma

Plasma formed in the ablation plume has a high initial velocity about $10^8 \text{ m}\cdot\text{s}^{-1}$, and in the absence of any background gas (*i.e.* in a vacuum) this velocity will be maintained until it strikes the substrate. If a background gas is present, collisions will slow the velocity of the plume components with increasing of distance from the target.

3.2.1.3. Multi-Layered Films

Films grown by PLD can be grown on a substrate a single atomic layer at a time, or multiple layers, by changing the deposition conditions. Multi-layered films, therefore, can be grown by sequential deposition with different target compositions, *e.g.* for superconductors, electronic devices or quantum well structures [107].

3.2.1.4. Uniform Thickness Over a Controlled Area

The plume generally generated by PLA travels perpendicularly to the target normal, but has a small degree of lateral spread. Thus the ablation plume material forms a cone of material within which the concentration of material is roughly uniform. If a substrate is placed close to the target (*i.e.* near the base of the cone), only a small area can be coated, but the resulting film thickness will be high. However, if the substrate is placed further away a larger area can be coated but the decreased density in the expanding plume leads to a thinner film. Thus, choice of target-to-substrate distance is a crucial parameter in PLD since it governs both the area and the film thickness, as shown in Figure 3.3.

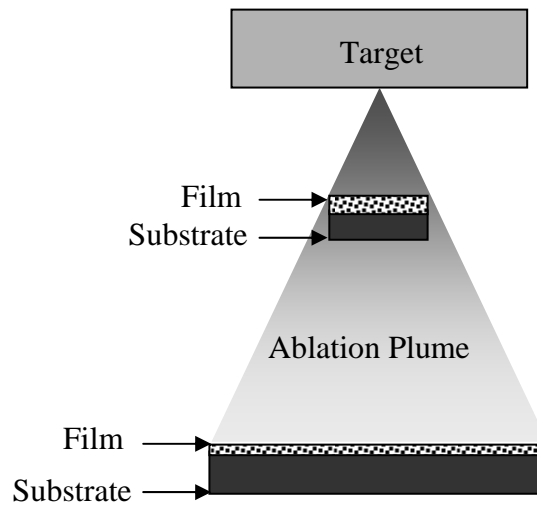


Figure 3.3 Film thickness and deposited area depend on the distance away from target.

3.2.2. The Stages of PLA

When the laser is focused onto the target material, ablation occurs, and this can be separated into four stages occurring at different times during the laser-target interaction, as shown in Figure 3.4.

- A. Surface heating of the target by the laser.
- B. Surface melting and thermionic emission of electrons.
- C. Interaction of the laser with ablated species, and production of plasma.
- D. Absorption of the laser radiation by the plasma.

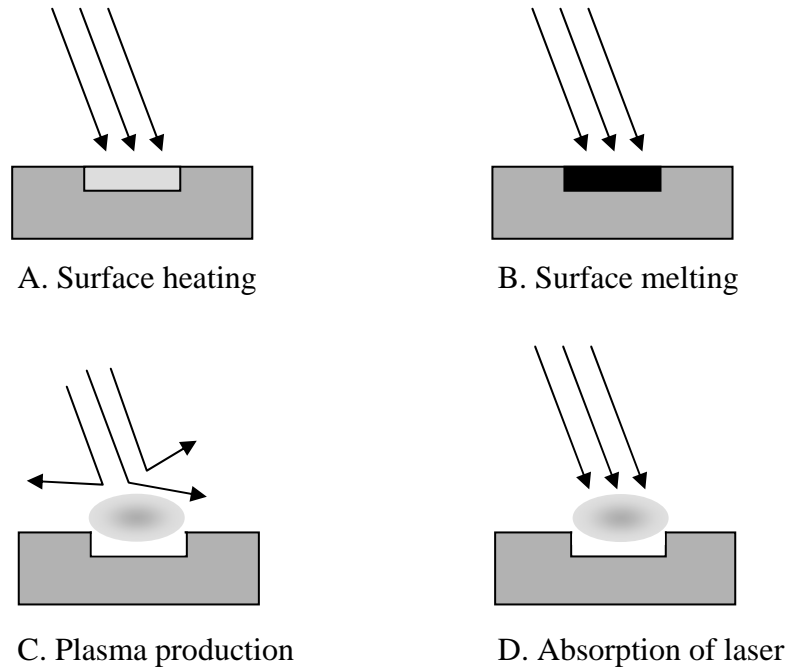


Figure 3.4 Four main stages of PLA.

3.2.2.1. Surface Heating

The first stage of PLA is the heating of the surface by the laser, which depends on the absorption of the laser power by the surface, which usually decreases with increasing wavelength. This can be seen by considering the 1-dimensional heat-flow equation in Equation 3.8 [108].

$$c\rho \frac{\partial T}{\partial t} = I(Z, t)\alpha + \frac{\partial}{\partial z} \left(\kappa(T) \frac{\partial T}{\partial z} \right), \quad (3.8)$$

where c is the heat capacity, ρ is the density of the target, κ is the conductivity of the material, and I is the laser intensity which is a function of position, Z and time, t . α is the absorption coefficient, given by:

$$\alpha = \frac{4\pi k}{\lambda}, \quad (3.9)$$

where k is the extinction coefficient and λ is the wavelength in nm.

When the laser is focused onto the target, a temperature profile is set up from the surface down into the bulk. The depth of the heating depends on the wavelength, because the penetration of longer wavelengths is deeper than the penetration of shorter wavelengths. For short wavelengths, *e.g.* UV, only the top few layers absorb the laser energy and so these are vaporised instantaneously, typically as atomic or small molecular species or ions. Longer wavelengths, however, penetrate many layers below the surface, and deposit the energy there. This causes these sub-surface layers to vaporise causing fragments from the top layers to be ejected from surface as unbroken lumps. These fragments may be deposited as unwanted particulates in the film.

3.2.2.2. Surface Melting and Thermionic Emission

After the surface is heated, the surface vaporises instantaneously due to the high power density. This can be seen by considering the basic relationship in electromagnetism, as is shown in Equation 3.10 [108].

$$E = \left(\frac{2\Phi}{c\epsilon_0 n} \right)^{1/2}, \quad (3.10)$$

where E is the electric field (V/cm), Φ is the power density of the laser (W/cm^2), ϵ_0 is the dielectric constant in vacuum (8.854×10^{-12} F/m), n is the refractive index of the material, and c is the velocity of light (3×10^8 m/s).

For the target in question, the refractive index of graphite at 193 nm is 1.05. For a laser power of $\sim 10^9$ W/cm^2 , the electric field inside the material, therefore, will be 8.5 V/cm, which is enough to break down the dielectric, resulting in thermionic emission of fast electrons, followed by ions and neutrals. In other words, for a high enough laser power density the evaporated material will be in the form of plasma.

3.2.2.3. Enhancing the Production of a Plasma

Throughout the duration of the laser pulse (20 ns) the laser will also interact with the thermally ejected ions, atoms and molecules in the plume. The wavelength of the laser (usually in the UV range) will cause fragmentation of some of the ejected clusters, and also ionisation of neutrals by non-resonant multiphoton ionisation. Since the ions are contained in a small volume, their electrostatic repulsion is large, causing them to accelerate and expand in a so-called ‘Coulombic explosion’. This expansion is also helped by the attraction from the fast electrons that were ejected ahead of the plume. Further, the target will be heated by the recoil pressure of the plume.

3.2.2.4. Absorption of the Laser Radiation by the Plasma

After production of the plasma, the highly charged plume becomes quite opaque at the laser wavelength, so it absorbs all the laser energy by inelastic free-electron scattering (inverse *Bremsstrahlung*), so becoming hotter and even more ionised. The surface of the target, therefore, is now shielded from the laser. But, thermal evaporation continues and large clusters are not broken down by ionisation and photolysis by the laser.

3.2.3. Effects of Process Parameters

PLD offers many process parameters which can be varied to obtain films with desired properties. These include: laser wavelength, laser fluence, ambient gas, substrate temperature and target-substrate distance [62].

3.2.3.1. Laser Wavelength

Of all of the PLD parameters, the laser wavelength is the most influential due to the wavelength dependence of absorption, as discussed in Section 3.2.2.1. Long wavelengths interact thermally with many substrates leading to a slow, deep heating and subsequent problems such as particulate formation and low plume energy, while short wavelengths couple to electrons, causing a more rapid and explosive heating. Consequently, larger target areas (and hence faster deposition rates) can be ablated at the shorter wavelengths without problems arising from particulates.

Another important effect is that of the UV-photon interaction with the plume after ablation. This photon energy is high enough to ionise most species present in the plume with the result that the reactivity in the presence of a background gas is improved (Section 3.2.3.3).

Wavelength / nm	Predominant ions	Mean kinetic energy / eV
1064	C_{11}^+	3.3
	C_{15}^+	4.5
532	C_2^+	38
	C_3^+	17
248	C_2^+	55
	C_3^+	18

Table 3.2 Mean kinetic energy of ionised carbon species produced by different wavelengths during PLA of graphite [109].

Murray and Peeler [109] measured the predominant carbon ions arising from PLA of graphite using different laser wavelengths. They found that the size of the predominant ion clusters decreased and the velocity of the ions increased with decreasing laser wavelength (see Table 3.2). For this reason, most PLD from graphite uses UV lasers.

3.2.3.2. Laser Fluence

The laser fluence is another parameter which has a significant effect on the particulate size and density. It is defined as the energy per unit area arriving at the target, and can be varied by varying the laser spot-size and the laser power. The spot-size depends upon the laser focusing position, as well as the laser type (see Section 3.2.2). The focusing and spot-size control the angular distribution of the ablated material, because a smaller spot-size produces a more directional plume. For the same power, a lower spot-size corresponds to a higher laser fluence. At constant laser power, the particulate number density is usually higher with a tighter focus. A higher power laser will cause more ionization of the ablated material, increased fragmentation of large clusters, and more thermal evaporation from the surface away from the laser focus. This produces a greater particulate number density. However, the rate of increase of particulate number density eventually reduces at very high fluence, and saturates to a constant value [110], see Figure 3.5.

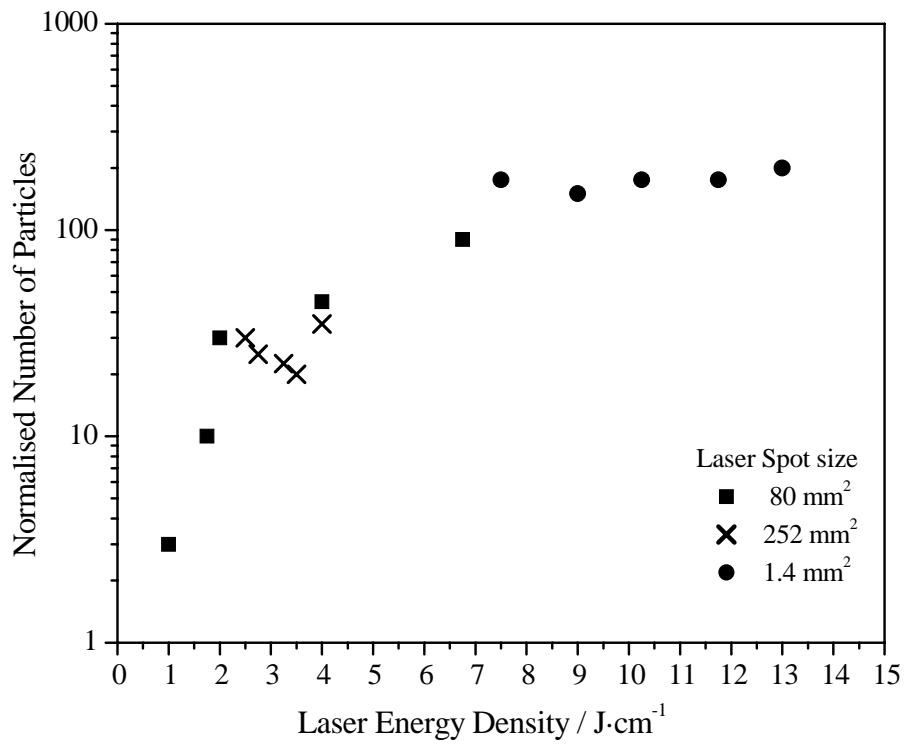


Figure 3.5 Number of particulates corrected for the film thickness as a function of laser fluence [110].

3.2.3.3. Background Gas

PLD is often performed in vacuum; however, it is possible to perform PLD with the target and substrate in a low pressure of background gas. This gas can be inert (N_2 , Ar) or reactive (NH_3), and its presence is one of the features that make PLD so versatile. The gas molecules can serve to thermalise the plume, and thereby reduce the kinetic and impact energy of the particles on the growing film. This can affect the bonding within the film, as well as change its hardness and density. Moreover, the presence of an inert ambient gas can help the formation of clusters, nanoparticles, and the creation of a shock-front in the gas mixture which may aid deposition of multicomponent materials [111, 112]. Furthermore, collisions between the atoms in the ablation plume and those from the background gas can result in chemical reactions, leading to films being deposited which contain atoms from both sources.

3.2.3.4. Target-to-Substrate Distance

The plume of ejected target material is generally symmetric and perpendicular to the surface of the target, and it does not depend upon the direction of the impinging laser beam or its angular divergence [113]. This means that the uniformity of the film over a given area can be achieved by simply varying the distance between the target and substrate, as explained in Section 3.2.1.4.

3.2.3.5. Substrate Temperature

Various properties of the deposited film depend upon the substrate temperature. Low substrate temperatures are not advantageous for the deposition of crystalline films. Crystal formation is improved at higher temperature when the species are mobile on the surface of the film allowing them to move to a more energetically favourable position. However, if the substrate temperature becomes too high, there may be the problem of re-evaporation of the more volatile components, leading to film thinning and a change of stoichiometry.

3.2.4. Particulates

PLD techniques have the same problem as sputtering techniques—unwanted large particles may be produced which are deposited onto the film surface and adversely affect uniformity. These particulates are formed from large aggregations of target material on scale of 0.1 to 10 μm with most smaller than 1 μm . This problem is intrinsic in the PLD process, and holds back its use in many electronic and optical applications which require extreme surface smoothness.

There are four main mechanisms proposed for the formation of particulates in PLD techniques, which mainly depend on the laser fluence and the target composition.

1. Surface features of the target, such as cracks and protrusions, are either formed by the action of prior ablation or are inherent to the target or. These are then dislodged due to thermal and mechanical shock or by the action of the ablation.
2. Evaporation of the sub-surface material causes the fracturing and ejection of the target surface. This is more of a problem when using longer laser wavelengths.
3. Gas within the bulk of the target that was trapped during target fabrication, becomes heated and expands, so fracturing and ejecting the target surface.
4. Condensation from the plume due to supersaturation. This probably occurs with high ambient gas pressure.

In this dissertation, the target is formed from compressed graphite and sulphur powder, and will have cracks, protrusions and trapped gas. These will be the main causes of particulates. Particulates from splashing of the molten target and condensation from the plume are unlikely to be a problem because the deposition conditions are insufficiently powerful to liquefy graphite, and there is no ambient gas pressure.

3.2.4.1. Elimination of Particulates

3.2.4.1.1. Laser Effects

In Section 3.2.3.1, the laser wavelength was shown to have an effect on the number of particulates due to the wavelength dependence of the absorption coefficient of the target material. Longer wavelengths normally couple thermally to the target, causing surface melting and deep heating. The recoil action of the expanding plume and the continued heating will cause the molten layer to ‘splash’. Short wavelengths normally couple to electrons, causing shallower and more rapid heating. The higher photon energy will ionise and fragment any particulates that may form.

The laser fluence also has an effect on the number of particulates. The reduction the laser power to below the level that causes splashing is the simplest method for the elimination of particulates. However, another effect of laser power reduction is the reduced energy of the ablated species, and possibly a reduction in the quality and deposition rate of the films.

3.2.4.1.2. Plume Effects

Atomic-sized species in the plume will travel orders of magnitude faster than larger and heavier particulates. The particulates, therefore, can be removed mechanically from the plume by manipulation of the plume, either with an off-axis arrangement for the deposition or by steering the charged plume with electric or magnetic fields. A type of mechanical filter that is used for the elimination of particulates is the spinning vane filter, as shown in Figure 3.6.

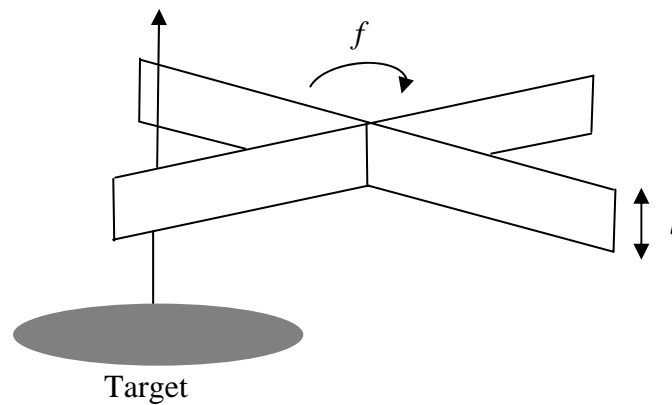


Figure 3.6 Schematic diagram of a velocity filter for elimination of slow-moving particulates from a fast plume [114].

All particles travelling with velocity (v) greater than a cut-off velocity (V_c) will pass through the vane filter, so long as they arrive within a time of $\frac{1}{V_c} - \frac{1}{v}$ of a vane passing at their entry point. The cut-off velocity of the spinning vane filter is given by:

$$V_c = nfl, \quad (3.11)$$

where n is the number of vanes, f is the speed of rotation, and l is the length of each vane. However, such mechanical vanes are tricky to implement within a vacuum system, and suffer from frequent clogging and breakdown due to the harsh conditions near the ablation plume.

3.2.4.1.3. Geometry

When using a background gas the plume undergoes collisions with the gas molecules, and scatters so that it is no longer highly directional. Heavy particles will scatter less and mostly remain on their initial trajectories.

However, the lighter species will scatter in all directions. If a substrate is placed off-axis from the initial plume trajectory the heavier particulates will pass it by whilst the scattered smaller atoms and ions will still strike it (see Figure 3.7). This will decrease the particulate density in the film at the expense of a much reduced deposition rate and a lower deposition energy, which may affect film properties such as hardness or density.

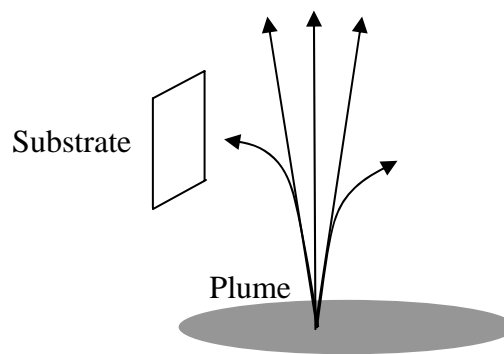


Figure 3.7 Off-axis PLD geometry to produce reduced-particulate films [114].

3.3. Diamond-Like Carbon Films Produced by PLD

The preparation of DLC thin films by PLD has received much attention in recent years because this technique produces hard-carbon films which do not contain hydrogen, with high sp^3/sp^2 ratios [4, 33, 62]. Several reports have reported deposition of DLC films by PLD, as summarised in Table 3.3.

PLD is commonly believed to be an energetic process. Consequently, the laser wavelength or photon energy has been a crucial parameter for producing the high degree of diamond-like properties found in PLD carbon films [4, 30, 33, 62]. In Table 3.3, changing the laser wavelength from IR to UV is seen to result in an increase in the diamond-like properties of the films. Particularly, a UV ArF laser, with the lowest wavelength, was found to obtain DLC films containing 95% sp^3 carbon.

Laser type	Power density / (W/cm ²)	Results	Reference
Nd: YAG (532 nm)	5×10^{11}	$E_g = 1.0$ eV, 75% sp ³	[115]
XeCl (308 nm)	3×10^8	Hard, $E_g = 1.4$ eV	[116]
XeCl (308 nm)	1.25×10^8	$E_g = 1.27$ eV	[117]
KrF (248 nm)	1.4×10^8	$E_g = 1.7$ eV, 85% sp ³	[38]
ArF (193 nm)	5×10^8	$E_g = 2.6$ eV, 95% sp ³	[4]

Table 3.3 Summary of the reported results for DLC films deposited by PLD. E_g is the energy band gap and the percentage values correspond to the amount of sp³ carbon in the film.

The laser power density is another parameter used to produce a high degree of diamond-like properties. This depends on the laser energy and beam diameter focused on the target [36]. Laser power densities in range of 10^8 - 10^{11} W/cm² are most commonly achieved [4]. Past experiments have indicated that the sp³ ratio increased as a function of increasing laser power density. This is because the ionisation of carbon particles with moderately high kinetic energies (from several eV up to ~100 eV) is a function of laser power density. Conversely, the formation of sp³ bonding structure is destroyed under excessively high energy ion bombardment (>200 eV), therefore, DLC films convert to the more stable sp² graphite structure. A threshold power laser density of $\sim 10^{11}$ W/cm² is reported in order to grow high quality DLC films [4].

CHAPTER IV

EXPERIMENTAL SETUP

4.1. Pulsed Laser Deposition

The PLD system used to grow DLC and S-DLC films consists of an ArF excimer laser, vacuum ablation system, target material, substrate and CO₂ laser. A schematic diagram and photograph of PLD system are shown in Figures 4.1 and 4.2, respectively.

Overview of PLD system: the deposition chamber was evacuated by a rotary and a turbomolecular pump, yielding a typical background pressure of 1×10^{-6} Torr. The output of an ArF excimer laser was focused onto a rotating target, yielding an incident fluence on the target 10 and 20 J/cm². The target-substrate separation was maintained in the range of 40 mm. A continuous wave (CW) CO₂ laser was employed to heat the substrate by illumination on its rear surface. The substrate temperature (T_{sub}) was varied from room temperature, 150 °C and 250 °C by adjustment of the CO₂ laser output power. The experimental parameters used are shown in Table 4.1.

Excimer laser power (ArF, 193 nm)	10 and 20 J/cm ²
Substrate temperature (T_{sub})	RT, 150, 250 °C
Background gas pressure	10^{-6} Torr
Distance between target and substrate	40 mm
Growth time	15 min

Table 4.1 Experimental parameters. RT = room temperature.

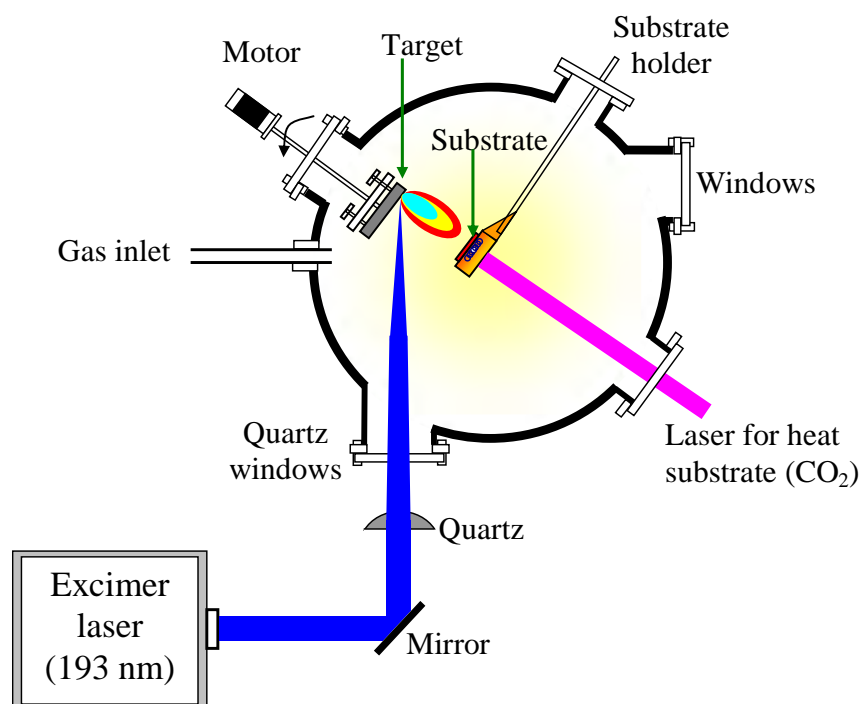


Figure 4.1 Schematic diagram of PLD system.



Figure 4.2 Photograph of PLD system (at School of Chemistry, University of Bristol).

4.1.2. Excimer Laser

The ArF excimer laser system was Lambda-Physik Complex 201 which operated at 193 nm output and 10 Hz repetition rate. The laser gas mixture was 0.16% F₂, 6.3% Ar in a Ne balance. The basic operation of an ArF excimer laser was described in Section 3.1.1. A schematic diagram of the laser set-up is shown in Figure 4.3. The 193 nm laser output was guided into the vacuum chamber by reflecting off two highly reflective mirrors (~98% at 193 nm). The alignment of the laser into the vacuum chamber was realized by adjusting the position of these two mirrors. An iris was used to reduce the laser beam size when low fluence or small focal spot-sizes on the target were required. The beam passed through a 20 cm-focal-length plano-convex lens mounted close to the vacuum ablation chamber, and from there passed through the fused-silica window mounted on the ablation chamber wall. The beam was then focused onto the target material at a typical angle of incidence of $\theta = 45^\circ$ to the surface normal. The plano-convex lens was mounted on a xyz micrometre-driven translation stage. This allowed fine adjustment of the lens position, and thus of the position of the laser beam focus on the target surface.

A computerised keypad controller was employed to control the evacuation and gas filling procedure for the laser. With a fresh fill of gas and clean optical mirrors, pulsed laser outputs with energies of ~300 mJ could be provided at the maximum discharge voltage of 30 kV. The discharge voltage was set up in the range 21-30 kV. The repetition rate of the laser was set up in the range of 1-10 Hz but was usually fixed at 10 Hz. The beam profiles were rectangular (~15×30 mm²) due to the discharge cavity design, and the pulse duration was ~20 ns. The laser power was measured in each experiment because the performance of the laser degraded with time (see Section 3.1.1). It was therefore necessary to increase the voltage to obtain the same laser power a few days after gas refilling. The gas mixture was normally refilled in every two weeks.

The laser power was generated by a voltage applied to a flashlamp inside the ArF excimer laser. It was detected by a photodiode with sensitivity 3.3 V/J, which converted the light into electrical power signals and displayed on the monitor of an oscilloscope. The laser fluence was calculated by division of the laser power by the spot-size on target. A spot-size $1.0 \times 0.4 \text{ mm}^2$ on the target was achieved by measuring the size of the drilled laser hole from SEM images of the target after irradiation, as shown in Figure 4.4.

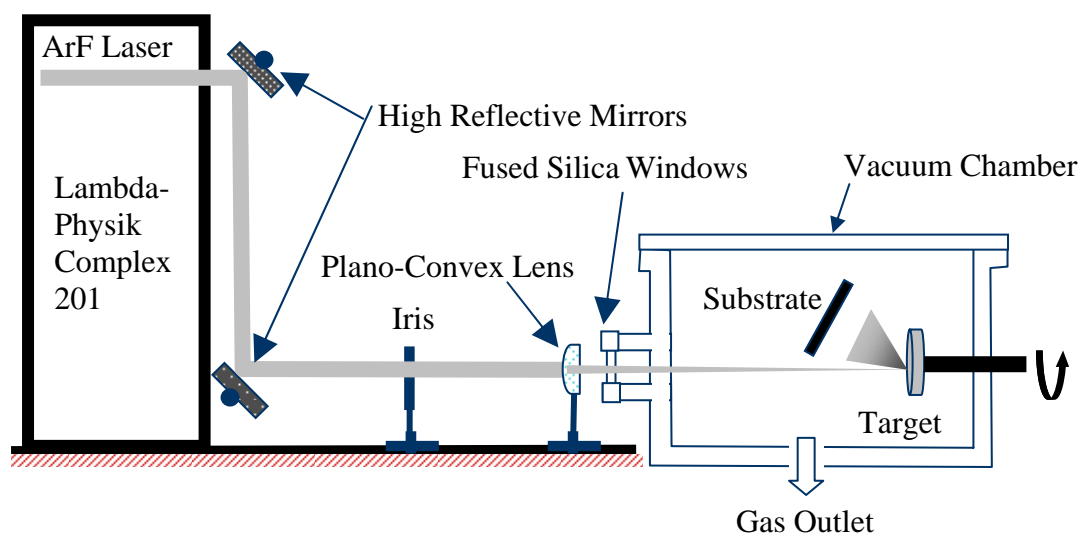


Figure 4.3 Schematic diagram of the laser set-up.

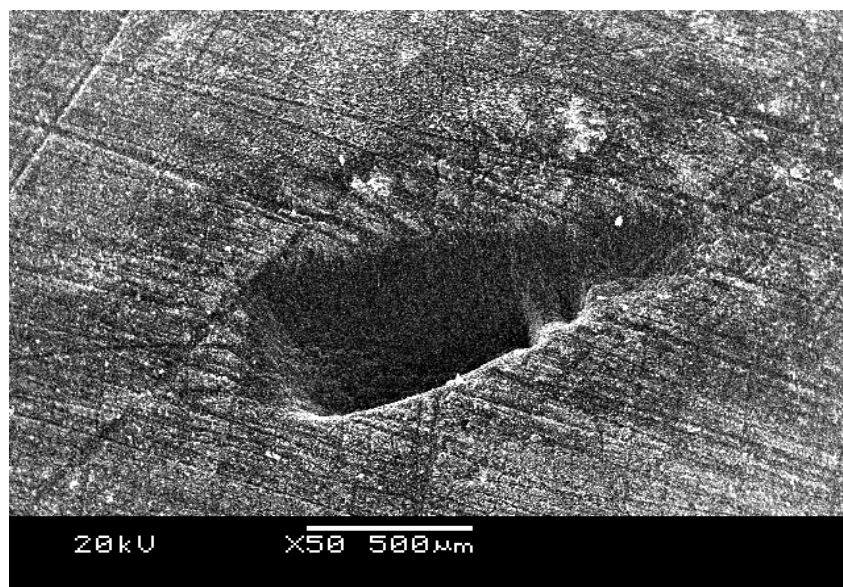


Figure 4.4 SEM image of the laser drilled hole on the target surface.

4.1.3. Vacuum Ablation Chamber

The ablation chamber was made from a stainless steel cylinder with internal diameter of 260 mm and height of 160 mm, and was mounted on top of a 100 mm turbomolecular pump (Leybold Turbotronic NTL59/369) backed by a two-stage rotary pump (Leybold Trivac). There was a fused silica window in the top-plate of the chamber for observation of the ablation process. The base pressure maintained in the ablation chamber was about 10^{-6} Torr. The pumping system was isolated from the ablation chamber via a butterfly valve. The pressure in the chamber was measured by Penning gauges (Edwards) and a Baratron capacitance manometer (MKS) gauge with working pressures in range of 5×10^{-8} to 10 Torr. The top flange was the full diameter of the chamber and was removable for access to the target and substrate. There were a number of flanges around the chamber for manipulation of the target and substrate. These included a thermocouple for monitoring the substrate temperature, gas inlets for bringing the chamber up to atmosphere pressure or for ablation in a background gas, and a mechanical feed-through for rotating the substrate holder and target holder. A quartz window had a dual purpose: it allowed the ArF laser beam into the chamber to strike the target, and it allowed IR light from a second laser (CO_2) to enter the chamber for substrate heating.

The quartz window needed to be changed every 15 min or about 9000 laser shots because after this time the film deposited on this window had become so thick that the window had become opaque, so decreasing the laser fluence reaching the target material. The DLC film deposited on the quartz window was removed by heating in air using a Bunsen flame.

4.1.4. Target Material

The sulphur-graphite target material was made from >99.99% high purity graphite and sulphur powders compressed by a 10-ton press to form a disc 5 cm in diameter and 1 cm thickness, as shown in Figure 4.5. Latex glue was mixed with the powders to act as a binder before the compression, and it was evaporated from the target material by heating to more than 120°C in an oven in air after the compression. The

amount of mixed glue used was about 50 cm^3 per 100 g of powder. Different molar ratios of sulphur and graphite were used: 0%, 1%, 5%, 10% and 25%. After preparation of the target, it was polished flat and smooth with sandpaper. It was then placed into the holder within the vacuum chamber and the focus position on the target was adjusted along the direction parallel to the laser beam.

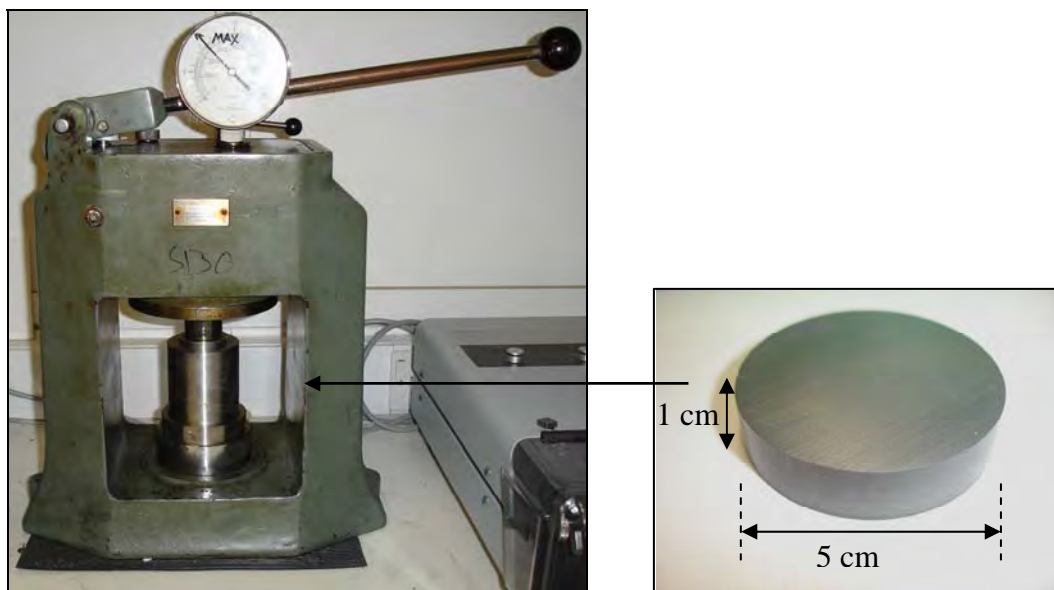


Figure 4.5 Photograph of the 10-ton press and the compressed target material in the form of a 5 cm diameter, 1 cm thick disc (at School of Chemistry, University of Bristol).

The action of ablation made deep pits on the target, so it was necessary to rotate the target to expose a fresh graphite surface at each laser shot. The target, therefore, was clamped in a holder on a shaft that passed through two O-rings to a stepper motor on the outside of the chamber, which was rotated at about 1 rpm. The disadvantage of this is that the surface of the target was not fully used because the track was circular and fresh ablation occurred only in the first rotation. On the next rotation, the laser ablated the same region on the surface target. The target used was changed after 15 min or 9000 shots of the operation and a new target prepared and polished flat.

4.1.5. Substrate and Substrate Heating

The substrates used were quartz wafers and a single crystal (100) boron-doped silicon wafers with 1-100 Ω -cm resistivity of size $\sim 1 \times 1 \text{ cm}^2$. The substrates were cleaned with acetone and ethanol before the deposition. They were clamped to a copper holder on a shaft that passed through on O-ring to a rotatable scale reader outside the chamber. Silver paint on the back of the substrate ensured good thermal contact with the copper plate. For heated substrates another silicon wafer was placed on the other side of the copper sheet, contacted by silver paint as well. This second silicon wafer helped to decrease the reflection of the CO_2 laser during substrate heating and to uniformly distribute the heat on the substrate. The temperature of the substrate was monitored by a thermocouple attached to the substrate surface. A schematic diagram of an unheated substrate and heated substrate is shown in Figure 4.6.

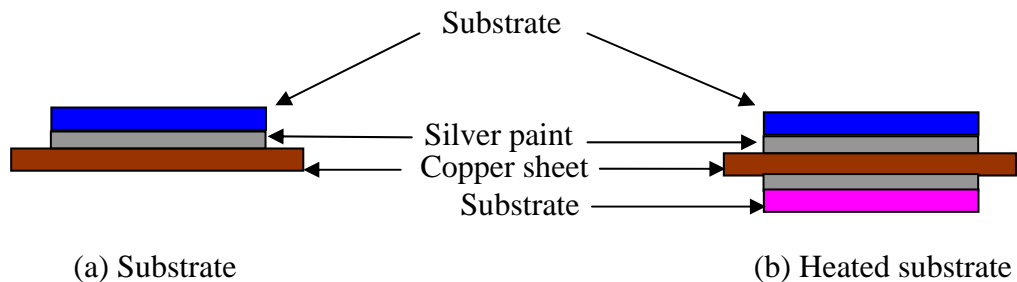


Figure 4.6 Schematic diagrams of (a) substrate and (b) heated substrate.

4.1.6. Carbon Dioxide Laser (CO_2 Laser)

A continuous wave (CW) $10.6 \mu\text{m}$ CO_2 laser (Synrad model: J48-2W-3180) was employed to produce a beam infrared light to heat and control the temperature on the substrate. It consisted of the RF CO_2 laser power supply and laser controller for controlling the CO_2 laser power by adjusting the % of pulse width modulation (PWM). The laser beam passed through the quartz window mounted on the chamber wall and defocused to a spot-size of $\sim 1 \text{ cm}^2$ to illuminate and therefore heat the backside of the substrate.

CHAPTER V

CHARACTERISATION TECHNIQUES

This chapter contains all characterisation techniques employed in this dissertation. All DLC and S-DLC films have been analyzed using several techniques. Laser Raman Spectroscopy was used to identify the structural properties of films. Spectroscopic Ellipsometry and Ultraviolet-Visible Spectroscopy was used to identify the optical properties, while Linear Four-Point Probe and Hall Effect measurements have been used to study the electrical properties of films. Scanning Electron Microscopy was used to image the film morphology. Secondary Ion Mass Spectroscopy and Energy Dispersive X-ray Spectroscopy have been used to identify the compositional properties, and Nanoindentation was used to identify the hardness of films.

5.1. Laser Raman Spectroscopy (LRS)

5.1.1. Introduction

LRS is a spectroscopic technique used to study vibrational and rotational modes of motion in condensed matter physics and chemistry. It is a very useful non-destructive tool to identify chemical bonding and structure of materials. All films were analyzed by LRS prior to other analysis.

5.1.2. Theory

When a beam of intense monochromatic light is incident on a material, most of the photons are scattered at the same wavelength as the incident radiation (Rayleigh radiation). But some of the photons interact with the molecules in the material and either gain or lose energy. The photons which are scattered with lower energy arise because some energy is lost in the material in the form of molecular vibrations in

single molecules or lattice phonons in crystalline solids. The coupling of the incident radiation to the phonon band of the material makes this technique very sensitive to bonding structure and symmetry disorder (bond-angle disorder) in materials such as diamond. The photons that scattered with less energy than the original are called “Stokes radiation”. In the case that the photons interact with an already excited molecule, it may increase its energy upon scattering, as it can gain energy from the material. These scattered photons are called “anti-Stokes radiation”. These scattered photons usually have low intensity. In this case a highly monochromatic and intense incident laser beam is needed.

LRS is the measurement of the inelastic scattering of photons (Stokes radiation) due to the change of polarization caused by the phonon mode, usually in a backscattering geometry. Since the original laser wavelength is known the energy difference can be calculated. The energy levels of molecule/materials can be probed by monitoring the frequency of the scattered radiation [53]. A schematic diagram and photograph of a LRS system are shown in Figures 5.1 and 5.2, respectively.

The laser light enters into the spectrometer and passed through a plasma filter to remove unwanted ‘plasma’ lines from the laser. The beam is then expanded and then is reflected off a semitransparent mirror into the microscope. This focuses the light onto the specimen with a spot-size resolution of $\sim 1 \mu\text{m}$ diameter. The scattered radiation returns to the spectrometer by the backward path, with the laser line being blocked by a suitable notch filter. The remaining light passes through the notch filter, then through the semitransparent mirror and is dispersed using a movable diffraction grating and captured by a CCD array. The spectrum can be recorded either with a fixed grating angle spreading a fixed number of wavelengths of light across the CCD array, or by rotating the grating to bring different wavelengths to bear on the detector sequentially.

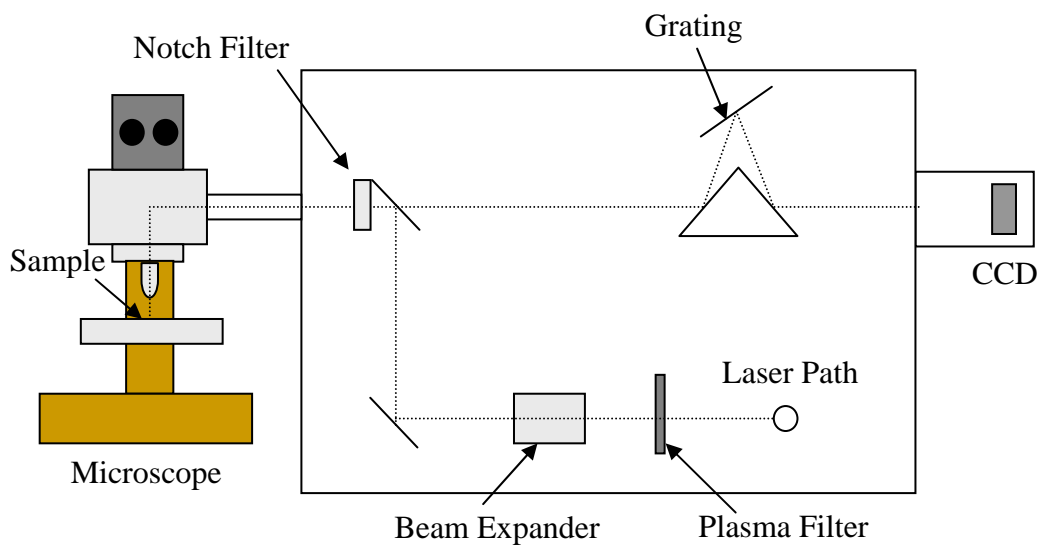


Figure 5.1 Schematic diagram of the LRS microscope.



Figure 5.2 Photograph of the Renishaw 2000 LRS microscope (at School of Chemistry, University of Bristol).

Three lasers were available for use with the spectrometer, with output wavelengths of 325 nm, 514 nm and 785 nm, which correspond to the wavelengths of He-Cd, Ar⁺ and IR-diode lasers, respectively. The Raman laser used almost exclusively for DLC film analysis was the green Ar⁺ laser at a wavelength 514 nm. This is quite low in energy, so cannot excite σ states in the sample, but it can excite π states due to these being lower in energy. π states have more easily polarized sp^2 hybridized carbons than sp^3 hybridized carbons by a factor of ~ 50 -230 times. Consequently, sp^2 hybridized carbon totally dominate the visible Raman spectrum [53]. Other smaller peaks can appear in the spectrum due to the presence in the film of other carbon structures, such as sp or sp^3 -bonded C and CH groups.

There is a resonant enhancement of two vibrational modes of DLC in a Raman spectrum, at around 1360 cm^{-1} and 1580 cm^{-1} , which are called the D and G peaks, respectively. The D peak is often a low frequency shoulder on the G peak and so its position is usually less accurately measured.

The G peak is attributed to the first-order scattering from zone-centre phonons of E_{2g_2} symmetry mode in single-crystal graphite. The G mode arises from the relative motion of sp^2 hybridized carbon, *i.e.* C=C sp^2 stretch vibrations of olefinic or conjugated carbon chains. This is shown in Figure 5.3(a). The D peak is attributed to the disorder-activated A_{1g} breathing motion of six-fold aromatic rings. The D mode is forbidden in perfect graphite, as is shown in Figure 5.3(b).

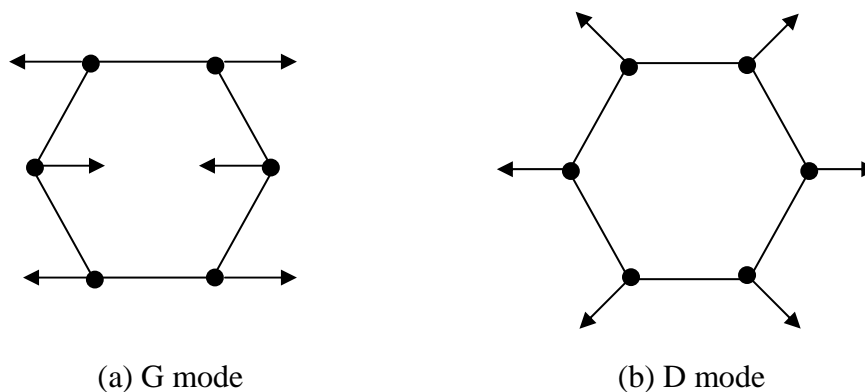


Figure 5.3 Carbon motion in the (a) G mode and (b) D mode [53].

5.1.3. Spectrum Fitting

Since the D and G peaks are often convoluted together, a fitting function must be used to separate them to find out their intensities and positions. Gaussian distributions are used for fitting after subtracting a quadratic polynomial background, which is attributable to fluorescence. For simple spectra two Gaussian components are used sufficient for fitting the G and D peak in DLC films. The deconvolution of the Raman spectrum with two Gaussians in a DLC film is shown in Figure 5.4.

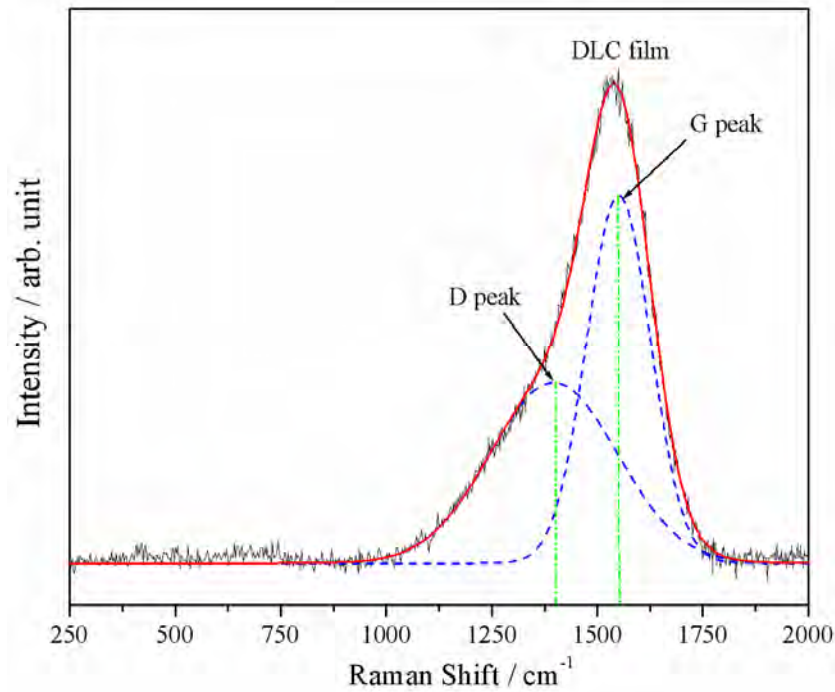


Figure 5.4 Deconvolution of the Raman spectrum with two Gaussians in DLC film.

5.1.4. Graphitization and the I_D/I_G Ratio

The ratio of intensities for D and G peak (I_D/I_G ratio) of amorphous carbon (a-C) and pure crystalline graphite (c-G) is dependent on the size of graphite cluster (L_a), as shown in Figure 5.5.

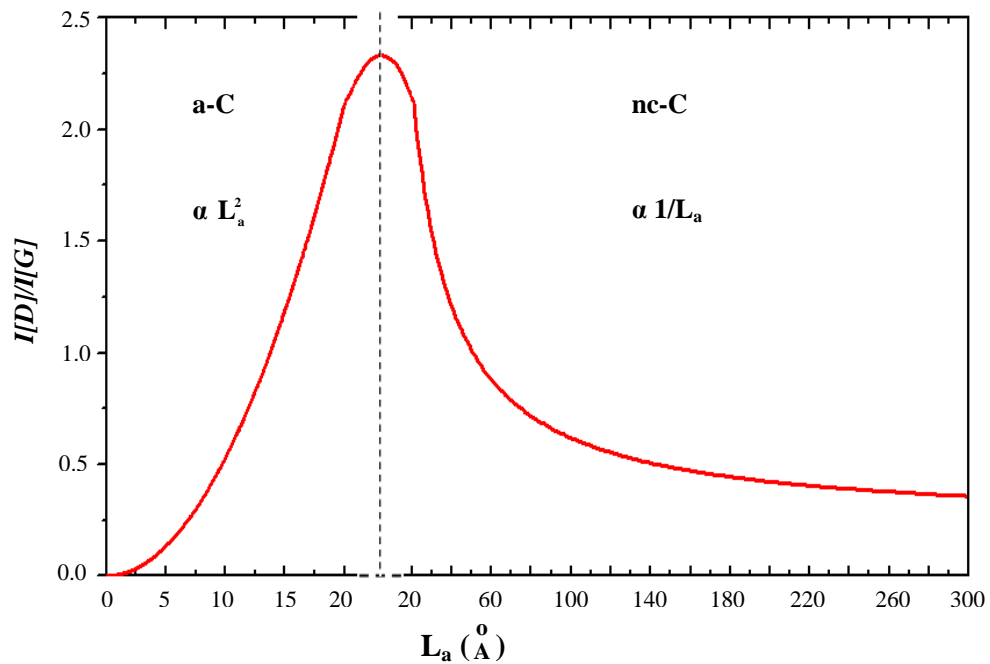


Figure 5.5 Variation of I_D/I_G ratio with L_a [53].

5.1.5. Factors Affecting the Spectrum

Ferrari's latest model [53] considers that the Raman spectrum of a DLC film depend upon 3 factors;

- The clustering of the sp^2 phase.
- The presence of sp^2 rings or chains.
- The sp^2/sp^3 ratio.

The position, widths and relative intensities of the D and G peak are found to vary systematically with deposition condition and film properties. The Raman spectra of a DLC film act on both the D and G peaks, as shown in Figure 5.6.

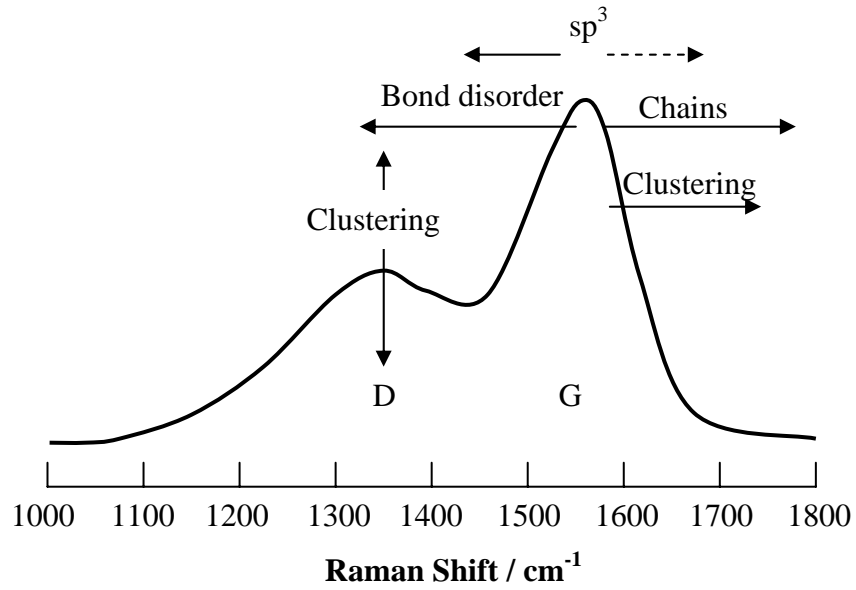


Figure 5.6 Schematic diagram showing the position and heights of D and G peak of DLC films in a Raman spectrum [53].

5.1.6. Characterisation of DLC Films by LRS

In disordered DLC films, the Raman spectra closely resemble the vibration density of states (VDOS), so it can be used to obtain information on defects, structural bonding variation, compositional (sp^3 , sp^2) variation, and the presence of microcrystalline or nanocrystalline grains/clusters. This allows it to be used to predict the E_g , density and hardness of DLC films. Moreover, the G peak position relative to G position in graphite gives an indication of the size of the graphite cluster, which has an effect on the E_g [53].

$$E_g \propto \frac{1}{L_a}, \quad (5.1)$$

where L_a is the graphite cluster size.

$$\frac{I_D}{I_G} = C'(\lambda) L_a^2, \quad (5.2)$$

where $C'(\lambda)$ is the Raman coupling coefficient at incident wavelength λ and I_D/I_G is the ratio of the intensities of the D and G peaks.

The meaning of relation of I_D/I_G and E_g can be seen from the combination of Equations 5.1 and 5.2. When a D peak is present, a decrease in the band gap will always be indicated by an increase in I_D/I_G . In hydrogenated DLC films, the G peak decreases with increasing sp^3 content due to the hydrogen atoms bonded in the films [53]. For S-DLC films it was found that the intensities of the D peak increased, suggesting the presence of sulphur increased the aromatic six-membered ring clustering in the film. This was reflected in a decrease in the optical band gap [24].

5.1.7. LRS Setup

LRS is performed by using a Renishaw 2000 spectrometer, with an Ar^+ laser (green laser) at 514.5 nm on 10% power (to prevent burning or damage to the DLC films). The spectra were scanned between 50 and 2000 cm^{-1} . The D and G peak were fitted using GRAM/32 software, as Gaussian lineshapes on a quadratic baseline. The positions and intensities of D and G peaks were recorded from the curve fitting. The detail of the LRS setup is shown in Table 5.1.

Device	Renishaw 2000
Microscope	Leica DMLM
Laser	Spectrophysics 514 nm (green laser) 20 mW
Objective	×50
Slit diameter	50 μm
Diffraction grating	1200 lines per nm
Scan time	10 s
Scan extension	50-2000 cm^{-1}
Scan accumulation	1

Table 5.1 LRS setup conditions for measurement of the DLC films.

5.2. Spectroscopic Ellipsometry (SE)

5.2.1. Introduction

SE is a popular technique for measure the film thickness, the surface roughness, and the optical properties of films because it is non-destructive and accurate.

5.2.2. Theory

The principle of this technique is measurement and interpretation of the changes in the polarization state of polarized light undergoing oblique reflection from a sample surface. It is based on Fresnel reflection and Maxwell's equations for polarized light encountering boundaries in a planar multi-layered material [118]. For a plane wave reaching a sample, the ratio of the complex Fresnel reflection coefficients for the light polarized parallel (p) to those of the light polarized perpendicular (s) to the plane of the incident wave, illustrated in Figure 5.7, is given by

$$\rho = \frac{r_p}{r_s} = \tan\varphi \cdot \exp(i\Delta), \quad (5.3)$$

where r_p and r_s are the complex Fresnel reflection coefficients of the sample in the plane of incidence and perpendicular to the plane of incidence wave, respectively. The value of $\tan\varphi$ is the amplitude ratio of reflectance and the value of Δ is the phase difference.

SE measurements are normally expressed in term of psi (φ) and delta (Δ). These coefficients are related to the material optical properties and physical dimensions. A photograph of SE apparatus is shown in Figure 5.8.

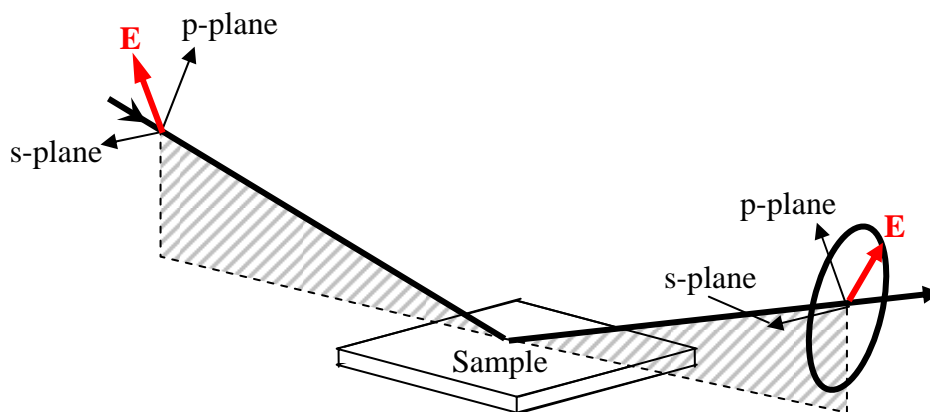


Figure 5.7 Geometry of SE measurements.

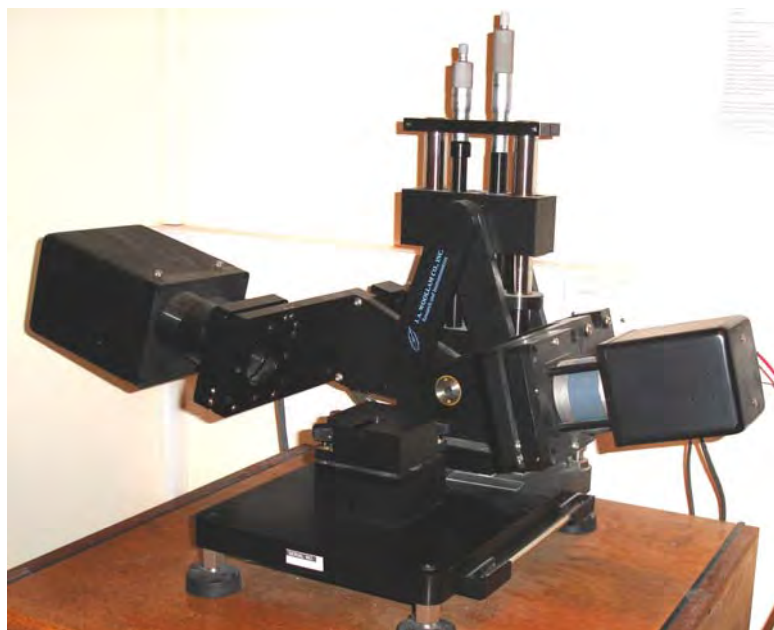


Figure 5.8 Photograph of J.A. Woollam M-2000U SE (at School of Chemistry, University of Bristol).

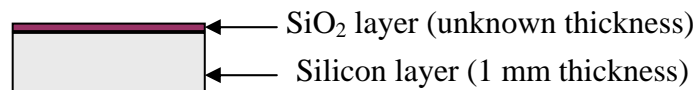
5.2.3. Fitting Model

The data from SE cannot be used directly but must be fitted with an appropriate model using software supplied with the Spectroscopic Ellipsometry. In the process of model fitting, the film thicknesses must be defined first. While the known thickness of some layers that are can be used directly, the unknown thickness of

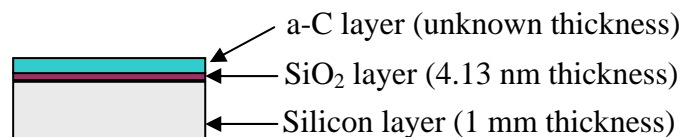
other layers and the optical properties will be obtained after fitting. For an amorphous material such as DLC, the Touc-Lorentz (TL) model is the best model to determine films properties.

There are two fitting models used in this dissertation. The first model was used to find the thickness of the native silicon dioxide layer that was always present on the silicon substrate before film deposition. This was done by considering the fitting as two layers. The first layer was set as the silicon layer with thickness 1 mm, and second layer was set to be the layer of the silicon dioxide with unknown thickness.

The second model was used to find the thickness and the optical properties of deposited DLC films. This model had three layers that need to be set in model fitting. The first layer is still the silicon layer with thickness 1 mm, and the second layer is the thickness of silicon dioxide layer with thickness 4.13 nm (obtained from the measurements and fitting before DLC deposition). This is the result from Section 6.3.2. The last layer is the amorphous carbon layer, as this layer is set as a function of the TL model. The schematic diagram of model fitting is shown in Figure 5.9.



(a) Silicon dioxide layer



(b) Film layer

Figure 5.9 Model fitting of (a) silicon dioxide layer (b) film layer, using results of (a) for the SiO₂ layer.

5.2.4. SE Setup

SE was performed by using a J.A. Woollam Co., Inc. M-2000U Spectroscopic Ellipsometry over the range of 200-1000 nm at angles of 55, 60, 65, 70 and 75°. Analysis was performed using WVASE 32 software. The thickness, refractive index, extinction coefficient and energy band gap were obtained from fitting first the oxide layer and then the DLC layer using the two models described above.

5.3. Ultraviolet-Visible Spectroscopy (UV-VIS)

5.3.1. Introduction

UV-VIS spectroscopy is the measurement of the absorption and transmission of light in the UV and visible regions of the electromagnetic spectrum by probing the outer electronic transitions of the materials composing a thin film. The advantage of using UV-VIS spectroscopy is the ability to obtain an estimate of the optical band gap in a non-destructive fashion.

5.3.2. Theory

Light in the visible and near-ultraviolet passes through the film to be analysed, and some of the light is absorbed by the film. The film, therefore, should be thin enough such that some of the light is transmitted. The film normally should be placed on a supporting substrate, for example, quartz, which is transparent at visible or ultraviolet wavelengths of light. The intensity of light, I , passing through a sample of thickness, x , and the incident light intensity, I_0 , is measured. The ratio I/I_0 is called the transmittance and is usually expressed as a percentage, % T . The absorption coefficient, α , is based on the transmittance and appears in the Beer-Lambert law, as shown in Equation 5.4.

$$I = I_0 \exp(-\alpha x). \quad (5.4)$$

The band gap is defined as the minimum energy between the occupied valence band and empty conduction band, and can obtain by using the Tauc relationship from calculation of the energy dependence of the optical absorption coefficient, as shown in Equation 5.5.

$$(\alpha h\nu)^{1/2} = B(h\nu - E_g), \quad (5.5)$$

where α is the absorption coefficient, $h\nu$ is the energy of the radiation, B is the Tauc gap constant and E_g is the optical band gap (or Tauc gap).

A schematic diagram and photograph of the UV-VIS spectroscopic apparatus are shown in Figures 5.10 and 5.11, respectively.

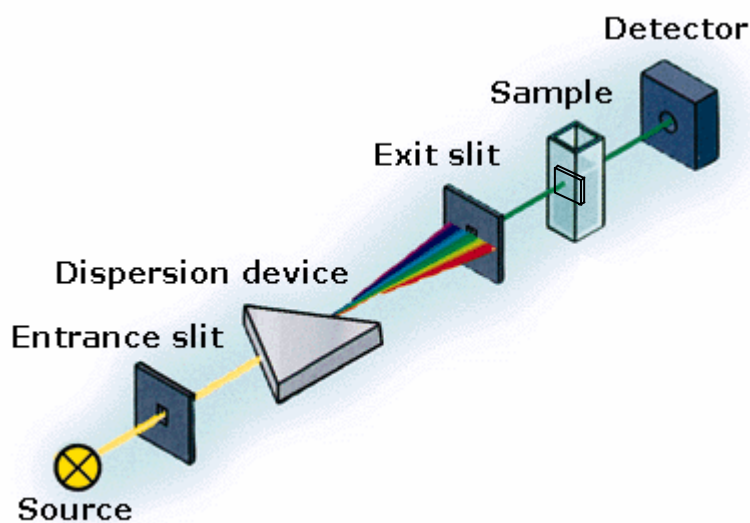


Figure 5.10 Schematic diagram of the UV-VIS spectroscopic set-up.



Figure 5.11 Photograph of the UV-VIS spectroscopic holder (at School of Chemistry, University of Bristol).

5.3.3. Estimation the Optical Band Gap

An example of transmittance spectrum as a function of wavelength is shown in Figure 5.12.

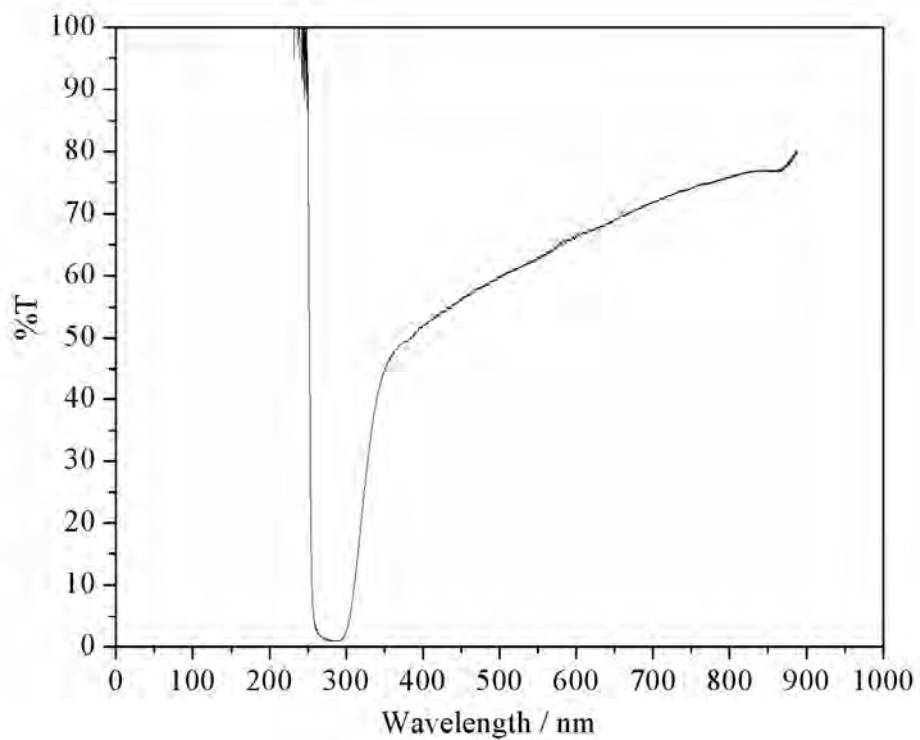


Figure 5.12 Example of transmittance spectrum as a function of wavelength.

In a Tauc plot, $(\alpha h\nu)^{1/2}$ is plotted as a function of $h\nu$. E_g can be determined approximately as 1.8 eV (in this particular example) from estimation of the intercept of the extrapolated linear fit with the Tauc plot curve, as shown in Figure 5.13.

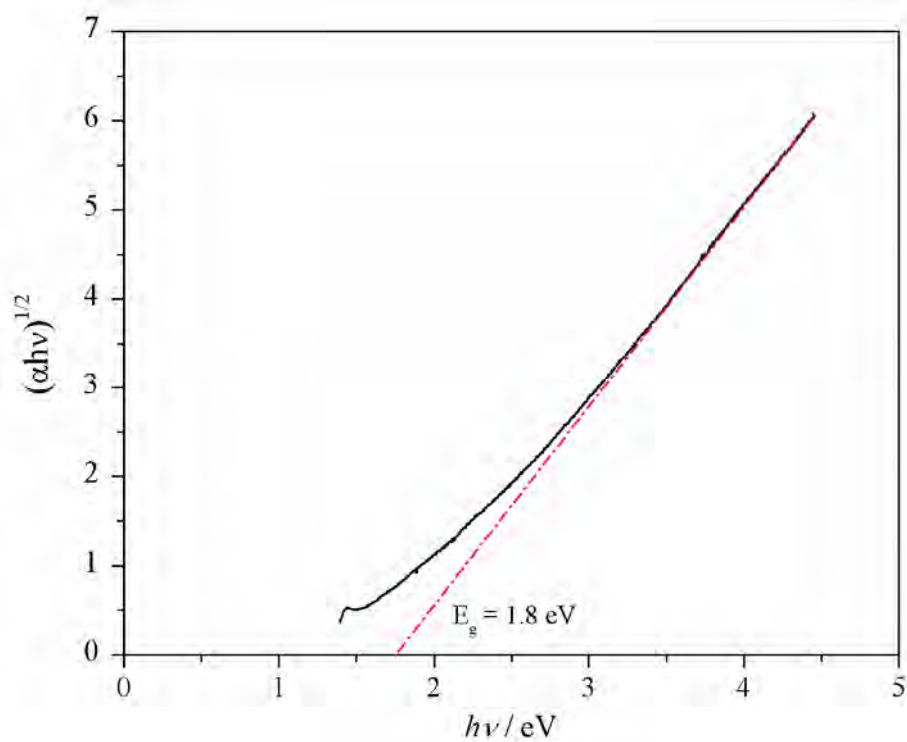


Figure 5.13 Example of a Tauc plot from a DLC film deposited at room temperature and 10 J/cm^2 .

5.3.4. UV-VIS Setup

UV-VIS spectroscopy was recorded in the range of 200-1000 nm on a Perkin Elmer Lambda Bio 10 UV/VIS spectrometer. The DLC and S-DLC films were grown on quartz substrates about 1 cm^2 in size, and then put into the quartz substrate holder (cuvettes) and mounted vertically so that UV/visible light could pass through them to a detector. The transmitted light was measured and stored by a computer. In each measurement the background was first recorded from a clean quartz substrate and then subtracted from those from the sample. The Tauc optical band gaps were then calculated.

5.4. Linear Four-Point Probe Measurement

5.4.1. Introduction

The Linear Four-Point Probe technique is used to measure the sheet resistivity of film. It is popular because the measured films are (usually) not damaged and using this technique is not difficult. The advantage of using Linear Four-Point Probe is the ability to obtain the resistivity without the complication of a contact resistance.

5.4.2. Theory

This technique involves bringing four equally spaced metal probes with known radius into contact with the film of unknown resistance. The probes are usually placed in the centre of the film. The schematic representation and photograph of a Linear Four-Point Probe is shown in Figures 5.14 and 5.15, respectively.

In the measurement, the height of the film can be adjusted by moving the mechanical stage. The sample is carefully moved upwards until the four spring-loaded probes come into contact with the surface. A high impedance current source is used to supply current through the two outer probes. The two inner probes sense the resulting voltage drop across the film. If probes with uniform spacing s are placed on an infinite slab material, then the resistivity, ρ , is calculated from:

$$\rho = 2\pi s \times \frac{V}{I} \quad \text{for } t \gg s \quad (5.6)$$

and

$$\rho = \frac{\pi}{\ln 2} \times \frac{V}{I} \times t \quad \text{for } s \gg t, \quad (5.7)$$

where ρ is the resistivity of the films ($\Omega\cdot\text{cm}$), V is the measured voltage (volts), I is the source current (A), and t is the film thickness (cm). For shallow layers, the above equation gives the sheet resistance R_s as

$$R_s = \frac{\rho}{t} = \frac{\pi}{\ln 2} \times \frac{V}{I} = 4.53 \times \frac{V}{I} \quad \text{for } s \gg t. \quad (5.8)$$

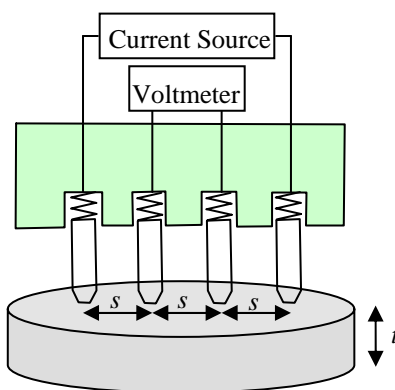


Figure 5.14 Schematic diagram of a Linear Four-Point Probe.

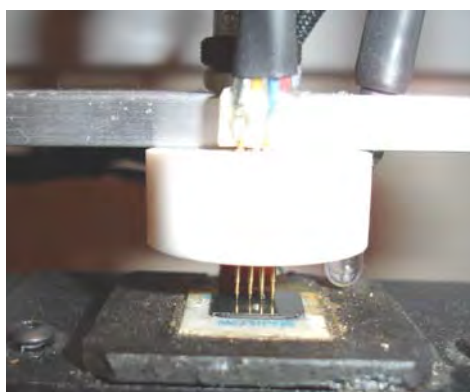


Figure 5.15 Photograph of a Linear Four-Point Probe (at School of Chemistry, University of Bristol).

5.4.3. Linear Four-Point Probe Setup

Linear Four-Point Probe analysis was conducted on a Solartron SI 1287 connected to a spring-loaded Four-Point Probe housed in a metal box acting as a 'Faraday cage'. The purpose of this was to shield the probe from any external electric fields. The *Labview* program controlled the input current, measured the output voltage and showed the resistance value of the films on the computer, while the thickness of the films was determined from separate SE measurements. The resistivity of the films by following the procedure given in Section 5.4.2.

5.5. Hall Effect Measurement

5.5.1. Introduction

Hall Effect measurement is a common technique used to characterise the charge-carrier concentration of a conducting sample. This technique applies a current across the sample in a magnetic field and measures the corresponding Hall voltage across the sample.

5.5.2. Theory

The Hall Effect is the production of a voltage difference across an electrical conductor transverse to the direction of an electric current, and perpendicular to the applied magnetic field. The nature of the current in a conductor is the movement of many small charge carriers, typically electrons, holes, or both. These charges move under the Lorentz Force. When a perpendicular magnetic field is applied to an electrical conductor, the charged particles' path becomes deflected, and charges become accumulated on one side of electrical conductor. This makes a new electric field in the electrical conductor perpendicular to both the direction of the electric current and the magnetic field. Opposite charged particles move to opposite sides of conductor. The Hall Effect is shown in Figure 5.16 and the apparatus required is in Figure 5.17.

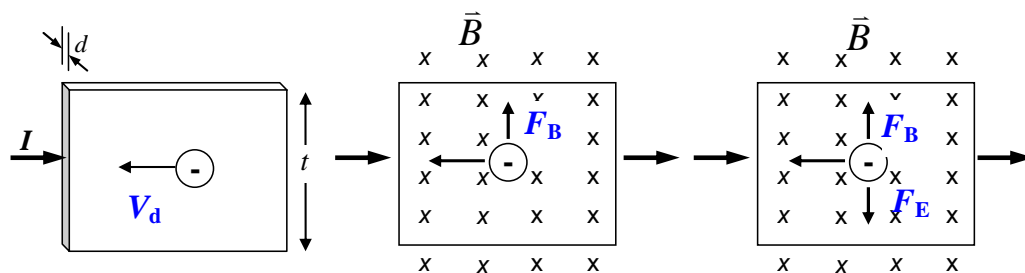


Figure 5.16 Schematic diagram of the Hall Effect.

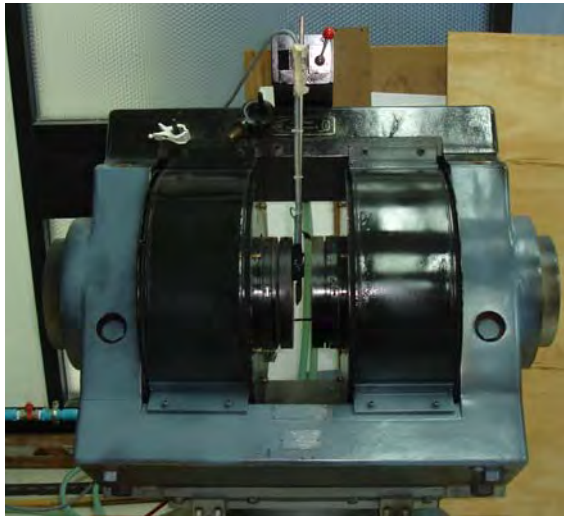


Figure 5.17 Photograph of Hall Effect apparatus (Department of Physics, Chulalongkorn University).

The opposite charges accumulated on one side of the electric conductor make a voltage difference, called the Hall potential difference or Hall voltage (V_H), given by

$$V_H = \frac{IB}{dne}, \quad (5.9)$$

where I is the current across the conductor (A), B is the magnetic flux density (T), d is the depth of the conductor (m), e is the electron charge (C), and n is the charge carrier density of the carrier electrons (cm^{-3}).

In semiconductors the carrier mobility (μ) indicates how easily a carrier moves in a particular material. This value is defined as the ratio of carrier velocity in the field direction to the magnitude of electric field. Therefore this value will be controlled by the carrier concentration, and is given by

$$\mu = \frac{1}{\rho ne}, \quad (5.10)$$

where n is the charge carrier density of the electrons (cm^{-3}), e is the electric charge (1.602×10^{-19} C), ρ is the resistivity value ($\Omega\text{-cm}$) and μ is the Hall mobility ($\text{cm}^2 \cdot \text{V}^{-1} \cdot \text{s}^{-1}$).

5.5.3. Hall Effect Setup

In the Hall Effect measurement, the $1 \times 1 \text{ cm}^2$ deposited DLC film was attached with four wires at the corners of a sample; two diagonal- wires were connected with a DC power supply (GPR-60H15D) to apply the current across the sample in the microampere range, while the other two diagonal wires were connected to a voltmeter to measure the Hall voltage value. The film was positioned perpendicular to a 600 mT magnetic field supplied by two large magnets either side of the sample.

5.6. Scanning Electron Microscopy (SEM) and Energy Dispersive X-ray Spectroscopy (EDX)

5.6.1. Introduction

SEM is a type of electron microscopy. This is the most popular technique use to look the film morphology, and is widely used in material science. The advantage of this technique is that it produces very high-resolution images of a sample surface, due to the very high energy of the electron beam. SEM has a large depth-of-field and spatial resolution yielding a characteristic image useful for understanding the surface structure of a sample. Moreover, SEM can be used jointly with another technique, such as, Energy Dispersive X-ray Spectroscopy (EDX) and Wavelength Dispersive Spectrometry (WDS) for achieving chemical analysis of the surface atoms.

5.6.2. Theory

The principle of SEM is based on the interaction of an incident electron beam and the solid specimen. Electron bombardment can produce a wide variety of emissions from the specimen, including secondary electrons, backscattered electrons (BSE), characteristic X-rays and Auger electrons.

When an incident electron collides with an electron in a sample atom, it will knock the electron out of its orbital shell and the atom will become ionized. These electrons generated as ionization products are called the secondary electrons, and can be collected by a detector. The secondary electron image is closely related to the sample topography. BSE measures the intensity of scattered electrons when incident electrons collide with the nuclei of surface atoms. The intensity of backscattered electrons depends directly on the atomic number; therefore, BSE can be used to discern differences in sample atomic number.

After a secondary electron is produced, a vacancy in an electron shell will be generated. An electron in an outer shell with higher energy drops down to fill the vacancy in an inner shell. The surplus energy of the electron can be released in two ways. It may be as a characteristic X-ray. X-rays have a characteristic energy unique to the element from which they originate and so provide compositional information about a sample. Alternatively, the surplus energy can be given to a third electron, which will be ejected from the atom (and the surface) with a characteristic energy. This electron is called an Auger electron.

Figures 5.18 and 5.19 show a schematic diagram of a simple SEM and a photograph of an SEM, respectively. An SEM consists of three parts: an electron column, a detection system, and a viewing system. In operation, two electron beams are controlled simultaneously by the same scan generator. One is the incident electron beam and the other is for the cathode ray tube (CRT) screen. The electron beam is rastered across the sample, and the secondary electron signal is detected and amplified to moderate the intensity of the second electron beam. A map of this emission with scanned area of the sample is shown on the CRT screen in real time. The SEM image can adjust the brightness, reflecting the surface morphologies of the specimen by changing the dimension of the area scanned on the sample surface. When an incident electron collides with the material, X-rays are emitted. These X-rays can be detected and then used to identify and analyze the elemental composition of the specimen surface. Secondary electron imaging and characteristic X-ray analysis were the primary functions used for SEM sample characterisation in this work.

5.6.3. SEM Setup

The sample was cleaved into two pieces and mounted on stubs, with one piece lying flat and the other at about 90° . The upright samples were intended to give cross-sections and the flat samples would give a plan view of the surface morphology. The beam of electrons was focused onto the specimen and scanned across the specimen surface. The reflected electrons were detected and converted to a visible image for example by a phosphor screen. The resulting images were stored electronically as bitmaps (*.bmp). In the SEM it was possible to use the X-ray analysis to get an elemental spectrum by linking to the *ISIS* program on the microanalysis computer. The kV and spot size needed to be increased to boost the signal and get sufficient readings to produce a spectrum. 20 kV with 15 mm working distance usually was used. Spectra were saved to the spectrum file or exported to tiff files.

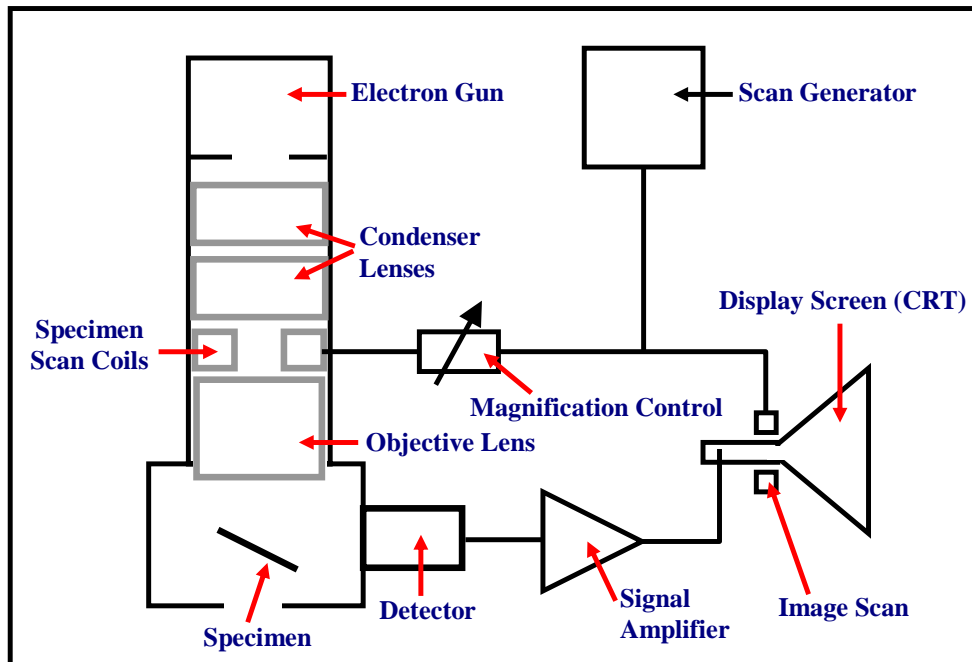


Figure 5.18 Schematic diagram of a simple SEM [119].



Figure 5.19 Photograph of an SEM (at School of Chemistry, University of Bristol).

5.7. Secondary Ion Mass Spectroscopy (SIMS)

5.7.1. Introduction

SIMS is widely used for analysis of the composition of a material, especially thin films. It is a very sensitive surface analysis method and is frequently used to detect low concentrations of dopant atoms in solids. This technique is concerned with ion bombardment of a sample surface by focusing a beam of high-energy ions in a UHV system. The effect of bombardment of a sample surface is the progressive removing of monolayer, and allows depth profiling of sample composition.

5.7.2. Theory

In SIMS, heavy ions (primary ion beam with 2 to 10 keV) are focused onto a sample surface in a UHV system. This causes neutral atoms, positively and negatively ions, electrons or clusters to be sputtered from the surface. Mass spectroscopy is employed to analyse these ejected species. However, the positive and negative ions cannot be detected at the same time. The dependent ion source used in SIMS must either run in positive or negative mode. An electropositive incident ion, Ar^+ , Cs^+ or Ga^+ , is used to increase the emission of negative species (-ve SIMS) and an electronegative

incident ion, O_2^+ , is used to increase the emission of positive species (+ve SIMS). At the same time, the sample is biased with the same polarity as the ion of interest to accelerate them away from the sample and into the mass spectrometer. Mass spectroscopy scans the charge-to-mass ratio abundances of the emitted ions, but cannot detect the neutral species. Accurate quantification of the species present is not possible, but with the use of depth profiling the homogeneity of the bulk composition can be analyzed. The basis principle of SIMS and a photograph of SIMS apparatus are shown in Figures 5.20 and 5.21, respectively.

5.7.3. SIMS Setup

Dynamic SIMS depth profiles used in this work were obtained using an in-house instrument comprising of an electronically variable aperture-type gallium-ion gun (FEI SD gallium LMIS EVA focusing column) fitted to a double-focusing magnetic-sector mass analyser (Vacuum Generators model 7035). A Ga^+ primary ion beam with 3 nA and 25 keV energy was scanned over an area of $65\ \mu m \times 65\ \mu m$ while monitoring the C^- , O^- , Si^- and $^{34}S^-$ secondary ions in order to obtain the depth profiles.

A gating facility was used to restrict ion counting to the centre of the etch pit in order to avoid edge effects. The system vacuum during operation was 10^{-7} Torr. The instrument was calibrated using values of 68.926 for the backscattered Ga^+ ions. The instrument control software was *Pisces* running under the Windows operating system. Dynamic SIMS depth profiles were obtained by continual secondary ion analysis whilst etching through the sample layer. The chemical distribution of an ion through the layer is presented on a percentage full scale (%Full Scale), where the full scale values for each ion is presented in the result.

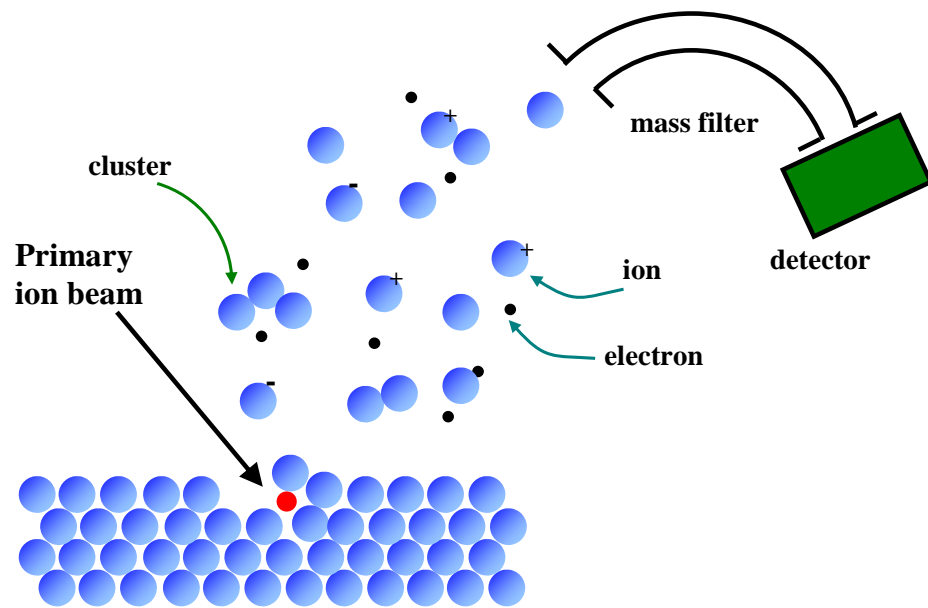


Figure 5.20 Basic principle of SIMS [120].

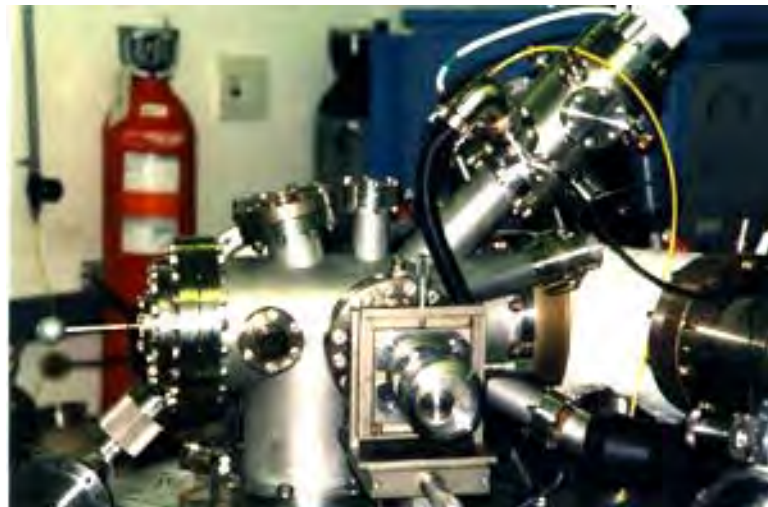


Figure 5.21 Photograph of SIMS apparatus (at Interface analysis centre, Bristol).

5.8. Nanoindentation

5.8.1. Introduction

Nanoindentation is a commonly used technique to investigate the hardness of thin films. The advantage of this technique is to avoid the delamination of thin films. This technique is concerned with applying load cycles of force onto the films. The area of the indenter load and depth of penetration is correlated with the film hardness.

5.8.2. Theory

Nanoindentation employs a hard tip, typically a diamond to press into the sample with known load. After the load is removed, the area of the residual indentation (A_r) in the sample, which may only be a few square micrometres or nanometres, is measured. The hardness (H) can be calculated by

$$H = \frac{P_{\max}}{A_r}, \quad (5.11)$$

where P_{\max} is the maximum load on the sample.

Images of the indentation can be carried out by atomic force microscopy, a scanning microprobe technique. However, these techniques are quite cumbersome. Alternatively, images of the indentation can be obtained by using an indenter with a geometry known to high precision. In the indentation process, the area of the indent is determined from the depth of penetration using the geometry of the indentation tip. The relation of load and depth of penetration is measured, recorded, and plotted on a graph to create a load-displacement curve. The hardness of the film can then be obtained. A schematic diagram of a load-displacement curve is shown in Figure 5.22. A photograph of Nanoindentation apparatus is shown in Figure 5.23.

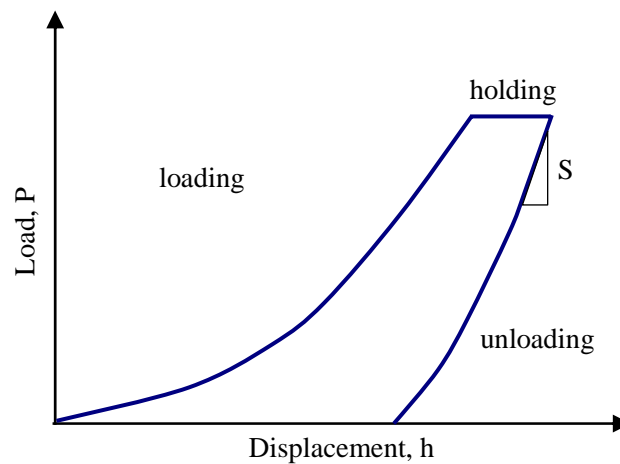


Figure 5.22 Schematic diagram of a load-displacement curve in Nanoindentation.



Figure 5.23 Photograph of Nanoindentation apparatus (at Nano shield co., Ltd, Thailand).

5.8.3. Nanoindentation Setup

The hardness of DLC films were investigated using a Nanoindentation (TTX-NHT) characterisation system. For all films, ten measurements of indentations at different surface locations were carried out in order to derive the hardness as a function of the deposition parameters via computation. Indentation curves were obtained with loading and unloading rates of 6-10 mN/min. The hardness of the films was calculated from load-penetration curves and the results were transferred via computer.

CHAPTER VI

RESULTS AND DISCUSSIONS

Following the description of characterisation techniques in Chapter 5, we will now discuss the characterisation results for the film electrical, optical, physical, and structural properties. For the electrical properties, the carrier concentration and the Hall mobility were obtained by Hall Effect measurement. The resistivity value was obtained by Linear Four-Point Probe. For the optical properties, the refractive index and extinction coefficient were obtained from SE. The E_g was measured from both SE and UV-VIS. For the physical properties, the surface morphology and the film thickness were determined by SEM and SE, respectively, while the hardness of films was measured by Nanoindentation. Finally, for the structural properties, the chemical bonding structure was analysed by LRS and the elemental components of the films were identified by EDX and SIMS.

6.1. Electrical Properties

6.1.1. Film Resistivity

The film resistivity values were obtained from the multiple sheet resistance values and the thickness values of each of film. The sheet resistance values were obtained from the slope of the current-voltage characteristic of films, which was measured by using Linear Four-Point Probe and the equations (5.6)-(5.8) given in Section 5.4.2. An example of current-voltage characteristic of S-DLC film deposited at 0% sulphur molar percentage at 150° C with 10 J/cm² of laser fluence is shown in Figure 6.1.

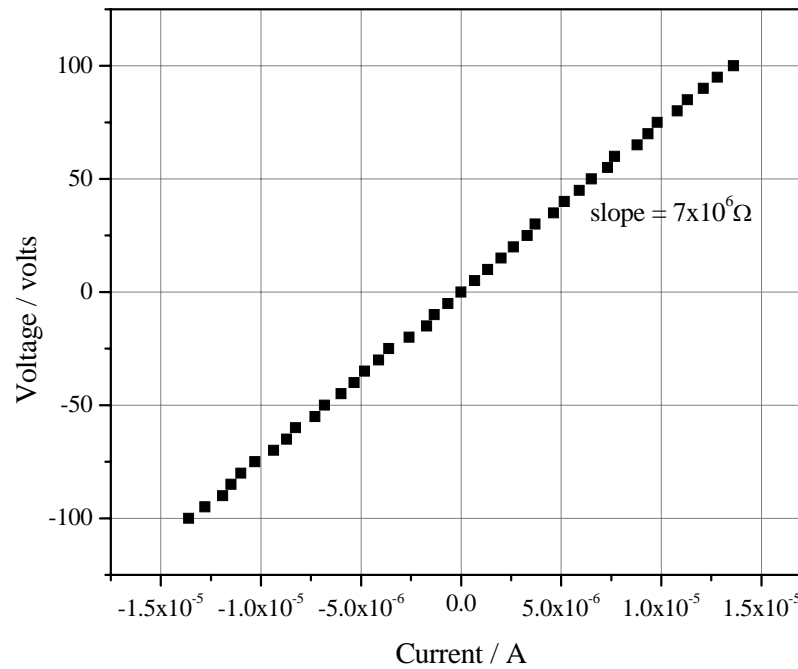


Figure 6.1 Example of a current-voltage characteristic from S-DLC film deposited at 0% sulphur molar percentage at 150°C with 10 J/cm^2 of laser fluence.

Figure 6.1 shows an example of a current-voltage characteristic from S-DLC films, which were found to be linear and symmetric as a result of the Ohmic contacts used for the measurement. The sheet resistance of this film was found to be $7 \times 10^6 \Omega$, which was obtained from the slope value of the current-voltage characteristic.

The thickness of all films was obtained from SE results, as shown in Section 6.3.2. The resistivity values of DLC and S-DLC films versus % atomic ratio of S/C at different substrate temperatures at 10 J/cm^2 and 20 J/cm^2 laser fluence is shown in Figure 6.2. The % atomic ratio of S/C in each of film at different deposition conditions was obtained from EDX results, as shown in Section 6.4.2.

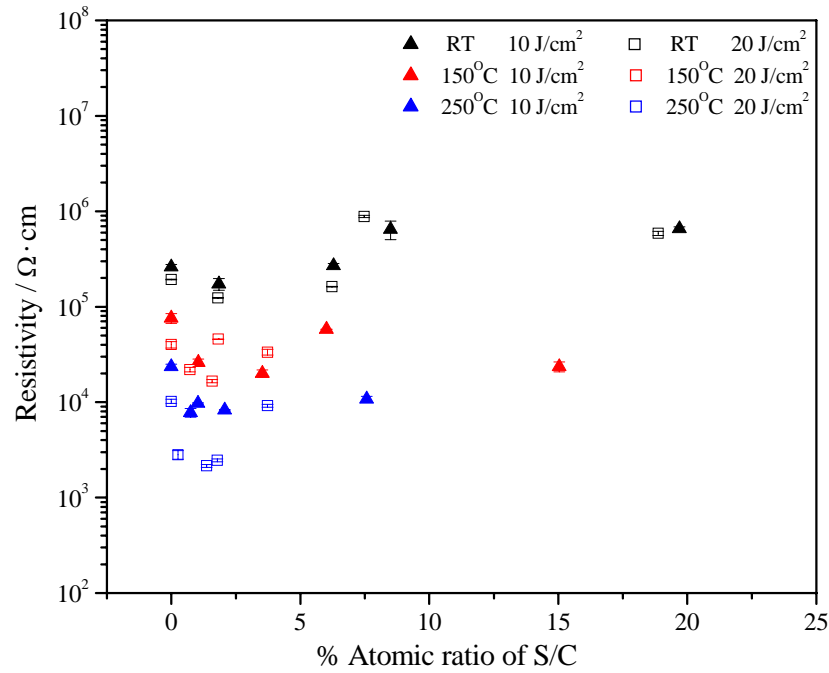


Figure 6.2 Resistivity values of DLC and S-DLC films versus % atomic ratio of S/C at different substrate temperatures and at 10 J/cm² and 20 J/cm² of laser fluence.

Figure 6.2 shows that the resistivity of DLC and S-DLC films is in the range 10³-10⁶ Ω·cm, depending upon the substrate temperature, laser fluence and % atomic ratio of S/C. Normally, the graphite and diamond films have resistivity values ~10⁻³ Ω·cm [121] and 10²⁰ Ω·cm [122], respectively. The resistivity values of the S-DLC films in this work were found to be between those of diamond and graphite, and were found to be in the same range of the resistivity values of DLC films in other work. The electrical resistivity of DLC films in other works were generally found to be in a larger range, from 10²-10¹⁶ Ω·cm [50], depending upon the deposition conditions and method used.

At different substrate temperatures, the films that were deposited at room temperature had the highest resistivity values in the range of 10⁵-10⁶ Ω·cm. The films that were deposited at 250 °C had the lowest resistivity values in the range of 10³-10⁵ Ω·cm. Films that were deposited at 150 °C had resistivity values in the range of 10⁴-10⁵ Ω·cm - between those of the films deposited at room temperature and 250 °C.

These results revealed that the temperature affected the structural and electrical properties of S-DLC films. This is because at higher substrate temperature the atoms in the film have time to thermally equilibrate. This results in films forming more sp^2 hybridization with more graphitic behavior at higher substrate temperature. Therefore, at higher substrate temperature the films became more conductive, and less diamond-like.

At different laser fluences, the films that were deposited at 10 J/cm^2 laser fluence had a higher resistivity value than the films that were deposited at 20 J/cm^2 . This may be due to the laser fluence having an effect on the kinetic energy of ions in ablation process. Thus, the increasing laser fluence increases the kinetic energy of the impacting carbon ions. This excess energy breaks many C-C bonds in the film, and when they reform they do so preferentially in the sp^2 hybridised form. Therefore, the films that were deposited with higher laser fluence also have more graphitic behavior.

At different % atomic ratio of S/C, the room temperature resistivity value of films decreased with increasing of % atomic ratio of S/C up to ~2%. But after that the resistivity value of films increased until at ~8% atomic ratio of S/C the films showed the highest resistivity value. Above ~8% atomic ratio of S/C the resistivity value reduced again. At 150°C substrate temperature, the resistivity value of films decreased with increasing of % atomic ratio of S/C until at ~2% atomic ratio of S/C the films showed the lowest resistivity value. After that the resistivity value increased and showed the highest resistivity value at ~6% atomic ratio of S/C, and reduced again after ~6% atomic ratio of S/C. At 250°C substrate temperature, the resistivity value of films decreased with increasing of % atomic ratio of S/C until at ~2% atomic ratio of S/C the films showed the lowest resistivity value. After that the resistivity value increased until ~8% atomic ratio of S/C.

We can conclude that the effect of a little sulphur doping on S-DLC films made the films show a decreasing resistivity value. This may be due to an increase in the number of free electrons in S-DLC films, donated by the S.

Therefore, S-DLC films have low resistivity value at low sulphur doping. In contrast, S-DLC films with higher sulphur content showed increasing resistivity values. Even though there would be more free electrons donated by the S, the large number of S atoms disrupt the conducting pathways within the structure hindering electron mobility. Therefore, the amount of sulphur doping can be used to adjust the structural and electrical properties of S-DLC films.

From these resistivity results we can conclude that the films contain more graphite with sp^2 hybridization with increasing substrate temperature and laser fluence. Sulphur was found to change the hybridization and resistivity value of films. The resistivity values were a complicated function of S content. S is thought to donate electrons to the structure, aiding conductivity, however too much S disrupts the lattice hindering conductivity. These resistivity value trends are consistent with the findings from both the optical, physical and structural results which will be discussed later.

6.1.2. Carrier Concentration and Hall Mobility

The carrier concentration and Hall mobility of the S-DLC films are two parameters which are of interest for electronic applications. Following the procedures described in Section 5.5, the carrier concentration and Hall mobility of S-DLC films at difference substrate temperatures, laser fluence and % atomic ratio of S/C were measured. The thickness of all films, which was used to calculate the carrier concentration and Hall mobility, is shown in Section 6.3.2. The carrier concentration result versus % atomic ratio of S/C at difference substrate temperature at 10 J/cm^2 and 20 J/cm^2 of laser fluence is shown in Figure 6.3. The % atomic ratio of S/C in each film at different deposition conditions was obtained from EDX results, as shown in Section 6.4.2.

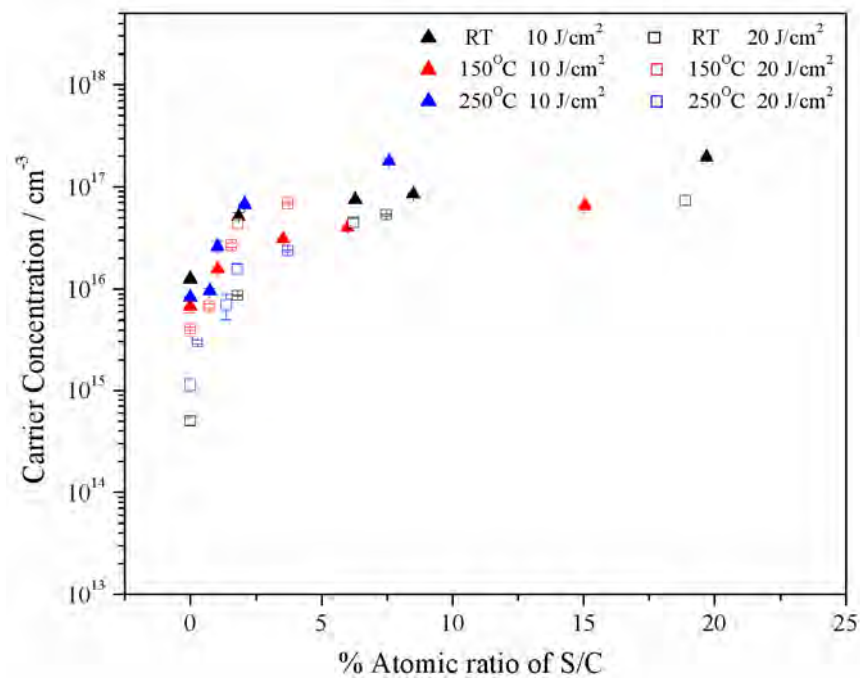


Figure 6.3 Carrier concentration of DLC and S-DLC films versus % atomic ratio of S/C at difference substrate temperatures at 10 J/cm^2 and 20 J/cm^2 laser fluence.

The Hall Effect measurements verified the presence of free carriers in S-DLC films. The carrier concentration was in the range of 10^{14} to 10^{18} cm^{-3} . The effect of doping the DLC films with sulphur was to convert the films into an n-type semiconductor.

At different substrate temperatures, the carrier concentration did not show a clear trend with % atomic ratio of S/C. For the same sulphur molar percentage in the target, the films deposited at room temperature were found to have higher carrier concentration than the films at 150°C and 250°C . Due to the melting point of sulphur $\sim 112.8^\circ\text{C}$, the S may be preferentially evaporated out of the target before the ablation process occurs. Therefore, the amount of sulphur that is incorporated into the substrate decreases with increasing substrate temperature for the same sulphur molar percentage in the target.

Another cause is that the increasing substrate temperature increases the thermal expansion of the films, therefore, increasing the probability of C and S atoms moving to a favourable position. However, S atoms are larger than C atoms; therefore, they will be less mobile.

At different laser fluences, the films that were deposited at higher laser fluence showed the lower carrier concentration because the increase of laser fluence increases the ion excess kinetic energy. This effect makes sulphur preferentially sputter off the films due to the etching of the surface.

The carrier concentration of S-DLC films increased rapidly with increasing % atomic ratio of S/C from 0% to 10%. After 10% atomic ratio S/C, the carrier concentration of S-DLC films showed a little increase with increasing % atomic ratio of S/C. This is because when the sulphur molar percentage in the target increases it increases the probability of incorporation of sulphur into DLC films. Therefore, it increases the carrier concentration of S-DLC films. The increasing % atomic ratio of S/C between 0-10% had a greater effect on the increasing carrier concentration in films. This is because S can act as a carrier in films at 0-10% atomic ratio of S/C. Above 10% atomic ratio of S/C, the large number of S atoms disrupt the conducting pathways within the structure. Therefore, the increasing S content in the films did not show an increase in carrier concentration.

The Hall mobility result versus % atomic ratio of S/C at difference substrate temperatures and at 10 J/cm^2 and 20 J/cm^2 of laser fluence is shown in Figure 6.4. This figure shows that the Hall mobility of S-DLC films was in the range of 10^{-5} to $1 \text{ cm}^2 \cdot \text{V}^{-1} \cdot \text{s}^{-1}$, depending on the substrate temperature, laser fluence and % atomic ratio of S/C. In this study, the mobility value of the films was a minimum at room temperature, 10 J/cm^2 of laser fluence and 25% of sulphur molar percentage, and was a maximum at $250 \text{ }^\circ\text{C}$ substrate temperature, 20 J/cm^2 of laser fluence and 1% of sulphur molar percentage.

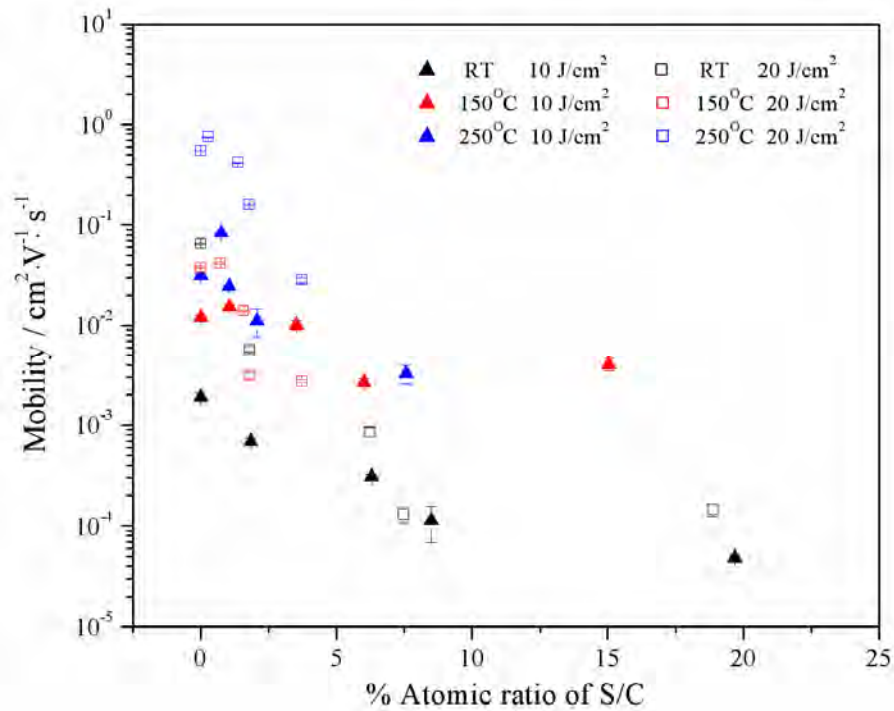


Figure 6.4 Hall mobility of DLC and S-DLC films versus % atomic ratio of S/C at difference substrate temperatures at 10 J/cm² and 20 J/cm² laser fluence.

At different substrate temperatures, the Hall mobility was found increase with increasing substrate temperature. This may be due to the arrangement of the carbon atoms at higher substrate temperature being more like crystalline graphite than at lower substrate temperature.

At higher laser fluences, the carrier concentration was found decrease but the Hall mobility was found to increase with increasing laser fluence. This is because at higher laser fluence the higher kinetic energy will implant the ions into the substrate making the films have a more crystalline structure than at lower laser fluence.

At different % atomic ratios of S/C, the Hall mobility of films decreased with increasing % atomic ratio of S/C. This means that an addition of sulphur into the films produces crystalline defects and increases the scattering by increasing the number of unionized S atoms. Therefore the films have decreased Hall mobility at higher sulphur doping.

However, for the films that were deposited at 150 °C and 250 °C, with both laser fluencies it was found that the mobility increased at less than 1% atomic ratio of S/C and also decreased with increasing of % atomic ratio of S/C. This is because the amount of sulphur in the films at these conditions can help to increase the crystalline structure of films.

6.2. Optical Properties

6.2.1. Refractive Index and Extinction Coefficient

The refractive index (n) and extinction coefficient (k) values were measured by SE. Figure 6.5 shows an example of how n and k vary as a function of 1-5 eV photon energy for a DLC film deposited at room temperature and 10 J/cm². In this DLC film, n and k were found to be in the range 2.6-2.7 and 0-0.6, respectively. The value of k was found to increase with increasing photon energy. The value of n was found to increase with increasing photon energy to 3 eV and then to decrease with increasing photon energy after that. The n and k values of DLC films in this work were found to be similar to those found by other workers.

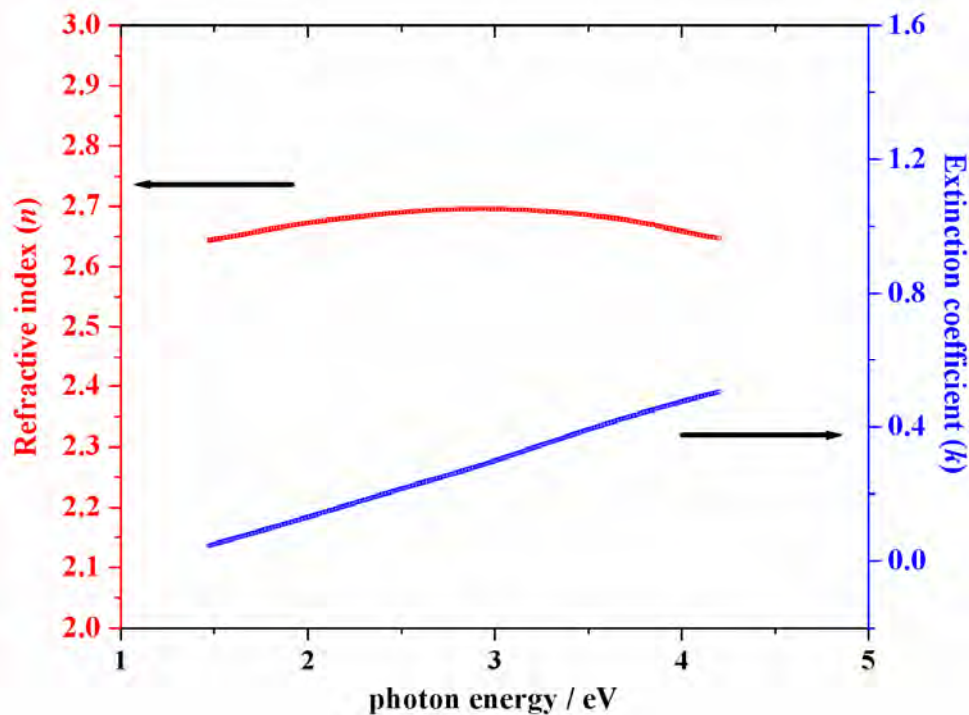


Figure 6.5 Example of n and k values of DLC films.

In comparison, Xiong *et al.*, deposited DLC films by the PLD method with an ArF excimer laser at 193 nm. They concluded that their DLC films have excellent properties. This is because their films have more than 95% sp^3 content. The n and k values of this type of high quality DLC films are in the range of 2.5-2.8 and 0-0.5, respectively [4]. So this can be used to explain that the DLC films in this work should have more diamond-like properties or a high sp^3 carbon bond fraction.

6.2.2. Optical Band Gap

In Sections 5.2 and 5.3, we showed the procedure for measuring the E_g as a function of photon energy of S-DLC films using UV-VIS and SE. The E_g result versus % atomic ratio of S/C at difference substrate temperatures at 10 J/cm^2 and 20 J/cm^2 of laser fluence are shown in Figures 6.6 and 6.7, respectively. The % atomic ratio of S/C in each film at different deposition conditions was obtained from EDX results, as shown in Section 6.4.2.

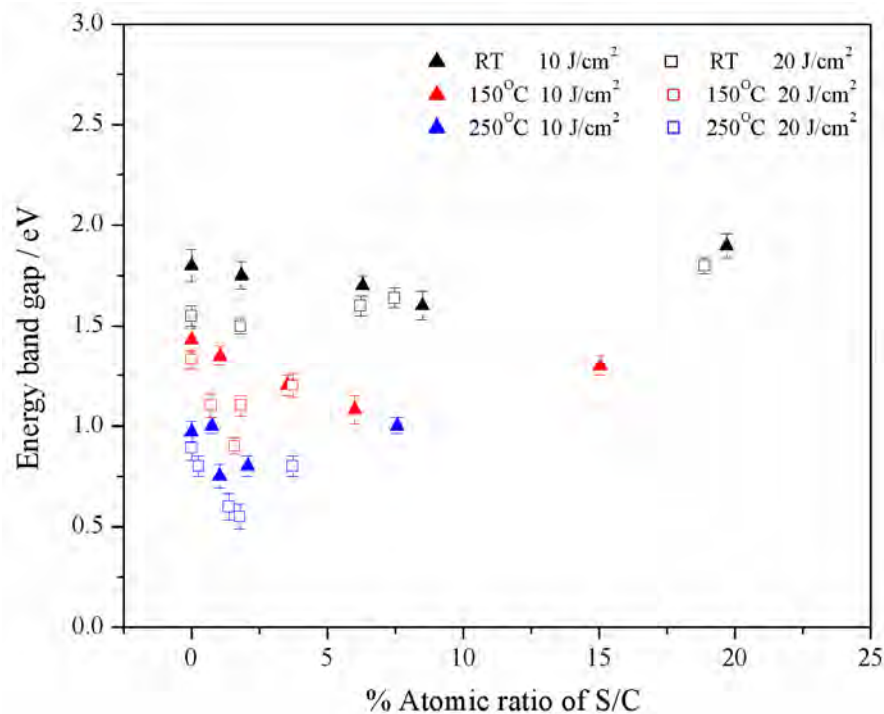


Figure 6.6 Energy band gap of DLC and S-DLC films measured by UV-VIS.

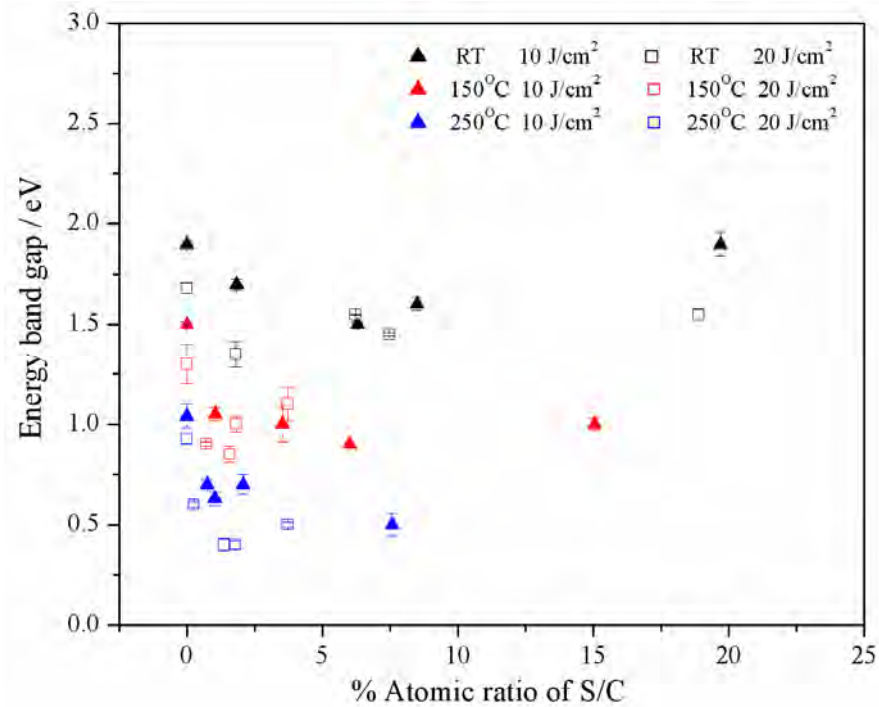


Figure 6.7 Energy band gap of DLC and S-DLC films measured by SE.

The E_g of a DLC film is directly related to the structure within the film. Generally, diamond has a large indirect band gap of 5.5 eV whereas graphite has effectively no band gap. Therefore, DLC and S-DLC should have the E_g , which can be tunable in the range of 0-4 eV.

Figures 6.6 and 6.7 verified that the trends in E_g from UV-VIS were found to be the same as those from SE. These figures show that the E_g of DLC and S-DLC films were found in the range 0.25-2.00 eV, depending upon the substrate temperature, laser fluence and % atomic ratio of S/C. The substrate temperature had a much greater effect on the E_g trend than other parameters, while laser fluence was the second most important. The E_g of S-DLC films did not show a definite trend with increasing of % atomic ratio of S/C.

At different substrate temperatures, the E_g of S-DLC films that were deposited at room temperature had the highest E_g values, in the range 1.50-2.00 eV. The films that were deposited at 250 °C had the lowest E_g values in the range through 0.25-1.00 eV. The films that were deposited at 150 °C had E_g values in the range 0.75-1.50 eV, intermediate between the values for films deposited at room temperature and at 250 °C. The E_g of DLC films at room temperature with 10 J/cm² of laser fluence was found to be approximately 1.90 eV. All of these results are similar to those from laser-deposited DLC films in other work, shown in Section 3.3 [4, 38, 115-117].

The substrate temperature has an effect on the E_g of films: E_g decreases at higher substrate temperature. These results confirm that the films had more graphitic behavior at higher substrate temperatures. These results also provide evidence for the idea that S changes the DLC film structure, which is consistent with the resistivity results.

At different laser fluences, the highest value of E_g at 10 J/cm² laser fluence was higher than that in the trend of E_g at 20 J/cm² laser fluence. This means that DLC films deposited at high laser fluence led to graphitization of the films. These results are consistent with resistivity results, which decreased with increasing laser fluence.

We can conclude that the E_g decreased with increasing substrate temperature and laser fluence, and this is related to fact that the films contain more graphite with sp² C hybridization. These E_g results were found to be similar to those from laser-deposited DLC films in other work. The effect of % atomic ratio of S/C changed the hybridization of films in an unpredictable manner.

6.3. Physical Properties

6.3.1. Surface Morphology

The morphology of S-DLC films was observed by SEM analysis. SEM indicated that micron-sized particulates were found on the surface of S-DLC films. The particulates in this work were found to be dependent upon the substrate temperature, laser fluence and sulphur molar percentage.

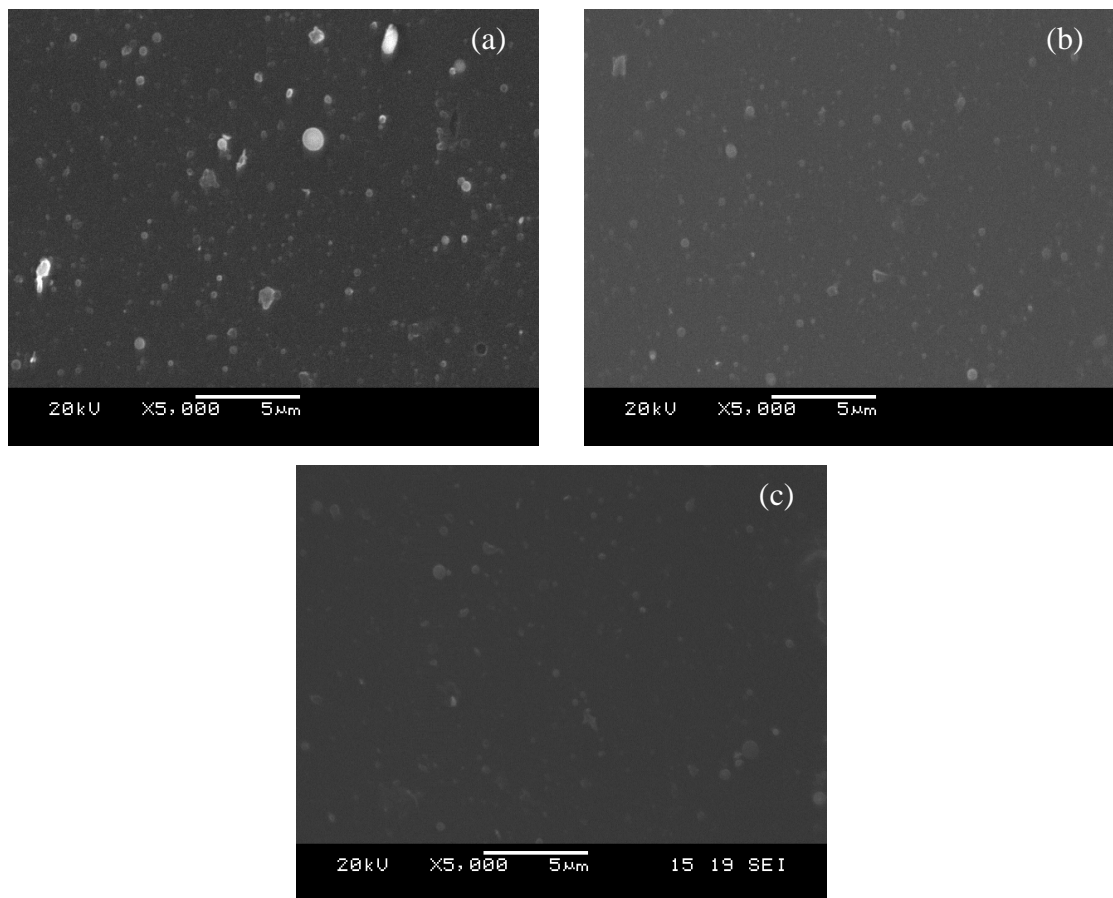


Figure 6.8 Morphology of S-DLC films on the silicon substrate determined by SEM at 1% sulphur molar percentage with 10 J/cm^2 laser fluence and various substrate temperatures; (a) room temperature, (b) $150 \text{ }^\circ\text{C}$, and (c) $250 \text{ }^\circ\text{C}$.

The main causes of particulates in these films is the structure of the target, as compressed graphite and sulphur powder will have cracks, protrusions and trapped gas. All of these will be dislodged due to thermal and mechanical shock or by the ablation action. This particulate problem holds back the use of PLD in many electronic and optical applications which require extreme surface smoothness. However, particulates are a common feature in any laser-deposited thin films [5, 8, 123] .

Figure 6.8 shows examples of the effect of substrate temperature on surface morphology of S-DLC films at 1% sulphur molar percentage with 10 J/cm^2 laser fluence and 3 substrate temperatures; (a) room temperature, (b) 150°C , and (c) 250°C . It is clear that the film deposited at higher substrate temperature has less particulates than the film deposited at lower substrate temperature.

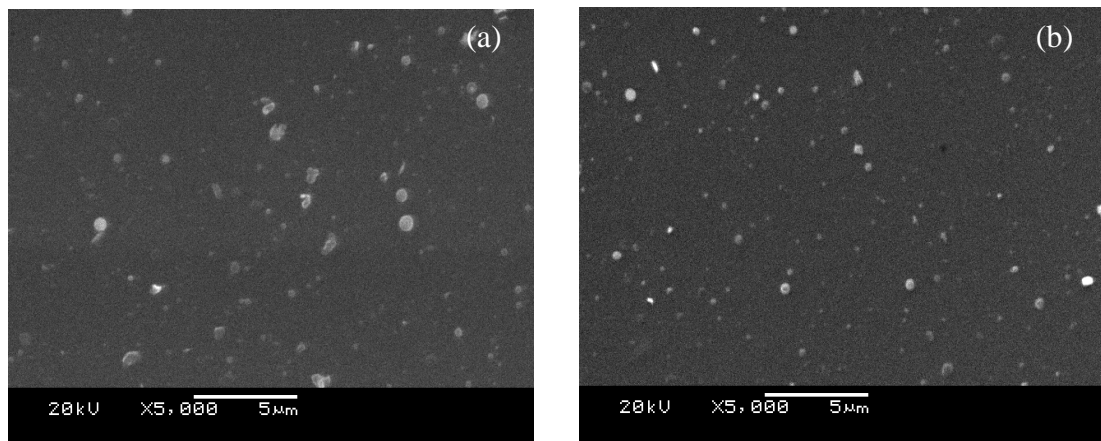


Figure 6.9 Morphology of S-DLC films on the silicon substrate determined by SEM at room temperature with 0% sulphur molar percentage and 2 laser fluences; (a) 10 J/cm^2 , and (b) 20 J/cm^2 .

Figure 6.9 shows examples of the effect of laser fluence on the surface morphology of S-DLC films at room temperature with 0% sulphur molar percentage and 2 laser fluences; (a) 10 J/cm^2 , and (b) 20 J/cm^2 . It was found that the deposited films at higher laser fluence show smaller-sized particulates than films deposited at lower fluence.

Figure 6.10 shows examples of the effect of sulphur molar percentage on surface morphology of S-DLC films at 250 °C substrate temperature and 10 J/cm² laser fluence and various sulphur molar percentages; (a) 1%, (b) 5%, (c) 10%, and (d) 25%. It was found that S-DLC films at higher sulphur incorporation had an abundance of particulates due to the higher non-uniformity of the target composition at higher sulphur molar percentage. During ablation, targets with higher sulphur molar percentage allow particulates to be dislodged more easily than those with lower sulphur molar percentage. This can be seen in more detail in Section 3.2.4.

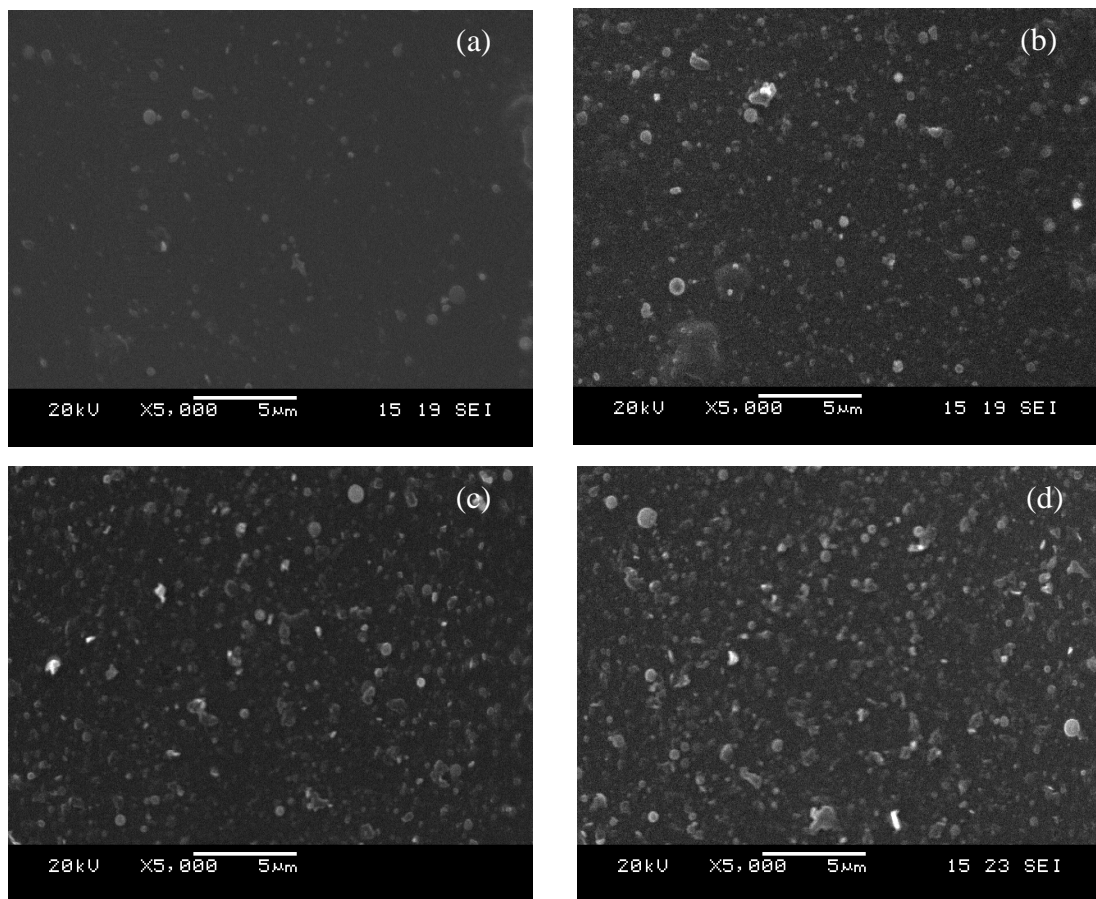


Figure 6.10 Morphology of S-DLC films on the silicon substrate determined by SEM at 250 °C substrate temperature and 10 J/cm² laser fluence and various sulphur molar percentages; (a) 1%, (b) 5%, (c) 10%, and (d) 25%.

6.3.2. Film Thickness

All film thicknesses and SiO₂ layers were measured by SE. First, the thickness of the SiO₂ layer was measured to calibrate the substrate for SE. The thickness of the native SiO₂ layer in this work was found to equal 4.13 nm; therefore, the known substrate thickness will consist of 1 mm of silicon substrate and 4.13 nm of SiO₂ layer. The film thickness of S-DLC films versus sulphur molar percentage at difference substrate temperature at 10 J/cm² and 20 J/cm² of laser fluence is shown in Figure 6.11. This figure shows that the thickness of films on the silicon substrate was in the nanometre range. The SEM cross-section in Figure 6.12 also confirms that the thickness of the DLC films was in the nm range.

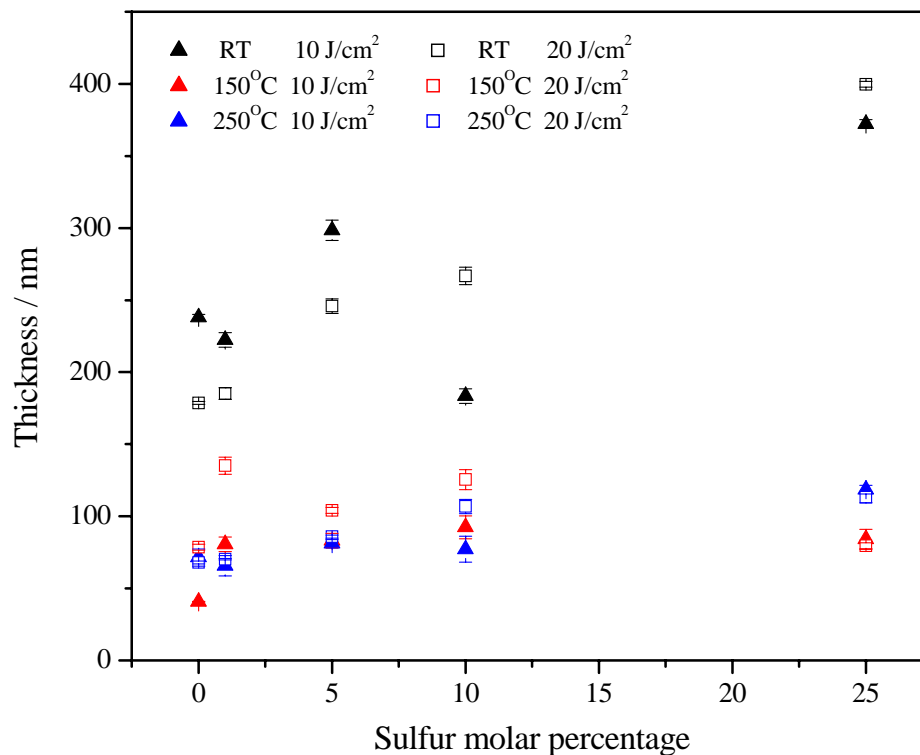


Figure 6.11 Film thickness versus sulphur molar percentages at different substrate temperatures and laser fluence.

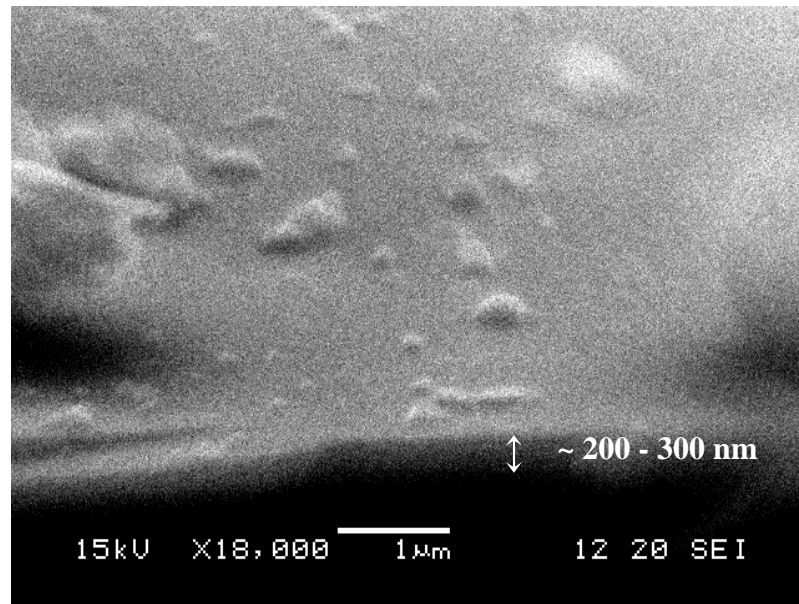


Figure 6.12 Cross-sectional SEM analysis of an S-DLC film on a silicon substrate.

The thickness of the films in this work did not show a clear trend with three parameters; this is may be due to non-uniformities in the graphite and sulphur target, and any cracks, protrusions and trapped gas present on the target surface. The effect of substrate temperature can be estimated by the measured thickness trend. The film deposited at higher substrate temperatures were thinner than those films deposited at lower substrate temperatures. This may be because at higher substrate temperatures the increased thermal expansion of films anneals the films somewhat, leading to thinner and smoother films. These results are consistent with SEM results, which showed that films became smooth with high substrate temperature, as showed in Figure 6.8.

Figures 6.9 and 6.10, as found related to Figure 6.11, showed that the smoothness of films are proportional to the thinness of films: the film thickness is proportional to the number of particulates.

6.3.3. Film Hardness

The hardness of DLC and S-DLC films was assessed by Nanoindentation. The hardness of S-DLC films that were deposited at room temperature and 150 °C at 10 J/cm² of laser fluence with various sulphur molar percentages are shown in Table 6.1. The hardness of DLC films that were deposited at room temperature with 0% sulphur molar percentage with difference laser fluence are shown in Table 6.2.

sulphur molar percentage	Hardness / GPa	
	room temperature	150 °C
0%	29.2±0.6	12.4±0.9
1%	26.5±4.3	15.3±0.3
5%	26.5±2.1	17.4±3.2
10%	11.9±1.9	15.3±3.1

Table 6.1 Hardness of S-DLC film deposited at 10 J/cm² of laser fluence at various sulphur molar percentage and at room temperature and 150 °C.

laser fluence / (J/cm ²)	Hardness / GPa
10	29.2±0.6
20	20.5±0.4

Table 6.2 Hardness of DLC film deposited at room temperature at 0% sulphur molar percentage at 10 J/cm² and 20 J/cm² laser fluence.

The hardness of pure DLC films deposited at room temperature and at 10 J/cm^2 and 20 J/cm^2 laser fluence was in the range 29.2 ± 0.6 and 20.5 ± 0.4 GPa, respectively. The normal range for DLC hardness is 10-20 GPa, while high quality DLC films normally have a hardness in the range 20-40 GPa, depending on the deposition conditions [4, 124]. 'High quality' DLC films means the film has more than 95% of sp^3 content. Therefore, the pure DLC films deposited in this work can be regarded as having properties close to that of diamond-like properties. By their remarkable hardness, it can be concluded that pure DLC films deposited at room temperature at 10 J/cm^2 of laser fluence should have more diamond-like properties than pure DLC films deposited at room temperature and 20 J/cm^2 laser fluence. In comparison, Xiong *et al.* deposited DLC films by a PLD method with an ArF excimer laser at 193 nm. They concluded that their DLC films are high quality.

Tables 6.1 and 6.2 showed that the substrate temperature, laser fluence and sulphur molar percentage strongly influenced the mechanical properties of the films. In this dissertation, the films deposited at higher substrate temperature displayed lower hardness. This result is consistent with other workers results. In comparison, Kumar *et al.*, [8] studied the effect of substrate temperature on DLC films. They found that the hardness of DLC films decreased with increasing substrate temperature, and that the films had more graphitic behavior at higher substrate temperature. Therefore, we can conclude that films deposited at higher substrate temperatures in this work should be less diamond-like, and this result corresponds with the results from measurements of the electrical and optical properties.

For room-temperature-deposited S-DLC films the hardness showed a little increase at 1% and 5% of sulphur molar percentage, but showed a sharp decrease at 10% S. This may be due to the softness of elemental sulphur. In sulphur-incorporated DLC films at higher molar percentage; an effect of sulphur will be approximated and appeared in the hardness results. However, the hardness of S-DLC films deposited at 150°C seemed to be constant with increasing sulphur molar percentage. This is because at higher substrate temperatures less S was incorporated in the films due to the S preferentially evaporating.

The hardness of DLC films decreased with increasing laser fluence. At higher laser fluence the ions have high kinetic energy, and disrupt the structure changing it into sp^2 hybridization. Therefore, at 20 J/cm^2 of laser fluence sp^2 hybridization was found in a soft film, while at 10 J/cm^2 of laser fluence sp^3 hybridization was found in a hard film. Although S-DLC films in some deposition conditions in this work showed hardness values below 20 GPa, they are still classed as being DLC films by the LRS characterisation.

6.4. Structural Properties

6.4.1. G Peak Position and I_D/I_G Ratio

All Raman spectra in this dissertation were measured by LRS. Figure 6.13 shows three Raman spectra, a DLC spectrum, a diamond spectrum, and a graphite target spectrum. The difference between all of these spectra can be seen from the peak positions and intensities. The graphite target spectrum gives two sharp characteristic peaks, the ordered graphite peak at $\sim 1570 \text{ cm}^{-1}$ and the disorder peak at a $\sim 1335 \text{ cm}^{-1}$. The intensity of the graphite peak is very high when compared with the intensity of the disorder peak. The diamond spectrum gives only one sharp diamond peak at 1332 cm^{-1} . The DLC spectrum shows only a broad graphite peak, with the disappearance of the disorder line. Although the characteristics of the diamond peak at 1332 cm^{-1} disappear in a DLC spectrum this does not indicate the absence of sp^3 bonding in DLC films.

All Raman spectra in this work were analyzed to determine how the substrate temperature, laser fluence and sulphur molar percentage affect both the G and D peak positions. These spectra are consistent with the spectral characteristic seen from other DLC films. All Raman spectra are shown in Appendix A.

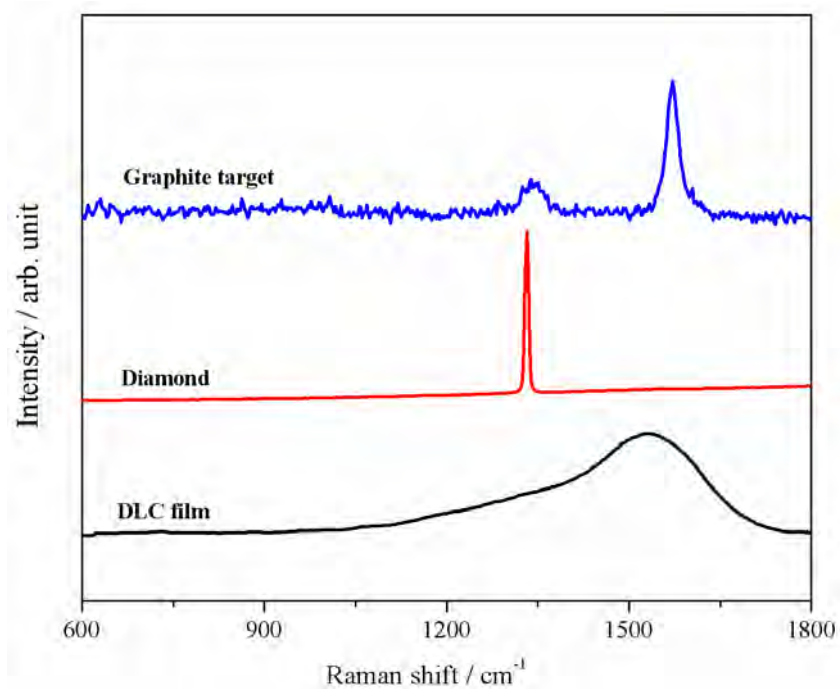


Figure 6.13 Raman spectra of a DLC film, a diamond film and the graphite target with excitation wavelength 514 nm.

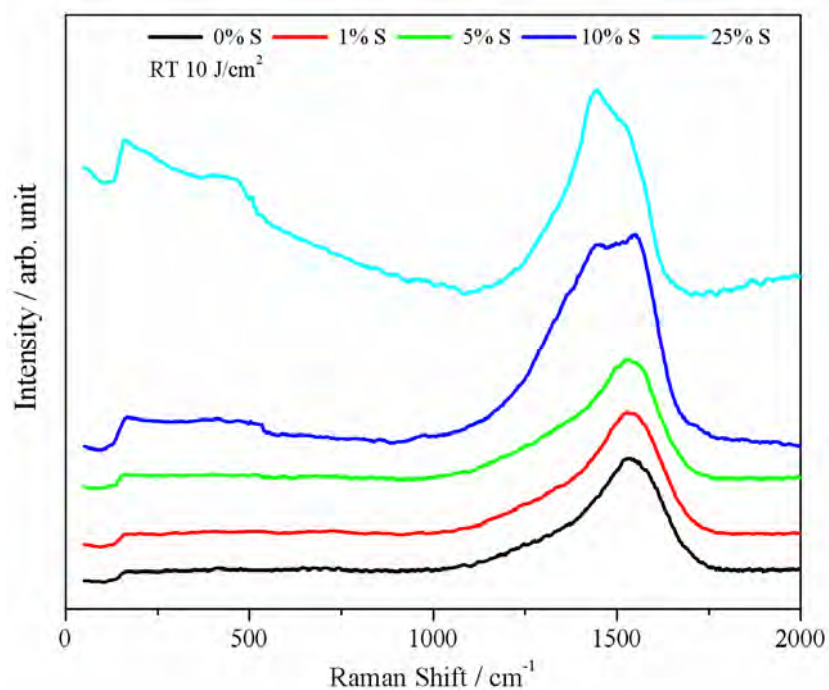
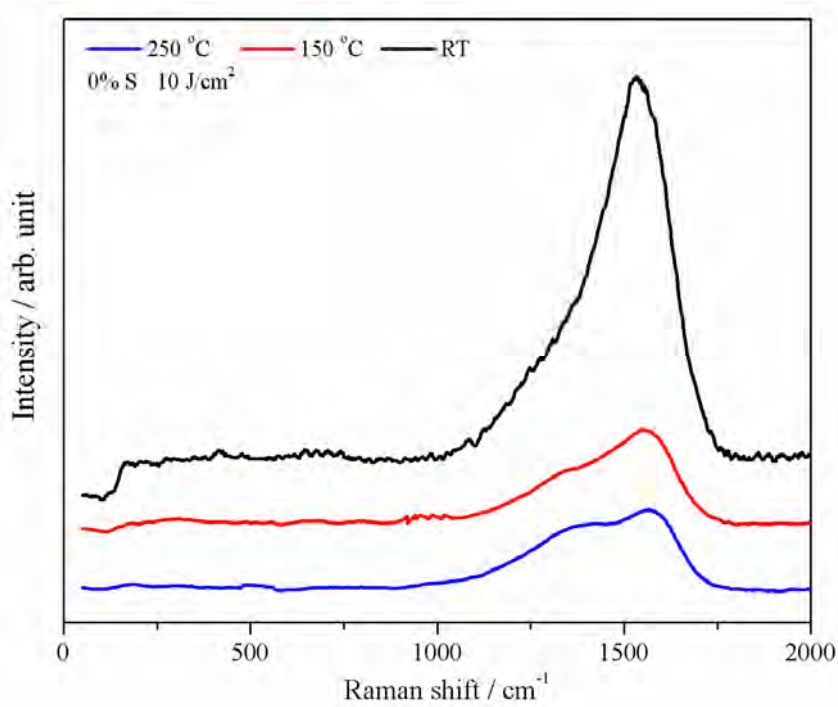


Figure 6.14 Raman spectra of DLC and S-DLC films at different sulphur molar percentages deposited at room temperature and 10 J/cm² of laser fluence.

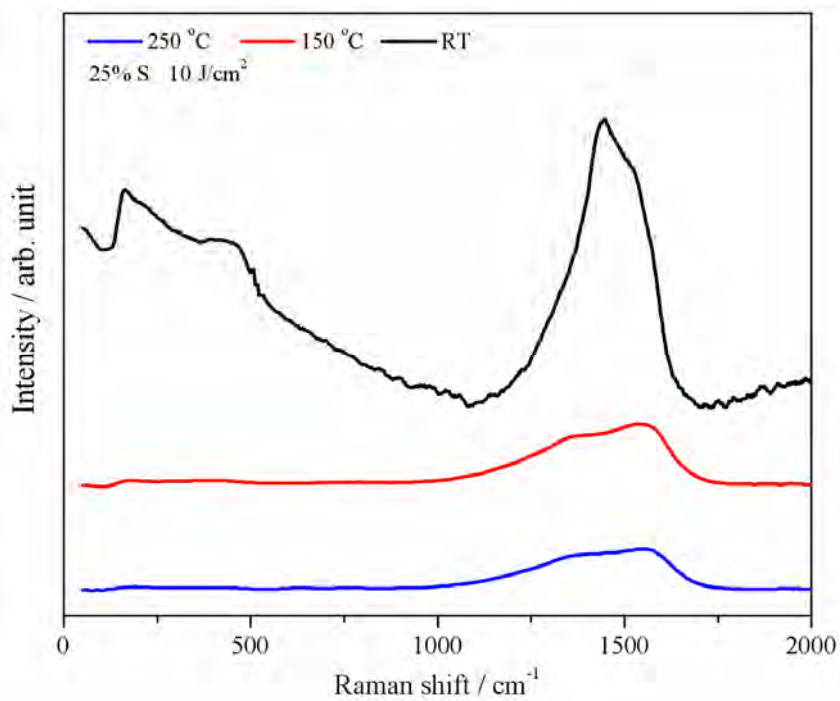
An example of Raman spectra for DLC and S-DLC films at different sulphur molar percentages at room temperature with 10 J/cm^2 of laser fluence is shown in Figure 6.14. This figure shows that the spectrum from a S-DLC film containing a lower sulphur molar percentage is found to be very similar to the spectrum from a pure DLC film. However, at higher sulphur molar percentages there is a clear difference. The most striking difference between the spectra was the development of the D peak shoulder as the S content increases. The quantity of sulphur creates increased asymmetry in the structure revealed by the increased D peak of S-DLC films. This suggests that the presence of sulphur in the films and its effect on the plasma chemistry may be to increase the A_{1g} symmetry in-plane breathing modes of aromatic six-membered ring clustering in the films. The G-peak position shifts frequency with increasing of amount of sulphur. This indicates that the presence of sulphur in the films make a modification to the E_{2g} symmetry in-plane stretching mode of crystalline graphite. Moreover, the intensity of the Raman spectra of S-DLC films with 25% sulphur doping at room temperature increased in the range $10\text{-}1000 \text{ cm}^{-1}$. This is due to increasing fluorescence.

An example of Raman spectra of S-DLC films at different substrate temperatures with 10 J/cm^2 of laser fluence at (a) 0% sulphur molar percentage, and (b) 25% sulphur molar percentage is shown in Figure 6.15. This figure shows that the substrate temperature shifts the G-peak position to high frequency. This means that DLC and S-DLC deposited at higher substrate temperatures should contain more crystalline graphite.

An example of Raman spectra of DLC films deposited at different laser fluences at room temperature with (a) 0% sulphur molar percentage and (b) 25% sulphur molar percentage, is shown in Figure 6.16. This figure shows that the laser fluence shifts the D-peak position and changes the A_{1g} symmetry in-plane breathing modes of aromatic six-membered ring clustering in the films.

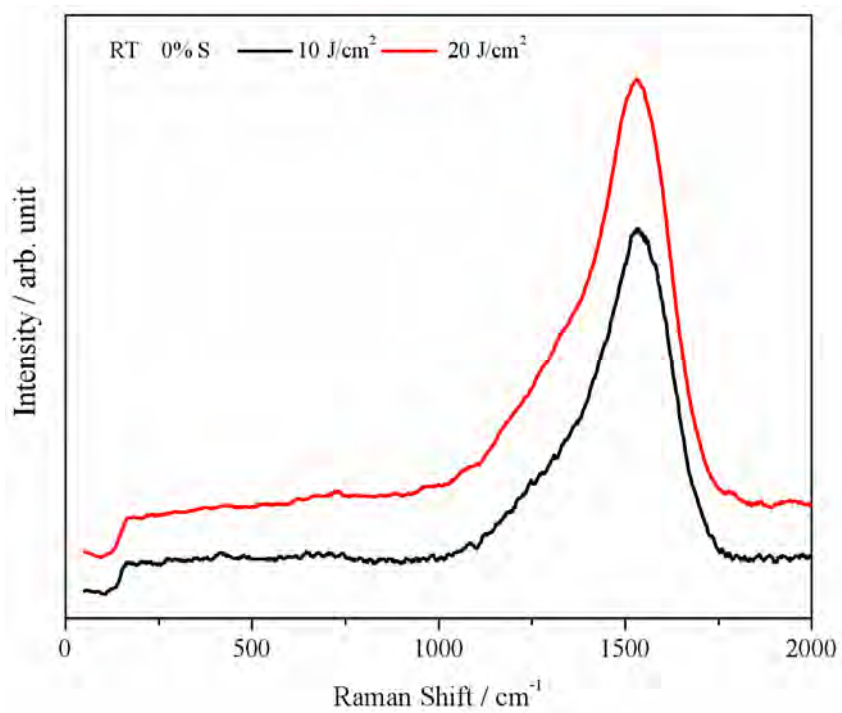


(a)

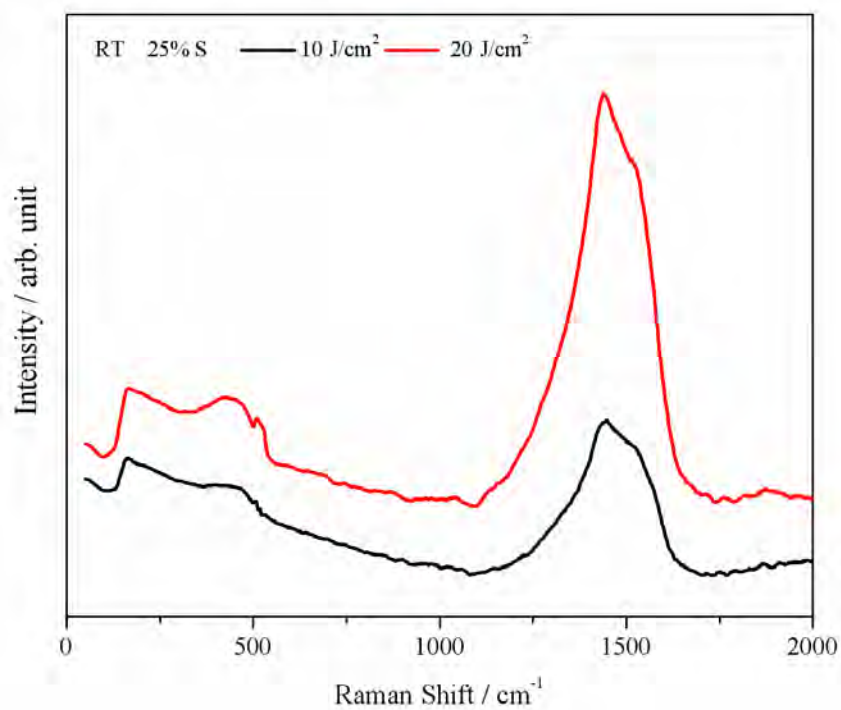


(b)

Figure 6.15 Raman spectra of S-DLC films at different substrate temperatures with 10 J/cm² laser fluence at (a) 0% sulphur molar percentage, and (b) 25% sulphur molar percentage.



(a)



(b)

Figure 6.16 Raman spectra of S-DLC films at different laser fluence at room temperature with (a) 0% sulphur molar percentage, and (b) 25% sulphur molar percentage.

However, all of these spectra can be clearly characterised by their G-peak positions and I_D/I_G ratios. In the characterisation, all Raman spectra of DLC films were fitted by following the procedure given in Section 5.1.3. After the curve fitting, it was found that there exist two broad peaks, a broad G-peak centered $\sim 1560\text{ cm}^{-1}$ and a shoulder of the disorder peak centered $\sim 1390\text{ cm}^{-1}$, which stems from the fact that finite crystalline sizes are absent. This is the common method of fitting DLC films.

S-DLC films were best fitted as three Gaussian line-shape peaks. They occur at $\sim 1560\text{ cm}^{-1}$ and 1440 cm^{-1} denoted as the G- and D-peaks, which relate to the E_{2g} symmetry in-plane stretching mode of crystalline graphite and the A_{1g} symmetry in-plane breathing modes of aromatic rings of graphite, respectively. A third peak was found at $\sim 1323\text{ cm}^{-1}$, which is related to sp^3 -bonded carbon, which occurs after sulphur doping. An example curve fit of a S-DLC film Raman spectrum is shown in Figure 6.17.

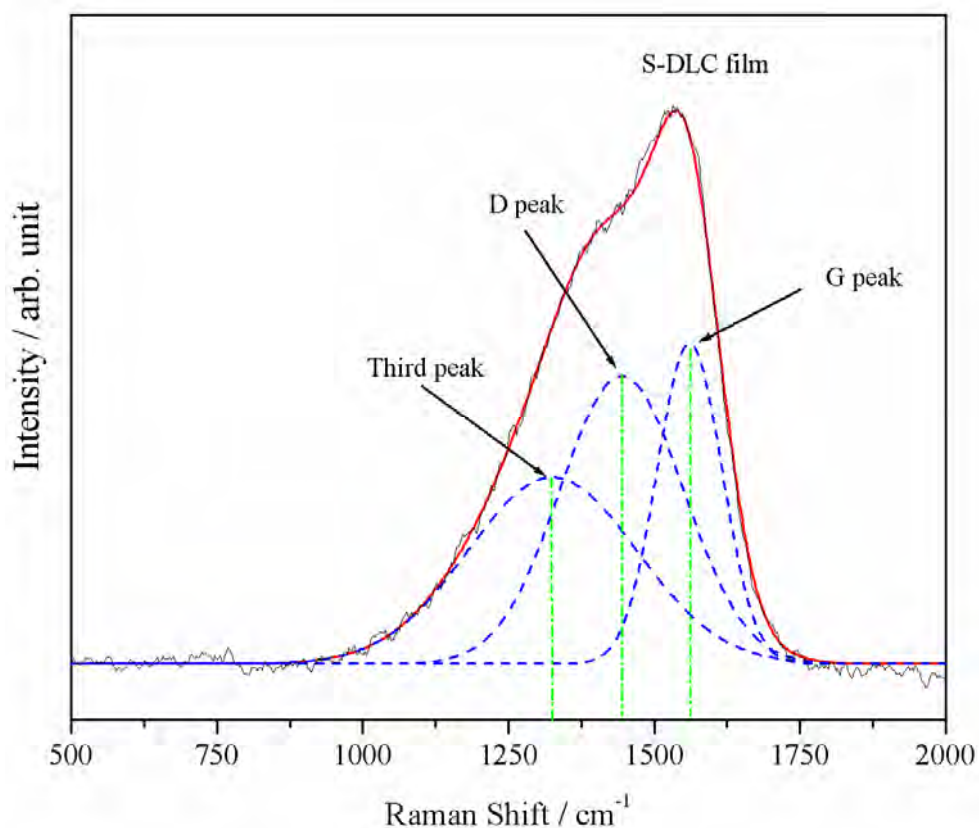


Figure 6.17 Example of Raman spectrum fitting of an S-DLC film.

The G peak position and I_D/I_G ratio can be used to indicate the sp^2 bonded planar carbon clusters. These clusters connect to both sp^2 and sp^3 hybridized carbon. The variation of the G-peak position and I_D/I_G ratio at different percentages of sulphur is shown in Figures 6.18 and 6.19, respectively, for three temperatures: room temperature, 150 °C and 250 °C, and two laser fluences: 10 J/cm² and 20 J/cm². The horizontal axis is the molar percentage of sulphur with graphite.

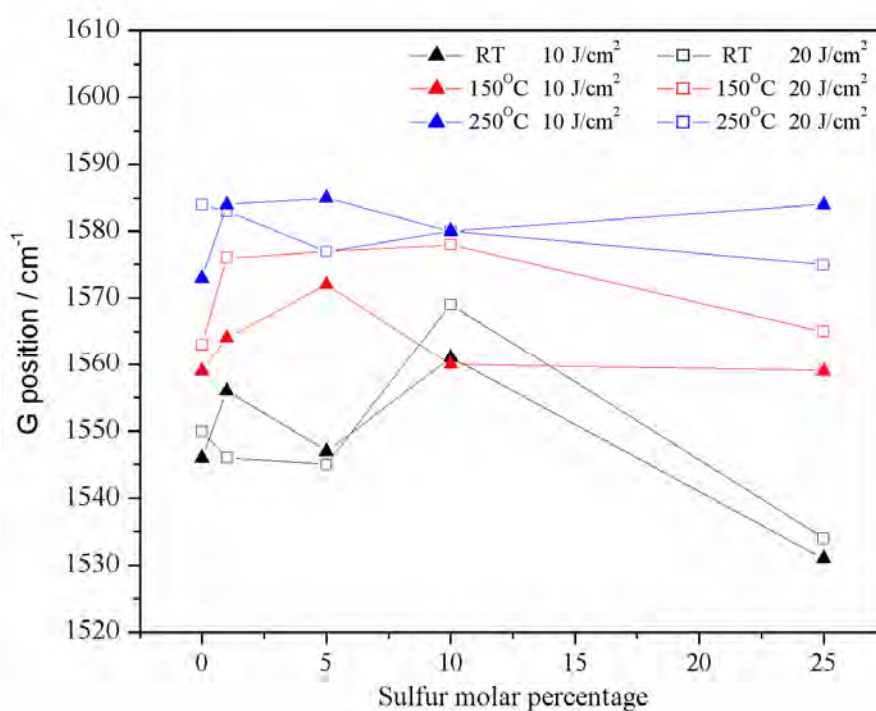


Figure 6.18 Plot of G-peak position versus sulphur molar percentages at different substrate temperatures at 10 J/cm² and 20 J/cm² laser fluence.

According to Figures 6.18 and 6.19, the G-peak position and the I_D/I_G ratios of DLC and S-DLC films were in the range of 1530-1590 cm⁻¹ and 0.20-1.40, respectively, consistent with the results from other workers. These figures showed that sulphur content, substrate temperature and laser fluence change the structure of the films significantly. The G-peak position did not show a clear trend with laser fluence and sulphur molar percentage, but it did with substrate temperature.

At the same laser fluence and sulphur molar percentages, increases in substrate temperature shift the G-peak position. The G-peak position shift indicates that at high substrate temperature a structure modification occurred in films in which the sp^2 clusters combine and grow rapidly (*i.e.* graphitization). At low substrate temperature no structural modification of the sp^2 carbon clusters occurred; hence the average cluster size decreases rapidly. Thus, deposited films at higher substrate temperature should contain a more crystalline phase of nano-sized graphite.

The sulphur molar percentage produced a larger G-peak position shift for films deposited at lower temperature than for films deposited at higher temperature. This is evidence for the development of graphitization in the films with increasing S content, because the G-peak position was not changed more at the higher substrate temperature. This means that at higher substrate temperature, the amount of sulphur that was added in DLC doping has little effect on graphitization of the film. The laser fluence also shifts the G-peak position; therefore, laser fluence also causes graphitization.

The Raman spectra showed that pure DLC films exhibit increased graphitic character containing larger numbers of graphite clusters, as evidence by the observed behavior that the G-peak shifts to higher frequency, together with an increasing I_D/I_G ratio. Moreover, Raman spectra of pure DLC films can be used to obtain information on defects and the size of the graphite clusters to predict the E_g . It is well known that in pure DLC films the E_g is proportional to the graphite cluster size, while the I_D/I_G ratio is inversely proportional to the graphite cluster size. Therefore, the relationship that I_D/I_G is inversely proportional to E_g , when a D-peak is present, means that a decrease in the band gap will always be indicated by an increase in I_D/I_G . Therefore, the Raman spectra show decreasing E_g with increasing substrate temperature at constant laser fluence and sulphur molar percentage. This prediction is consistent with E_g measured from the SE and UV-VIS results.

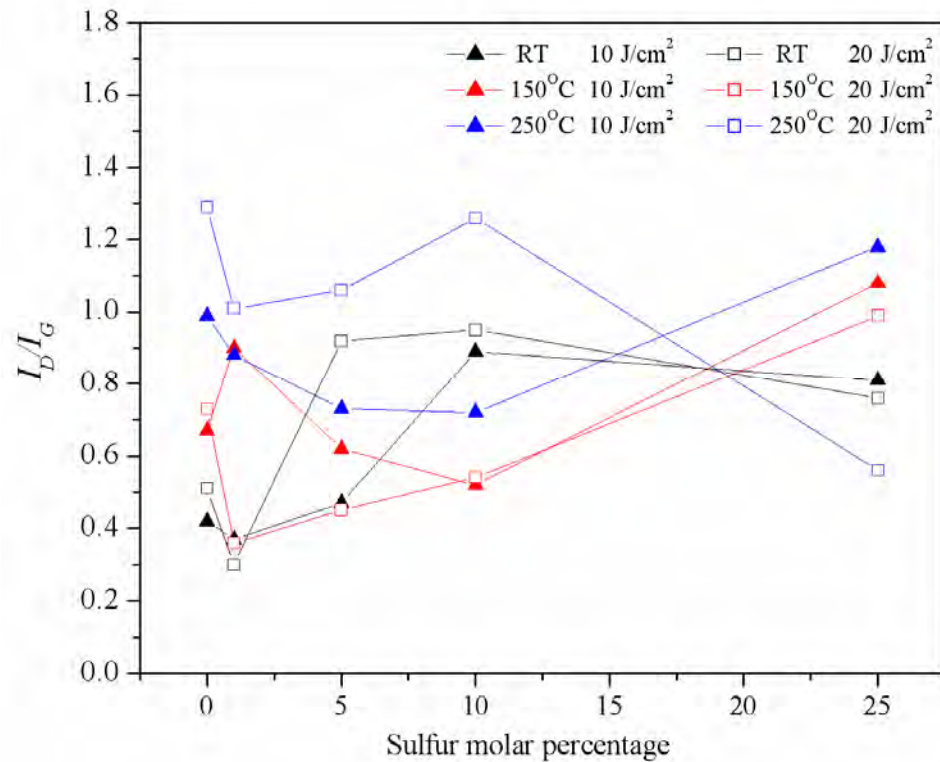


Figure 6.19 Plot of I_D/I_G ratio versus sulphur molar percentages at different substrate temperatures at 10 J/cm² and 20 J/cm² laser fluence.

However, the relationship that the G-peak position is proportional to the I_D/I_G ratio cannot hold with all S-DLC films due to the appearance of the third peak in S-DLC films related to sp^3 -bonded carbon. In S-DLC films, some of the cluster boundaries are decorated by sulphur-carbon bonds, which also connect the sp^2 matrix cluster together. But the G-peak position and I_D/I_G ratio did not seem to be directly related to the expected change in $sp^3 : sp^2$ ratio at increasing sulphur molar percentage. This is because the desorbed sulphur and sulphur-carbon from the edges of sp^2 clusters in S-DLC films, lead to changes in the sp^3 bonding configuration. The cluster boundaries were believed to include the presence of sp^3 hybridized carbon. Therefore, the G-peak position, the I_D/I_G ratio and the third peak must be considered together in order to answer the question of whether an S-DLC film has graphite-like or diamond-like properties.

6.4.2. Elemental Composition by EDX

EDX was used to analyze the composition of carbon and sulphur in S-DLC films. The EDX spectra are shown in Appendix B. The ratio of sulphur:carbon was obtained, and the result of elemental analysis is shown in Figure 6.20. This figure shows that the % atomic ratio S/C of S-DLC films increases with increasing sulphur molar percentage at constant substrate temperature and laser fluence. This evidence shows that the amount of sulphur in the film increased, and corresponds with the amount of sulphur in the target.

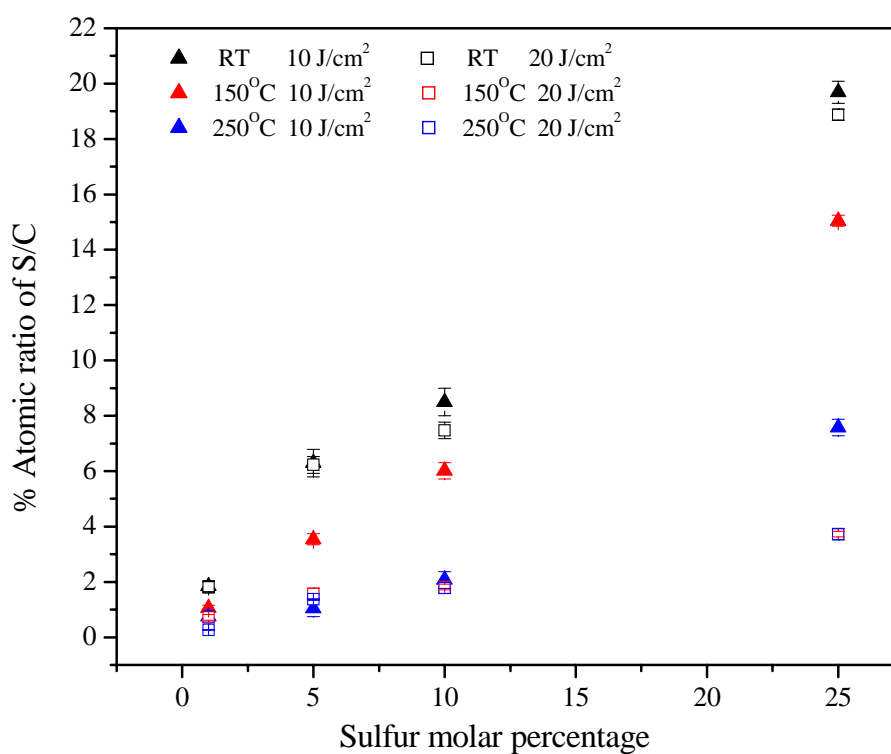


Figure 6.20 % Atomic ratio of S/C of S-DLC films versus sulphur molar percentage at different substrate temperatures and laser fluence.

At constant laser fluence and sulphur molar percentage, the % atomic ratio S/C of S-DLC films decreased with increasing substrate temperature. This means that the amount of sulphur decreased when films were deposited at higher substrate temperature. These results are consistent with the carrier concentration and Raman spectra results. The carrier concentration was found to decrease at higher substrate temperature due to the decreasing sulphur incorporation in the films. Raman spectra results showed a shift of the G-peak position at higher substrate temperature due to the preferential evaporation of sulphur.

At constant substrate temperature and sulphur molar percentage, the % atomic ratio S/C of S-DLC films decreased with increasing laser fluence. This means that the amount of sulphur decreased when films were deposited at higher laser fluence. These results are also consistent with the decreased carrier concentration results measured at higher laser fluence.

6.4.3. Elemental Composition by SIMS

An example of a depth profile from an S-DLC film deposited from a target with 1% atomic ratio of S/C at room temperature and 10 J/cm^2 laser fluence is shown in Figure 6.21. The C^- , O^- , Si^- and $^{34}\text{S}^-$ secondary ions were obtained in the depth profiles. The figure confirms that sulphur can incorporate into DLC films. The start of the depth profile (about 0-150 s) is the time used to equilibrate the etch rate of the ions. Therefore, during this time the signal cannot be used to describe the film composition accurately. After 150 - 350 s etching, the profile is almost flat, suggesting that the film has an almost a homogeneous composition of species within the film. After 600 s, a trace of oxygen is seen corresponding to reaching the native oxide layer on the Si substrate. However, these SIMS data are not quantitative; therefore, the intensity of sulphur and carbon peaks cannot be compared to get absolute concentrations.

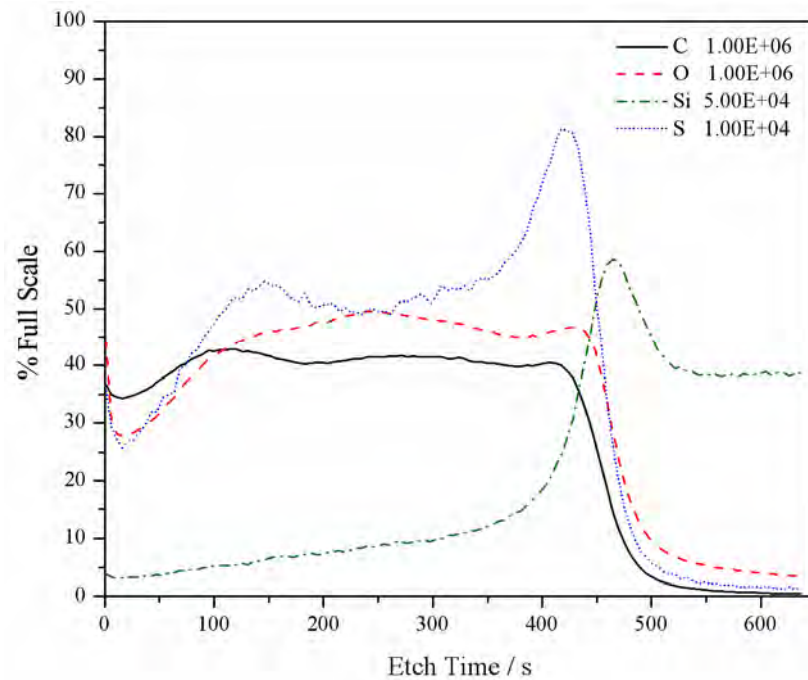


Figure 6.21 SIMS depth profile of an S-DLC film.

In this figure, the vertical axis shows % full-scale of C, O, Si and S equal to 10^6 , 10^6 , 5×10^4 and 10^4 , respectively. At the equilibrium state of the etch rate, 150-350 s, the amount of S and C were found to be approximately 5×10^3 and 4×10^5 , respectively. Therefore, the ratio of S/C in this film was found to be approximately 1% S/C. This can explain why S-DLC films that are formed by PLD techniques had the same composition as the target because the high initial rate of heating of the target, the high efficient atomic excitation and electronic ionization, and the non-thermal target erosion by the plasma, all combine to cause uniform ejection of the surface material. This stoichiometric transfer is an advantage of the PLD method.

CHAPTER VII

CONCLUSIONS AND SUGGESTIONS

7.1. Conclusions

Pulsed laser ablation of a sulphur-graphite target was carried out by ArF excimer laser deposition at a laser wavelength of 193 nm and fluence of 10 and 20 J/cm² to produce S-DLC films. The sulphur-graphite target was made from the graphite and sulphur power at different molar ratios 0%, 1%, 5%, 10% and 25%. S-DLC films were deposited on silicon and quartz substrates under 1×10⁻⁶ Torr pressure at different temperatures from room temperature to 250 °C. The effects of substrate temperature, laser fluence and % atomic ratio of S/C were studied for the S-DLC film electrical, optical, physical and structural properties.

DLC films deposited at room temperature at 10 J/cm² with 0% atomic ratio of S/C were found to have results diamond-like properties, such as high hardness at 29.2±0.6 GPa, an energy band gap of 1.90 eV, a resistivity of the order of 10⁵ Ω·cm, a *n* value of 2.6-2.7 and *k* values of 0-0.6. All of these DLC results were in a similar range to those measured from high quality DLC containing a high proportion of sp³ carbon that have been measured by other workers.

In contrast, S-DLC films showed resistivity values in the range 10³-10⁶ Ω·cm, corresponding to a *E_g* in the range of 0.25-2.00 eV. The carrier concentration was found to be in the range 10¹⁴-10¹⁸ cm⁻³, while the Hall mobility was in the range of 10⁻⁵-1 cm²·V⁻¹·s⁻¹. The thickness of the films was in the nanometre range, while the hardness of the films was in the range of 10-30 GPa. The surface morphology showed the presence of micron-sized particulates on the surface. Elemental composition analysis confirmed the presence of S in the films.

For S-DLC films deposited at higher substrate temperature the structure of the films changed into more sp^2 hybridization. It is believed that the depositing S ions species may be preferentially evaporate from the film during the deposition process, leading to a C-rich film and restructuring of the lattice. Also, the thermal expansion of the substrate helps anneal film, leading to a restructuring into a more stable crystalline form, *e.g.* graphite.

Therefore, at higher substrate temperature, the resistivity, the E_g and the hardness decreased with the increasing of sp^2 hybridization. The Hall mobility increased due to the presence of more crystalline graphite at higher substrate temperature. The carrier concentration and % atomic ratio of S/C decreased due to the preferential evaporation of S species that arrive at the substrate. The Raman spectra showed the G-peak shifts to higher frequency with the presence of more sp^2 hybridization. The particulate size decreased with increasing substrate temperature, accompanied by the film becoming smoother, again, possibly as a result of evaporation and/or annealing.

Generally, the laser fluence affected the kinetic energy of ion species. In this work laser fluences of 10 J/cm^2 and 20 J/cm^2 were used in deposition process. A laser fluence of 20 J/cm^2 created ions with higher kinetic energy than a laser fluence of 10 J/cm^2 . At the higher laser fluence, the increased ion kinetic energy will implant the ion species into the substrate. This will cause bond-breaking and reforming, leading to a change in the structure of films into sp^2 hybridization. Some ion species will simply scatter off from the film surface. Therefore, at higher laser fluence, the resistivity, the E_g and the hardness decreased as a result of the increased sp^2 hybridization. The Hall mobility increased due to the increased crystalline graphite content at higher laser fluence. The carrier concentration and % atomic S/C ratio decreased with increasing of laser fluence, due to the implantation, restructuring and evaporation effects mentioned above. And at higher laser fluence, the Raman spectra showed the G-peak shifting to higher frequency with pure DLC films, but there was no clear trend with S-DLC films. This is because of the complicated relationship between the effect of % atomic ratio of S/C and the substrate temperature. The

particulate size decreased and the films became smoother but thinner with increasing fluence, again due increased evaporation of the impinging species.

At lower % atomic ratio of S/C the films showed a decreasing resistivity and E_g . At higher S content the films showed increasing of resistivity and E_g . The Hall mobility and hardness decreased with increasing of percentages content. The carrier concentration and % atomic S/C ratio increased with increasing S content. This is because as the amount of sulphur in the target increases it increases the sulphur incorporation into films. The amount of particulates increased with S content, and the films became rougher and thicker, due to highly non-uniformity of the target composition. The Raman spectra showed that the presence of sulphur caused the appearance of a third peak related to the sp^3 hybridization.

7.2. Suggestions

To our knowledge, DLC films can be doped with several elements to become both p-type and n-type semiconductors. This dissertation demonstrates that sulphur is another element that can be used to change the DLC film properties to be an n-type semiconductor. The S content can be controlled to tailor the film properties for a specific application. Therefore, possible future experiments involve study the incorporation of other elements (As, Sb, Li, etc) into DLC films, to determine if they too can act as dopants and affect the electrical properties.

REFERENCES

- [1] F. Qian, R. K. Singh, S. K. Dutta and P. P. Pronko. Laser deposition of diamondlike carbon films at high intensities. *Appl. Phys. Lett.* 67 (1995): 3120-3122.
- [2] V. I. Merkulov, D. H. Lowndes, G. E. Jellison, Jr., A. A. Puretzky and D. B. Geohegan. Structure and optical properties of amorphous diamond films prepared by ArF laser ablation as a function of carbon ion kinetic energy. *Appl. Phys. Lett.* 73 (1998): 2591-2593.
- [3] C. MÖßner, P. Grant, H. Tran, G. Clarke, D. J. Lockwood, H. J. Labbé, B. Mason and I. Sproule. Characterization of diamond-like carbon by Raman spectroscopy, XPS and optical constants. *Thin Solid Films* 317 (1998): 397-401.
- [4] F. Xiong, Y. Y. Wang, V. Leppert and R. P. H. Chang. Pulsed laser deposition of amorphous diamond-like carbon films with ArF (193 nm) excimer laser. *J. Mat. Res.* 8 (1993): 2265-2272.
- [5] A. Hu, I. Alkhesho, H. Zhou and W. W. Duley. Optical and microstructural properties of diamond-like carbon films grown by pulsed laser deposition. *Diam. Relat. Mater.* 16 (2007): 149-154.
- [6] N. Ravi, V. L. Bukhovets, I. G. Varshavskaya and G. Sundararajan. Deposition of diamond-like carbon films on aluminium substrates by RF-PECVD technique: Influence of process parameters. *Diam. Relat. Mater.* 16 (2007): 90-97.
- [7] M. Pandey, D. Bhattacharyya, D. S. Patil, K. Ramachandran and N. Venkatramani. Diamond-like carbon coatings: AFM and ellipsometric studies. *Surf. Coat. Technol.* 182 (2004): 24-34.
- [8] A. Kumar, U. Ekanayake and J. S. Kapat. Characterization of pulsed laser-deposited diamond-like carbon films. *Surf. Coat. Technol.* 102 (1998): 113-118.
- [9] S. Kumar, K. S. A. Butcher and T. L. Tansley. X-ray photoelectron spectroscopy characterization of radio frequency reactively sputtered carbon nitride thin films. *J. Vac. Sci. Technol. A* 14 (1996): 2687-2692.

- [10] D. M. Teter and R. J. Hemley. Low-compressibility carbon. *Science* 271 (1996): 53-55.
- [11] A. Zocco, A. Perrone, E. D'Anna, G. Leggieri, A. Luches, A. Klini, I. Zergioti and C. Fotakis. Deposition of carbon nitride films by reactive pulsed-laser ablation at high fluences. *Diam. Relat. Mater.* 8 (1999): 582–585.
- [12] P. Hammer, N. M. Victoria and F. Alvarez. Effects of increasing nitrogen concentration on the structure of carbon nitride films deposited by ion beam assisted deposition. *J. Vac. Sci. Technol. A* 18 (2000): 2277–2287.
- [13] C. M. Niu, Y. Z. Lu and C. M. Lieber. Experimental realization of the covalent solid carbon nitride. *Science* 261 (1993): 334–337.
- [14] S. Lopez, H. M. Dunlop, M. Benmalek, G. Tourillon, M. S. Wong, W. D. Sproul. XPS, XANES and ToF-SIMS characterization of reactively magnetron-sputtered carbon nitride films. *Surf Interface Anal.* 25 (1998): 315–323.
- [15] S. Muhl and J. M. Méndez. A review of the preparation of carbon nitride films. *Diam. Relat. Mater.* 8 (1999): 1809–1830.
- [16] D. I. Jones and A. D. Stewart. Properties of hydrogenated amorphous carbon films and the effects of doping. *Philos. Mag. B* 46 (1982): 423-434.
- [17] V. S. Veerasamy, G. A. J. Amaratunga, C. A. Davis, A. E. Timbs, W. I. Milne and D. R. McKenzie. N-type doping of highly tetrahedral diamond-like amorphous carbon. *J. Phys. Condens. Matter* 5 (1993): L169-L174.
- [18] A. Helmbold, P. Hammer, J. U. Thiele, K. Rohwer and D. Meissner. Electrical conductivity of amorphous hydrogenated carbon. *Philos. Mag. B* 72 (1995): 335-350.
- [19] J. Tsukamoto and A. Takahashi. Polymeric Product of Carbon Disulfide and Its Electrical Properties. *Jap. J. Appl. Phys.* 25 (1986): L338-L340.
- [20] C. L. Spiro, W. F. Banholzer and D. S. McAtee. Chemical vapor deposition of novel electronic materials from carbon disulfide. *Thin Solid Films* 220 (1992): 122-124.
- [21] R. K. Sathir and K. F. Schoch, Jr.. Plasma-Polymerized Carbon Disulfide Thin-Film Rechargeable Batteries. *Chem. Mater.* 8 (1996): 1281-1286.

- [22] S. Al-Dallal, S. M. Al-Alawi, S. Aljishi, M. Hamman and S. Arekat. Hydrogenated amorphous carbon-sulfur alloy thin films grown from a CH₄ and H₂S gas mixture by rf glow discharge. *J. Non-Cryst. Solids* 196 (1996): 168-172.
- [23] S. Al-Dallal, M. Hammam, S. M. Al-Alawi, S. Aljishi and A. Breitschwardt. Infrared and raman spectroscopy of a-Si, Se: H alloys prepared by r.f. glow discharge. *Philos. Mag. B* 63 (1992): 211-218.
- [24] J. Filik, I. M. Lane, P. W. May, S. R. J. Pearce and K. R. Hallam. Incorporation of sulfur into hydrogenated amorphous carbon films. *Diam. Relat. Mater.* 13 (2004): 1377-1384.
- [25] I. Sakaguchi, M. N. Gamo, Y. Kikucji, E. Yasu and H. Haneda. A donor dopant for Sulfur: n-type diamond semiconductors. *Phys. Rev. B* 60 (1999): 2139-2141.
- [26] W. Gou, G. Li, X. Chu and B. Zhong. Effect of negative self-bias voltage on microstructure and properties of DLC films deposited by RF glow discharge. *Surf. Coat. Technol.* 201 (2007): 5043-5045.
- [27] S. Adhikary, X. M. Tian, S. Adhikari, A. M. M. Omer, H. Uchida and M. Umeno. Bonding defects and optical band gaps of DLC films deposited by microwave surface-wave plasma CVD. *Diam. Relat. Mater.* 14 (2005): 1832-1834.
- [28] X. M. He, J. F. Bardeau, D. H. Lee, K. C. Walter, M. Tuszewski and M. Nastasi. Bonding defects and optical band gaps of DLC films deposited by microwave surface-wave plasma CVD. *J. Vac. Sci. Technol. B* 17 (1999): 822-827.
- [29] J. Noshiro, S. Watanabe, T. Sakurai and S. Miyake. Friction properties of co-sputtered sulfide/DLC solid lubricating films. *Surf. Coat. Technol.* 200 (2006): 5849-5854.
- [30] A. A. Puretzky, D. B. Geohegan, G. E. Jellison, Jr. and M. M. McGibbon. Comparative diagnostic of ArF- and KrF-laser generated carbon plumes used for amorphous diamond-like carbon films deposition. *Appl. Surf. Sci.* 96,98 (1995): 859-865.

- [31] H. Nakazawa, Y. Yamagata, M. Suemitsu and M. Mashita. Thermal effects on structure properties of diamond-like carbon films prepared by pulsed laser deposition. *Thin Solid Films* 467 (2004): 98-103.
- [32] S. M. Mominuzzaman, T. Soga, T. Jimbo and M. Umeno. Diamond-like carbon by pulsed laser deposition from a camphoric carbon target: effect of phosphorus incorporation. *Diam. Relat. Mater.* 10 (2001): 1839-1842.
- [33] S. S. Yap and T. Y. Tou. Diamond-like carbon formation for various positions by pulsed laser deposition. *Appl. Surf. Sci.* 248 (2005): 340-343.
- [34] J. C. Orlianges, C. Champeaux, A. Catherinot, Th. Merle and B. Angleraud. Pulsed laser deposition of tetrahedral amorphous carbon films from glassy carbon and graphite targets: a comparative study. *Thin Solid Films* 453,454 (2004): 285-290.
- [35] P. Mosaner, M. Bonelli and A. Miotello. Pulsed laser deposition of diamond-like carbon films: reducing internal stress by thermal annealing. *Appl. Surf. Sci.* 208,209 (2003): 561-565.
- [36] F. Qian, V. Craciun, R. K. Singh, S. D. Dutta and P. P. Pronko. High intensity femtosecond laser deposition of diamond-like carbon thin films. *J. Appl. Phys.* 86 (1999): 2281-2290.
- [37] N. Jegenyés, Z. Toth, B. Hopp, J. Klebniczki, Z. Bor and C. Fotakis. Femtosecond pulsed laser deposition of diamond-like carbon films: The effect of double laser pulses. *Appl. Surf. Sci.* 252 (2006): 4667-4671.
- [38] D. L. Pappas, K. L. Saenger, J. Bruley and W. Krakow. Pulsed laser deposition of diamond-like carbon films. *J. Appl. Phys.* 71 (1992): 5675-5684.
- [39] H. C. Ong and R. P. H. Chang. Effect of laser intensity on the properties of carbon plasmas and deposited films. *Phys. Rev. B* 55 (1997): 13213-13220.
- [40] J. Filik. *Fundamental studies on the deposition and characterisation of novel diamond-like materials*. Doctoral dissertation, School of Chemistry Faculty of Science University of Bristol, 2006.
- [41] J. Robertson. Properties of diamond-like carbon. *Surf. Coat. Technol.* 50 (1992): 185-203.

- [42] Y. Lifshitz, G. D. Lempert and E. Grossman. Substantiation of subplantation model for diamondlike Film Growth by atomic force microscopy. *Phys. Rev. Lett.* 72 (1994): 2753-2757.
- [43] M. Hakovirta, X. M. He and M. Nastasi. Optical properties of fluorinated diamond-like carbon films produced by pulsed glow discharge plasma immersion ion processing. *J. Appl. Phys.* 88 (2000): 1456-1459.
- [44] J. C. Angus, J. E. Stultz, P. J. Shiller, J. R. Macdonald, M. J. Mirtich and S. Domitz. Composition and properties of the so-called diamond-like carbon. amorphous carbon films. *Thin Solid Films* 118 (1984): 311-320.
- [45] M. Silinskas and A. Grigonis. Low energy post-growth irradiation of amorphous hydrogenated carbon (a-C:H) films. *Diam. Relat. Mater.* 11 (2002): 1026-1030.
- [46] A. N. Kayani. *Deposition and Characterization of Diamond-Like Carbon Films With and Without Hydrogen and Nitrogen*. Doctoral dissertation, Department of Physics and Astronomy the College of Arts and Science Ohio University, 2003.
- [47] E. Staryga and G. W. Bak. Relation between physical structure and electrical properties of diamond-like carbon thin films. *Diam. Relat. Mater.* 14 (2005): 23-34.
- [48] H. Li, T. Xu, C. Wang, J. Chen, H. Zhou and H. Liu. Annealing effect on the structure, mechanical and tribological properties of hydrogenated diamond-like carbon films. *Thin Solid Films* 515 (2006): 2153-2160.
- [49] A. H. Lettington. Applications of diamond-like carbon thin films. *Carbon* 36 (1998): 555-560.
- [50] A. Grill. Electrical and optical properties of diamond-like carbon. *Thin Solid Films* 355,356 (1999): 189-193.
- [51] E. Fitzer, K. H. Köchling, H. P. Boehm and H. Marsh. Recommended terminology for the description of carbon as a solid. *Pure & Appl. Chem.* 67 (1995): 473-506.
- [52] J. Robertson. Defect in diamond-like carbon. *Phys. Stat. Sol. (a)* 186 (2001): 177-185.

- [53] A. C. Ferrari and J. Robertson. Interpretation of Raman spectra of disordered and amorphous carbon. *Phys. Rev. B* 61 (2000): 14095-14107.
- [54] A. K. Nix, D. Schwen, C. Ronning, J. Krauser, C. Trautmann and H. Hofsäss. Electronic properties of graphite-like ion tracks in insulating tetrahedral amorphous carbon. *Rev. Adv. Mater. Sci.* 15 (2007): 192-197.
- [55] H. Schulza, M. Leonhardt, H. J. Scheibe and B. Schultrich. Ultra hydrophobic wetting behaviour of amorphous carbon films. *Surf. Coat. Technol.* 200 (2005): 1123-1126.
- [56] M. Vinnichenko, R. Gago, N. Huang, Y. X. Leng, H. Sun, U. Kreissig, M. P. Kulish and M. F. Maitz. Spectroscopic ellipsometry investigation of amorphous carbon films with different sp^3 content: relation with protein adsorption. *Thin Solid Films* 455,456 (2004): 530-534.
- [57] S. Chowdhury, M. T. Laugier and I. Z. Rahman. Effects of substrate temperature on bonding structure and mechanical properties of amorphous carbon films. *Thin Solid Films* 447,448 (2004): 174-180.
- [58] H. Kinoshita, J. Takahashi and T. Hando. Formation of electrical conductive hard-carbon (DLC) films using $i-C_4H_{10}/N_2$ supermagnetron plasma. *Superficies y Vacío* 9 (1999): 108-110.
- [59] H. Weidong, D. Ding and Z. Rujuan. Synthesis and characteristics of diamond-like carbon films. *Plasma Sci. Technol* 6 (2004): 2255-2258.
- [60] J. Robertson. Diamond-like amorphous carbon. *Mater. Sci. Eng. R* 37 (2002): 129-281.
- [61] J. Robertson. The deposition mechanism of diamond-like a-C and a-C: H. *Diam. Relat. Mater.* 3 (1994): 361-368.
- [62] T. Yoshitake, T. Nishiyama, H. Aoki, K. Suizu, K. Takahashi and K. Nagayama. Atomic force microscope study of carbon thin films prepared by PLD. *Appl. Surf. Sci.* 141 (1999): 129-137.
- [63] T. Datta. Optical-absorption edge and disorder effects in hydrogenated amorphous diamond like carbon films. *Phys. Rev. B* 40 (1989): 5956-5960.
- [64] J. A. Garrido, C. E. Nebel, M. Stutzmann, E. Gheeraert, N. Casanova, E. Bustarret and A. Deneuve. A new acceptor state in CVD-diamond. *Diam. Relat. Mater.* 11 (2002): 347-350.

- [65] R. Haubner. Comparison of sulfur, boron, nitrogen and phosphorus additions during low-pressure diamond deposition. *Diam. Relat. Mater.* 14 (2005): 355-363.
- [66] R. B. Li, X. J. Hu, H. S. Shen and X. C. He. Co-doping of diamond with boron and sulfur. *J. Mater. Sci.* 39 (2004): 1135-1137.
- [67] A. S. Barnard, S. P. Russo and I. K. Snook. *Ab initio* modelling of band states in doped diamond. *Philos. Mag.* 83 (2003): 1163-1174.
- [68] J. A. Garrido, C. E. Nebel and M. Stutzmann. Electrical and optical measurement of CVD diamond doped with sulfur. *Phys. Rev. B* 65 (2002): 1654091-1654096.
- [69] T. Yokoya, T. Nakamura, T. Matsushita, T. Muro, E. Ikenaga, M. Kobata, K. Kobayashi, Y. Takano, M. Nagao, T. Takenouchi, H. Kawarada and T. Oguchi. Valence band electronic structures of heavily boron-doped superconducting diamond studied by synchrotron photoemission spectroscopy. *New Diam. Front. C. Tec.* 17 (2007): 11-19.
- [70] J. R. Petherbridge, P. W. May, G. M. Fuge, G. F. Robertson, K. N. Rosser and M. N. R. Ashfold. Sulfur doping of diamond films: spectroscopic, electronic, and gas-phase studies. *J. Appl. Phys.* 91 (2002): 3605-3613.
- [71] N. F. Mott. Electrons in disordered structures. *Adv. Phys.* 16 (1967): 49.
- [72] T. Makino, H. Kato, M. Ogura, H. Watanabe, S. G. Ri, Y. G. Chen, S. Yamasaki and H. Okushi. Electrical and optical characterization of (001)-oriented homoepitaxial diamond p-n junction. *Diam. Relat. Mater.* 15 (2006): 513-516.
- [73] T. Makino, H. Kato, M. Ogura, H. Watanabe, S.-G. Ri, S. Yamasaki and H. Okushi. Strong excitonic emission from (001)-oriented diamond P-N junction. *Jpn. J. Appl. Phys.* 44 (2005): L1190-L1192.
- [74] A. J. Lu, B. C. Pan and J. G. Han. Electronic and vibrational properties of diamond like hydrocarbons. *Phys. Rev. B.* 72 (2005): 0354471-0354479.
- [75] B. Kleinsorge, A. Ilie, M. Chhowalla, W. Fukarek, W. I. Milne, and J. Robertson. Electrical and optical properties of boronated tetrahedrally bonded amorphous carbon (ta-C:B). *Diam. Relat. Mater.* 7 (1998): 472-476.

- [76] M. Allon-Alaluf and N. Croitoru. Nitrogen and iodine doping in amorphous diamond-like carbon films. *Diam. Relat. Mater.* 6 (1997): 555-561.
- [77] A. M. M. Omer, S. Adhikari, S. Adhikary, M. Rusop, H. Uchida, T. Soga and M. Umeno. Electrical conductivity improvement by iodine doping for diamond-like carbon thin-films deposited by microwave surface wave plasma CVD. *Diam. Relat. Mater.* 15 (2006): 645-648.
- [78] S. M. Mominuzzaman, H. Ebisu, T. Soga, T. Jimbo and M. Umeno. Phosphorus doping and defect studies of diamond-like carbon films by pulsed laser deposition using camphoric carbon target. *Diam. Relat. Mater.* 10 (2001): 984-988.
- [79] D. Zhou, F. A. Stevie, L. Chow, J. McKinley, H. Gnaser and V. H. Desai. Nitrogen incorporation and trace element analysis of nanocrystalline diamond thin films by secondary ion mass spectrometry. *J. Vac. Sci. Technol. A* 17 (1999): 1135-1140.
- [80] J. F. Prins. Nitrogen-related n-type conduction with low thermal activation in diamond. *Semicond. Sci. Technol.* 16 (2001): L50-L52.
- [81] E. Gheeraert, N. Casanova, A. Tajani, A. Deneuve, E. Bustarret, J. A. Garrido, C. E. Nebel and M. Stutzmann. N-type doping of diamond by sulfur and phosphorus. *Diam. Relat. Mater.* 11 (2002): 289-295.
- [82] R. Kalish, C. Uzan-Saguy, R. Walker and S. Prawer. Electrically active sulfur-defect complexes in sulfur implanted diamond. *J. Appl. Phys.* 94 (2003): 3923-3930.
- [83] A. Y. Liu and R.M. Wentzcovitch. Stability of carbon nitride solids. *Phys. Rev. B* 50 (1994): 10362-10365.
- [84] G. W. Yang and J. B. Wang. Carbon nitride nanocrystals having cubic structure using pulsed laser induced liquid-solid interfacial reaction. *Appl. Phys. A Mater.* 71 (2000): 343-344.
- [85] W. L. Yin, Y. Bando, M. S. Li, Y. X. Liu and Y. X. Qi. Unique single-crystalline beta carbon nitride nanorods. *Adv. Mater.* 15 (2003): 1840-1844.

- [86] L. Yang, P. W. May, L. Yin, J. A. Smith and K. N. Rosser. Ultra fine carbon nitride nanocrystals synthesized by laser ablation in liquid solution. *J. Nano. Part. Res.* 9 (2007): 1181-1185.
- [87] M. M. Golzan, D. R. McKenzie, D. J. Miller, S. J. Collocott and G. A. J. Amaratunga. Magnetic and spin properties of tetrahedral amorphous carbon. *Diam. Relat. Mater.* 4 (1995): 912-916.
- [88] C. A. Davis, Y. Yin and D. R. McKenzie. The structure of boron-, phosphorus- and nitrogen-doped tetrahedral amorphous carbon deposited by cathodic arc. *J. Non-Cryst. Solids* 170 (1994): 46-50.
- [89] T. Y. Leung, W. F. Man, P. K. Lim, W. C. Chan, F. Gaspari and S. Zukotynski. Determination of the sp^3/sp^2 ratio of a-C:H by XPS and XAES. *J. Non-Cryst. Solids* 254 (1999): 156-160.
- [90] M. T. Kuo, P. W. May, A. Gunn, M. N. R. Ashford and R. K. Wild. Studies of phosphorus doped diamond-like carbon films. *Diam. Relat. Mater.* 9 (2000): 1222-1227.
- [91] S. R. J. Pearce, P. W. May, R. K. Wild, K. R. Hallam and P. B. J. Heard. Deposition and properties of amorphous carbon phosphide films. *Diam. Relat. Mater.* 11 (2002): 1041-1046.
- [92] O. Loew. Carbon disulfide produced a dark precipitate on exposure to sunlight. *Z. Chem.* 4 (1868): 622-626.
- [93] J. Dewar and H. O. Jones. Note on carbon monosulfide. *Proc. R. Soc. Lond. A* 83 (1910): 408-413.
- [94] P. W. Bridgman. Explorations toward the Limit of Utilizable Pressures. *J. Appl. Phys.* 12 (1941): 461-469.
- [95] M. N. R. Ashfold, F. Claeysens, G. M. Fuge and S. J. Henley. Pulsed laser ablation and deposition of thin films. *Chem. Soc. Rev.* (2004): 23-31.
- [96] S. H. Bae, S. Y. Lee, B. J. Jin and S. Im. Growth and characterization of ZnO thin films grown by pulsed laser deposition. *Appl. Surf. Sci.* 169-170 (2001): 525-528.
- [97] S. Christoulakis, M. Suche, M. Katharakis, N. Katsarakis, E. Koudoumas and G. Kiriakidis. ZnO nanostructures transparent thin films by PLD. *Rev. Adv. Mater. Sci.* 10 (2005): 331-334.

- [98] Y. Sun, N. G. N.- Angwafor, D. J. Riley and M. N. R. Ashfold. Synthesis and photoluminescence of ultra-thin ZnO nanowire/nanotube arrays formed by hydrothermal growth. *Chem. Phys. Lett.* 431 (2006): 352-357.
- [99] D. K. T. Ng, M. H. Hong, L. S. Tan, Y. W. Zhu and C. H. Sow. PLD synthesis of GaN nanowires and nanodots on patterned catalyst surface for field emission study. *Appl. Phys. A* 93 (2008): 685-689.
- [100] P. Sanguino, O. M. N. D. Teodoro, M. Niehus, C. P. Marques, A. M. C. Moutinho, E. Alves and R. Schwarz. Structural and composition analysis of GaN films deposited by cyclic-PLD at different substrate temperatures. *Sensor. Actuat. A-Phys.* 21 (2005): 131–135.
- [101] M. Cazzanelli, D. Cole, J. F. Donegan, J. G. Lunney, P. G. Middleton, K. P. O'Donnell, C. Vinegoni and L. Pavesi. Photoluminescence of localized excitations in pulsed-laser-deposited GaN. *Appl. Phys. Lett.* 73 (1998): 3390-3392.
- [102] N. Matsuyama, K. Yukimura and T. Maruyama. Amorphous diamond-like carbon film prepared by pulsed laser deposition with application of pulsed negative bias voltage. *J. Appl. Phys.* 89 (2001): 1938-1941.
- [103] D. B. Chrisey and G. K. Hubler. *Pulsed laser deposition of thin films*. eds. D. B. Chrisey and G. K. Hubber. New York: John Wiley and Sons, 1994.
- [104] H. V. Bergmann and U. Stamm. *Excimer Laser Technolog.* eds. D. Basting and G. Marowsky. Springer, New York: Springer Berlin Heidelberg, 2005.
- [105] P. R. Willmott and J. R. Huber. Pulsed laser vaporization and deposition. *Rev. Mod. Phys.* 72 (2000): 315-328.
- [106] D. H. Lowndes, D. B. Geohegan, A. A. Puretzky, D. P. Norton and C. M. Roleau. Synthesis of novel thin-film material by pulse laser deposition. *Science* 273 (1996): 898-903.
- [107] M. Kanai, T. Kawai and S. Kawai. Low-temperature formation of multilayered Bi(Pb)-Sr-Ca-Cu-O thin films by successive deposition using laser ablation. *Appl. Phys. Lett.* 54 (1989): 1800-1802.
- [108] T. Jackson and S. B. Palmer. Oxide superconductor and magnetic metal thin film deposition by pulsed laser ablation: a review. *Physica D* 27 (1994): 1581-1594.

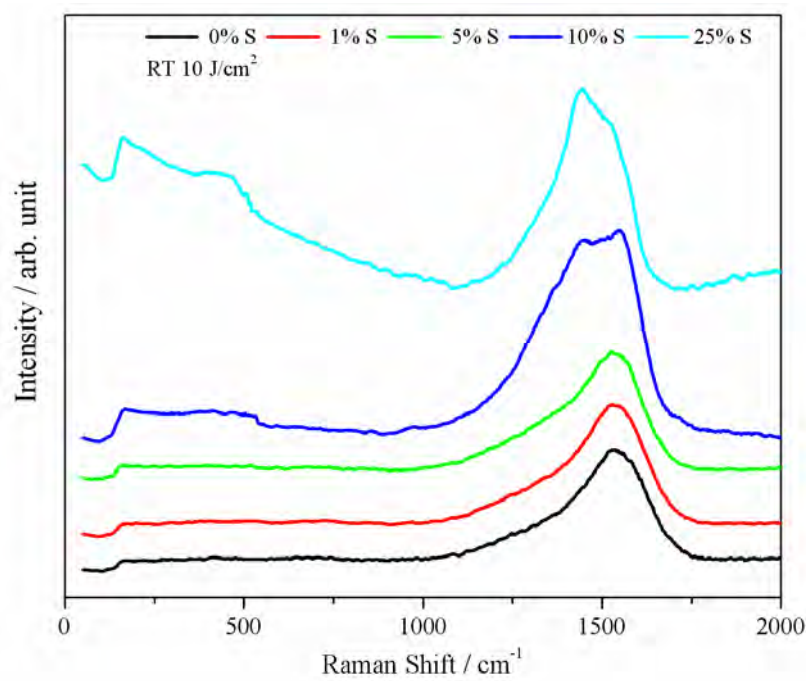
- [109] P. T. Murray and D. T. Peeler. Pulsed laser deposition of carbon films: dependence of film properties on laser wavelength. *J. Electron. Mater.* 23 (1994): 855-859.
- [110] G. A. Smith, L. C. Chen and M. C. Chuang. Effects of processing parameters on KrF excimer laser ablation deposited ZrO₂ films. *Mater. Res. Soc. Symp. Proc.* 235 (1992): 840-843.
- [111] T. Yoshida, S. Takeyama, Y. Yamada and K. Mutoh. Nanometer-sized silicon crystallites prepared by excimer laser ablation in constant pressure inert gas. *Appl. Phys. Lett.* 68 (1996): 1770-1772.
- [112] Y. Y. Yamada, N. Suzuki, T. Makino and T. Yoshida. Stoichiometric indium oxide thin films prepared by pulsed laser deposition in pure inert background gas. *J. Vac. Sci. Technol. A* 18 (2000): 81-83.
- [113] A. Mele, A. G. Guidoni, R. Kelly, A. Miotello, S. Orlando, R. Teghill and C. Flamini. Angular distribution and expansion of laser ablation plumes measured by fast intensified charge coupled device photographs. *Nucl. Instrum. Meth. B* 166 (1996): 257-261.
- [114] T. Venkatesan, X. D. Wu, R. Muenchausen and A. Pique. Pulsed laser deposition: future directions. *MRS Bull.* XVII(2) (1992): 839-855.
- [115] F. Davanloo, E. M. Juengerman, D. R. Jander, T. J. Lee and C. B. Collins. Amorphous diamond film produced by a laser plasma source. *J. Appl. Phys.* 67 (1990): 2081-2087.
- [116] J. Krishnaswamy, A. Rengan, J. Narayan, K. Vedam, a. C. J. McHargue. Thin-Film Deposition by a New Laser Ablation and Plasma Hybrid Technique. *Appl. Phys. Lett.* 54 (1989): 2455-2457.
- [117] T. Sato, S. Furuno, S. Iguchi and M. Hanabusa. Diamond-Like Carbon-Films Prepared By Pulsed-Laser Evaporation. *Appl. Phys. A* 45 (1988): 355-360.
- [118] S. Orzeszko, N. D. Bholá, J. A. Woollam, J. J. Pouch, S. A. Alterovitz and D. C. Ingram. Thin-film hermeticity: A quantitative analysis of diamond-like carbon using variable angle spectroscopic ellipsometry. *J. Appl. Phys.* 64 (1988): 4175-4180.

- [119] L. Yang. *Self-Assembly and Ordering Nanomaterials by Liquid-Phase Pulsed Laser Ablation*. Doctoral dissertation, School of Chemistry Faculty of Science University of Bristol, 2007.
- [120] Sean R. J. Pearce. *The Synthesis and Characterisation of Carbon Phosphide*. Doctoral dissertation, School of Chemistry Faculty of Science University of Bristol, 2003.
- [121] Resistivity of Carbon: Graphite (online). Available from: <http://hypertextbook.com/facts/2004/AfricaBelgrave.shtml> [2009, January 6]
- [122] Resistivity of Carbon: Diamond (online). Available from: <http://hypertextbook.com/facts/2004/KerryRemulla.shtml> [2009, January 6]
- [123] J. J. Li, C. Z. Gu, H. Y. Peng, H. H. Wu, W. T. Zheng and Z. S. Jin. Field emission properties of diamond-like carbon films annealed at different temperatures. *Appl. Surf. Sci.* 251 (2005): 236-241.
- [124] R. J. Narayn. Laser processing of diamond-like carbon-metal composites. *Appl. Surf. Sci.* 245 (2005): 420-430.

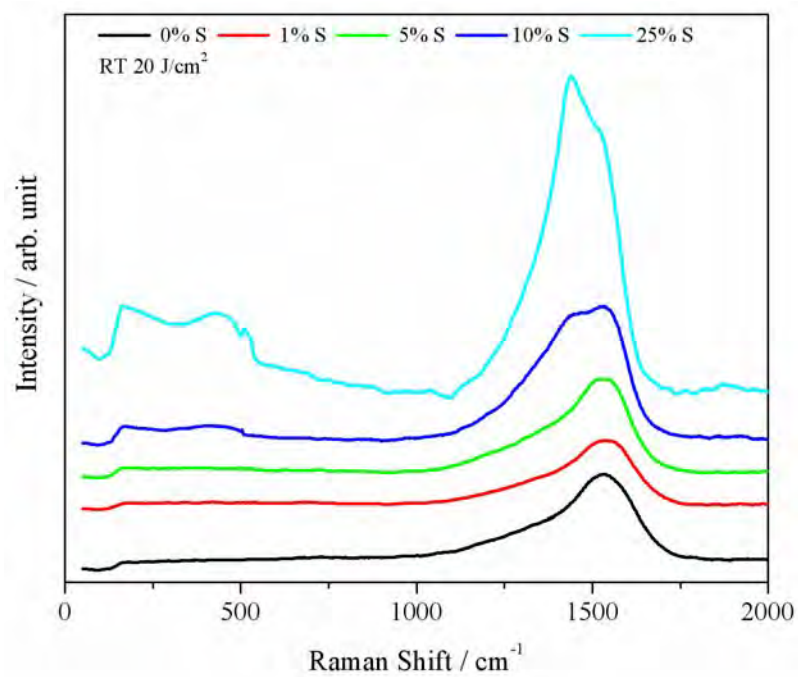
APPENDICES

APPENDIX A

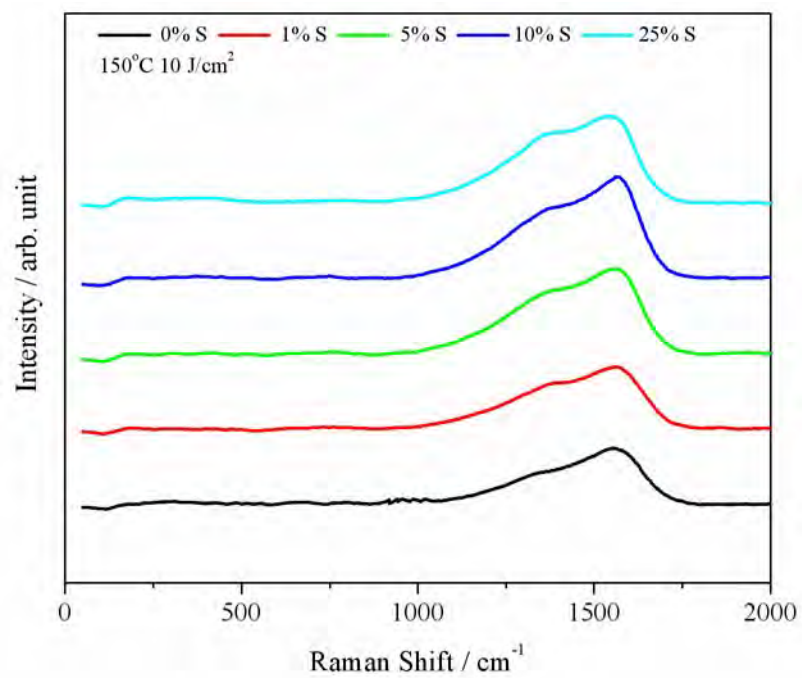
Raman Spectra of S-DLC films



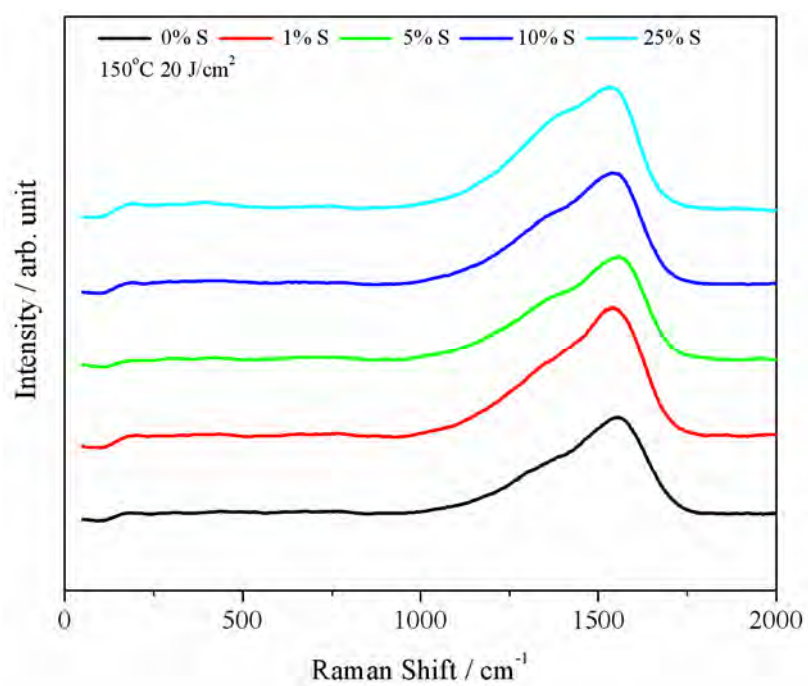
(a)



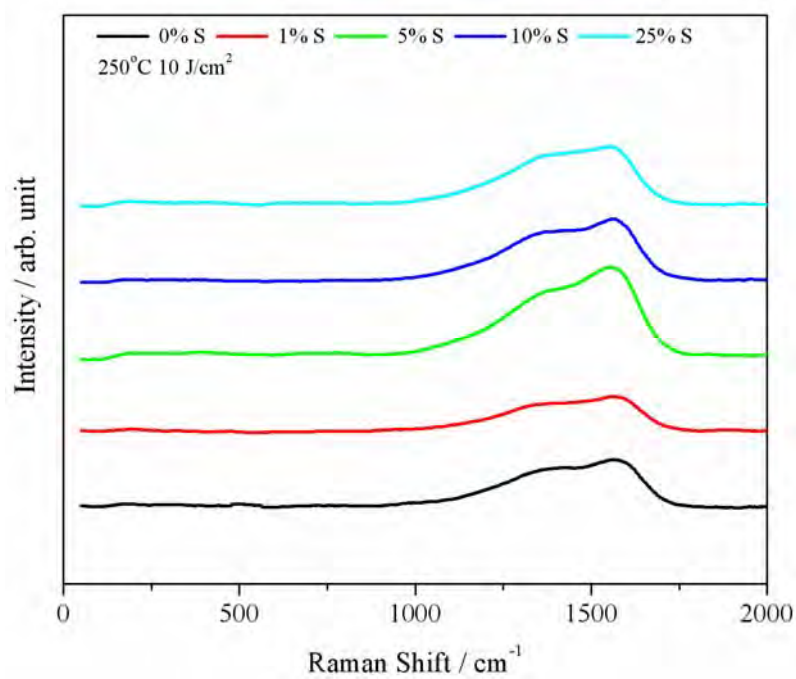
(b)



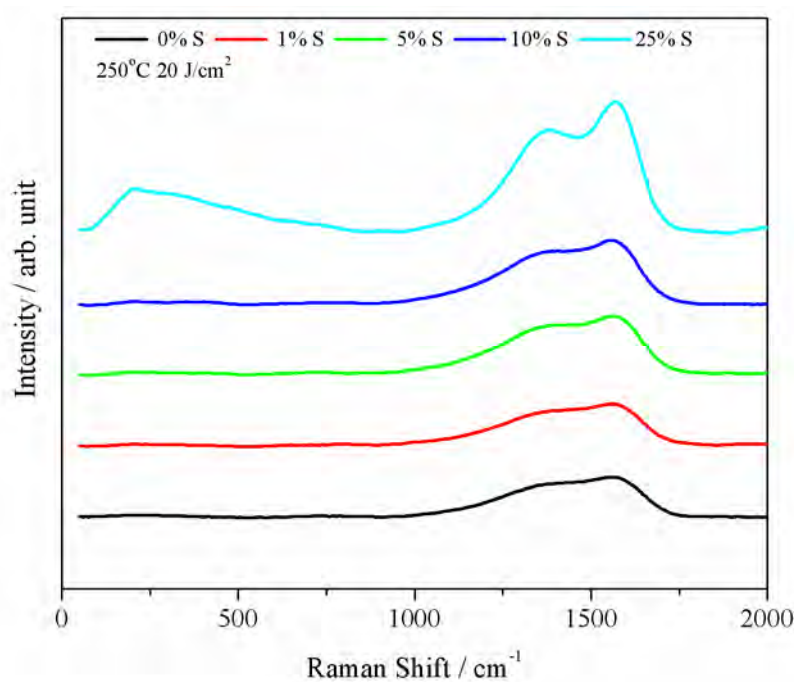
(c)



(d)



(e)



(f)

Figure A Raman spectra for DLC and S-DLC films at different percentages of sulphur deposited at (a) room temperature and 10 J/cm² laser power (b) room temperature and 20 J/cm² laser power (c) 150°C and 10 J/cm² laser power (d) 150°C and 20 J/cm² laser power (e) 250°C and 10 J/cm² laser power (f) 250°C and 20 J/cm² laser power.

APPENDIX B

**Elemental Composition of S-DLC films determined by
Energy-Dispersive X-Ray Spectroscopy (EDX)**

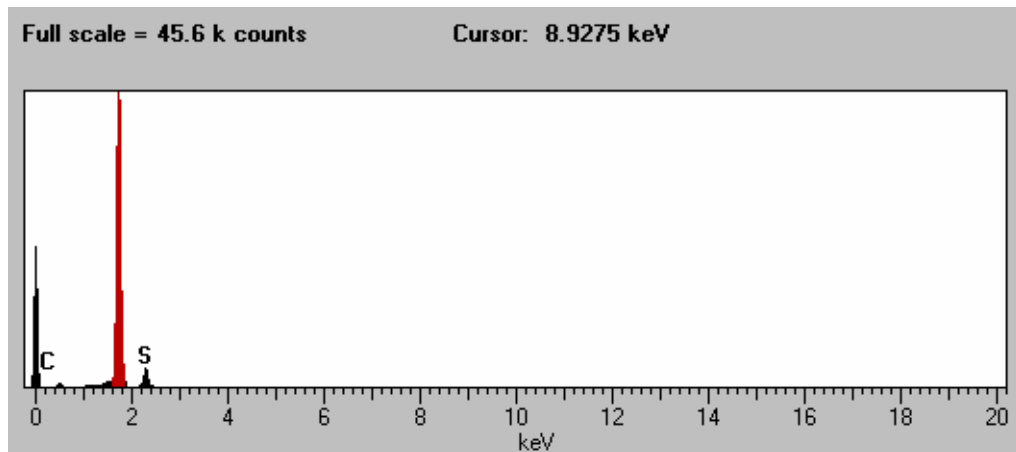


Figure B Example of an EDX spectrum from a S-DLC film.

BIOGRAPHY

NAME Miss KANCHAYA HONGLERTKONGSAKUL

BIRTH 12 OCTOBER 1979

EDUCATION 2004 Master's Degree, Department of Physics, Faculty of Science,
Chulalongkorn University

CONFERENCE:

1. The 2nd Mathematics and Physical Science Graduate Congress, December 11-15, 2006, "Plasma Diagnostic Measurements in a Microwave Plasma Reactor (MPR) by the Single Langmuir Probe", NUS University, Singapore.
2. The 34th Congress on Science and Technology Thailand, October 31-November 2, 2008, "Effect of Substrate Temperature on Excimer Laser Deposited DLC Films Properties", Queen Sirikit National Convention Center, Bangkok, Thailand.
3. SPC 2009: Physics for Dynamic Society, March 19-21, 2009, "Structural and optical properties of diamond-like carbon films deposited by pulsed laser ablation", Cha-am, Phetchburi, Thailand.
4. *ChinaNANO2009*, International Conference on Nanoscience & Technology, September 1-3, 2009, "Effect of Temperature on Sulfur-Doped Diamond-Like Carbon Films Deposited by Pulsed Laser Ablation", Beijing, China.
5. Diamond 2009: 20th Anniversary conference, September 6-10, "Electrical and Optical Properties of Diamond-like Carbon Films Deposited by Pulsed Laser Ablation", Athens, Greece.
6. SPC 2010: Physics for Dynamic Society, March 24-27, 2010, "Effect of Sulfur on Diamond-Like Carbon Films Deposited by Pulsed Laser Ablation", Kanchanaburi, Thailand.